CYCLOGENESIS DIAGNOSED WITH POTENTIAL VORTICITY

by

CHRISTOPHER A. DAVIS

B. S. Physics
University of Massachusetts (Amherst)
(1985)

Submitted to the Department of Earth, Atmospheric
and Planetary Sciences in partial fulfillment
of the requirements for the degree of

DOCTOR OF PHILOSOPHY IN METEOROLOGY

at the

MASSACHUSETTS INSTITUTE OF TECHNOLOGY
May, 1990

© Massachusetts Institute of Technology 1990
All rights reserved

Signature of Author.....
Dept. of Earth, Atmospheric and Planetary Sciences
May, 1990

Certified by.....
Kerry A. Emanuel
Professor of Meteorology
Thesis Supervisor

Accepted by.....
Thomas H. Jordan - Chairman
Departmental Committee on Graduate Students

MASSACHUSETTS INSTITUTE OF TECHNOLOGY
WITHDRAWN
MAR 2 1990
MIT LIBRARIES

CYCLOGENESIS DIAGNOSED WITH POTENTIAL VORTICITY

by

Christopher A. Davis

Submitted to the Department of Earth, Atmospheric and Planetary Sciences on May 21, 1990 in partial fulfillment of the requirements for the Degree of Doctor of Philosophy in Meteorology

Abstract

With the assumption of dynamically balanced flow, the structure and development of cyclones may be understood in terms of the distribution and evolution of the interior potential vorticity (PV) and boundary potential temperature (θ_B) fields. The goals of this observation based diagnostic study are: (1) to document the PV and θ distribution during four cases of cyclogenesis and quantify the contributions of the observed perturbations of PV and θ_B to the circulation of each cyclone (2) to examine the origin of PV and θ_B features comprising the majority of the cyclone perturbation and (3) to diagnose the influence of condensation on development, primarily through its effects on the PV distribution.

In each case examined, the initial development is dominated by the growth of a positive θ_B perturbation. The largest contributor to this growth is the flow associated with upper tropospheric PV anomalies. Lower tropospheric potential vorticity perturbations develop during cyclogenesis just upshear from the region of heaviest stratiform precipitation. Calculations of potential vorticity generation using both the balance equations and station precipitation data indicate that latent heat released in these regions is sufficient to account for the observed changes in low level PV.

Differences among the cases seemed to be smallest at the surface and largest at upper levels. Two cases exhibited large amplitude upper tropospheric features prior to surface

cyclogenesis. Subsequent cyclone developments featured a transient vertical structure. In the two cases with initially small amplitude upper level waves, the disturbances aloft and at low levels amplified simultaneously. The primary growth phase showed a nearly fixed vertical structure. Positive low level PV anomalies were generated in phase with the θ_B field and contributed roughly 1/3 to the total cyclonic circulation.

We identify the upper tropospheric PV anomalies as perturbations of θ on the tropopause (constant PV surface). The dominance of tropopause and lower boundary θ disturbances suggests a qualitative analogy with Eady dynamics, modified by the existence of a flexible upper material surface and the presence of condensation.

Thesis supervisor: Dr. Kerry A. Emanuel

Title: Professor of Meteorology

Acknowledgments

Although there were many people who provided valuable guidance during the course of this work, a few deserve special recognition. I wish to thank Professor Kerry Emanuel, supervisor of this thesis, for his insights, encouragement and emphasis on independent thought. Conversations with Professor Randy Dole were also especially useful as were comments by Professors Frederick Sanders and Richard Lindzen.

I also have appreciated the valuable interaction between myself and other meteorology graduate students (members of the team that reigns as two time defending National Forecasting Contest champions!). Special thanks go to my office companions Rob Black and Brad Lyon as well as to "microvax gods" Peter Neilley and John Nielsen. In addition, I must thank my friend Amelia Careghini for her support thoughout the arduous process that leads erratically toward a Ph. D.

However, the most important people in this whole endeavor have been my parents, Richard and Hazel Davis. They encouraged me to pursue my true interests and would have been supportive of any path I chose. It is to them that this work is dedicated.

This thesis work was supported by Grant ATM 8513871.

Contents

		Page
Acknowledgments		7
Chapter A	Motivation, Objectives and Summary	9
Chapter 1	Background	16
	Vorticity and Divergence	16
	Potential Vorticity Diagnostics	23
	Potential Vorticity in Simple Models	28
Chapter 2	Diagnostics	36
	Data and Computations of PV	36
	Inversion of PV	39
	Method of Solution	43
	Perturbations	49
	Tendency Calculations	53
	Examples	60
Chapter 3	Case I; December, 1987	64
	Quantitative Contributions	68
	Origin of Perturbations	74
	Diabatic Effects	78
	Summary	80
	Figures	83
Chapter 4	Additional Cases	100
	Case II; November, 1988	100
	Figures	111
	Case III; February, 1988	122
	Figures	132
	Case IV; December, 1987(b)	144
	Figures	155

Chapter 5	Summary and Discussion	165
	Summary of Cases	165
	Discussion	170
	Further Calculations	176
	Figures	181
Appendix A		186
References		188

Chapter A: Motivation, Objectives and Summary

Extratropical cyclones and anticyclones have been a prominent subject of research in meteorology for more than a century. The list of contributions from observational works alone is immense. Some of the more well known references are Bjerknes and Solberg (1922), Petterssen et al. (1955), Petterssen et al. (1962), Palmen and Newton (1969), Petterssen and Smebye (1971), Sanders and Gyakum (1980), Bosart and Lin (1984), Uccellini et al. (1985), Boyle and Bosart (1986), Sanders (1986). In spite of all these, we believe a succinct view of the fundamental underlying dynamics of midlatitude developments from observations is generally lacking. The simplest way to understand the dynamics of a system is to diagnose its behavior in terms of conserved quantities which concisely embody the state of that system. However, the classical interpretation of observed cyclogenesis did not arise directly from the consideration of such quantities. In fact, the popular development scenarios described by Petterssen (1955) and Petterssen and Smebye (1971) were partly empirical results useful for forecasting rather than for describing the essential physics behind cyclone intensification.

Beginning with Charney and Stern (1962), theoretical extensions of the classical studies by Charney (1947) and Eady (1949) began to focus on potential vorticity (PV) as the dynamic variable of fundamental importance in the study of midlatitude

cyclogenesis. Potential vorticity had been introduced some years before (Rossby 1940, Ertel 1942) as a scalar variable conserved following adiabatic, frictionless motion. The full usefulness of PV was realized with the knowledge that one could calculate the motion itself given the interior potential vorticity, potential temperature on the boundaries and a prescribed "balance" relation between the wind and temperature fields (Eliassen and Kleinschmidt 1957; Hoskins, McIntyre and Robertson 1985, hereafter HMR). Through its properties of *conservation* and *invertibility*, potential vorticity has come to be recognized as a very important diagnostic tool for atmospheric motions on the synoptic and larger scales (HMR). Observational studies of cyclogenesis have not fully exploited the properties of PV to quantitatively diagnose developments in the real atmosphere. Because of this, there has been insufficient common ground on which to compare observed cases of cyclogenesis with the solutions of idealized theoretical and numerical models.

The properties of PV allow one to isolate the disturbances in the flow that are crucial to development from those that are incidental. This is necessary if one is to reduce the inherent complexity of typical atmospheric states to a level where the underlying dynamics becomes apparent. In this thesis, we will use the invertibility and conservation properties of PV to quantify the roles of the potential vorticity features most influential in the development process. Importance here is measured by the strength of the circulation associated with a particular feature and the

ability of that flow to amplify perturbations elsewhere. These calculations will form the basis for interpreting the observations in terms of simpler models of cyclogenesis.

Specific questions we will address include (a) whether the significant interior PV features are concentrated at the tropopause, the steering level or distributed throughout the troposphere and what the importance of surface potential temperature perturbations is, (b) whether the development occurs with a vertical structure nearly constant in time or depends on a transient structure and, (c) what the influence of nonconservative processes (primarily latent heat release) is on cyclogenesis.

The first issue is related to the question of whether Eady "type" or Charney "type" dynamics are applicable. We use the word type here because we are referring to classes of behavior rather than specific models. In observed cyclone developments, we are unlikely to see either of these solutions in their pure form, hence we must look for potential vorticity distributions that signify different dynamical behavior. In a Charney type development, the significant PV perturbations are concentrated at the steering level and critical layer dynamics are important. The Eady scenario features no interior potential vorticity perturbations; the significant features are potential temperature waves at the upper boundary (or the tropopause) and at the ground. Synopticians have long pointed to the importance of waves in the upper troposphere in development (Bjerknes 1954, Petterssen 1955, Sanders 1986, 1987, 1988, Uccellini et al. 1985), perhaps indicating the

importance of tropopause perturbations. However, there are no calculations which cleanly isolate the importance of such waves in observed cases of cyclogenesis.

The second problem is related to the relative importance of modal versus non-modal growth in the atmosphere. Farrell (1984, 1989) has suggested that the transient development of perturbations with an initially favorable vertical tilt against the shear may be of greater importance than growth due to modal instability. This type of development exhibits algebraic rather than exponential growth, but may intensify rapidly for a short time, perhaps enough to render an exponential growth phase irrelevant. Although many descriptions of atmospheric development suggest transient structures are prevalent (e.g. the above works concerning upper level waves), this issue if far from settled. Even a modal development will enter a nonlinear phase when the structure changes markedly after the low level circulation has spun up (Simmons and Hoskins, 1978). Hence, one must note the phase behavior during the most rapid stage of development. In most atmospheric observational studies, vorticity at mid levels and at the surface are used to diagnose structural changes. Since stretching of vortex tubes provides a source of vorticity above a developing cyclone, the structure may appear more transient than when viewed from a potential vorticity perspective.

A third major issue investigated in this thesis is the importance on development of diabatic processes. Observational

studies have generally focussed on the effect of the latent heat released during the condensation of water vapor (Manabe 1956, Danard 1964, Tracton 1973, Bosart 1981, Dimego and Bosart 1982, Gyakum 1983, Emanuel 1988). Condensation is ubiquitous in nearly all mid latitude developments but its overall influence on cyclogenesis is still not well understood. Gradients of diabatic heating from condensation can act as a major source of PV in the lower troposphere. Thus, if we are able to identify that part of the PV distribution created by latent heat release, we can use the property of invertibility to calculate its contribution to the flow.

To investigate these issues, we examine four observed cases of cyclogenesis. Our procedure, which Chapter 2 outlines in detail, consists of breaking up the total potential vorticity distribution into pieces which have individual dynamical significance. We then calculate the flow associated with each of these perturbations and determine how each one contributes to the cyclone circulation directly or how it acts to amplify other features.

Our main results may be summarized as follows. For each case, we find that the low level circulation in the early stages of development is almost exclusively associated with potential temperature perturbations at the lower boundary. The low level winds from potential vorticity features in the upper troposphere contribute most to the amplification of the lower thermal wave. We also find that potential vorticity features in the lower troposphere likely result from the condensation of water vapor in stably stratified ascent regions. By this we mean that stratiform

precipitation, rather than convection, is the dominant type in the region of PV generation near the low level anomaly. These potential vorticity features are nearly colocated with the warm temperature phase of the low level thermal wave and, in two cases, contribute about 1/3 of the total low level circulation. Two of the developments feature initally large amplitude potential vorticity perturbations aloft and growth is transient. The other two cases begin with smaller upper tropospheric waves which grow during the low level intensification. These cases exhibit a relatively fixed phase structure during most of the cyclogenesis. Because of the prominence of the interaction between perturbations at the tropopause and at the lower boundary in each of the four cases, "Eady dynamics", modified by condensation in a way envisaged by Emanuel et al. (1987) and Montgomery and Farrell (1990) is deemed a roughly consistent paradigm for these developments.

Chapter 1 contains more background material, especially concerning potential vorticity and discusses some of the basic PV structures obtained from theoretical and numerical models of cyclogenesis. The application of some of our diagnostics to these quasigeostrophic solutions is also presented. The diagnostics appropriate for Ertel's potential vorticity are developed and discussed in chapter 2. In chapters 3 and 4, we present the four cases examined, each diagnosed using Ertel's potential vorticity. Chapter 3 reviews case I, which is fairly representative of the classic Petterssen development scenario. The three cases in

Chapter 4 serve mainly to contrast with this first case, and try to isolate those features that are common to each of the four developments. The first two cases feature somewhat smaller amplitude features in the initial state than case I. The last case in Chapter 4 serves two purposes. First, it presents a "null case" in which initial conditions were similar to those in case I, but development did not occur, at least not in the same region. Cyclogenesis did occur later in time and this development forms the fourth event on which our results are based. These results are discussed in Chapter 5, in which we also suggest some additional diagnostics that might be illuminating.

Chapter 1: Background

The purpose of this chapter is to summarize the different diagnostics used in previous studies of developing extratropical cyclones. The general progression we outline is from semi-empirical approaches, partly rooted in weather forecasting, to the more quantitative diagnostics of the potential vorticity perspective. We then present the potential vorticity structure of solutions to the Charney and Eady problems of baroclinic instability and show the results our diagnostics yield when applied to these models. The distinctions between these simple models will provide a useful foundation for interpreting the observed cyclogenesis cases.

Vorticity and Divergence

The diagnosis of cyclone development from observations has generally focussed on the behavior of the low level wind circulation with time. The basic approach has often been to investigate related quantities such as vorticity (the vertical component of earth-relative vorticity) or perturbation pressure (the departure from an instantaneous background field) from which the low level winds can usually be inferred. To deduce changes in either low level vorticity or surface pressure, the essential quantity is the horizontal divergence of the flow.

Works by Bjerknes and Holmboe (1944) and Bjerknes (1954)

sought to relate the vertically integrated mass divergence (which must be positive over a pressure minimum at the surface for deepening to occur) to particular configurations of waves at different heights in the troposphere. The importance of the convergence-divergence patterns associated with waves in the upper troposphere soon became apparent. Bjerknes and Holmboe were able to deduce that divergence (convergence) aloft was likely downstream (upstream) of upper level troughs. This implied a preferential phase in the large scale wave pattern for surface pressure falls (downstream of troughs) and rises (downstream of ridges). They also inferred the importance of a westward tilt with height in an amplifying baroclinic system. Ten years later, Bjerknes made a useful contribution to forecasting by identifying the qualitative shape of upper level troughs which most favored downstream divergence. These "diffluent" troughs simply had stronger winds upshear than in the downshear direction. Unfortunately, the utility of divergence as a diagnostic quantity is limited in practice. There is generally a near cancellation between divergence aloft and convergence at the surface (from inertial inflow and friction). Hence, the favorability for arbitrary perturbations to develop is determined by the small difference between two large terms. Further, divergence is itself the difference between two nearly cancelling derivatives of the wind field ($\partial u/\partial x \approx -\partial v/\partial y$), hence it is difficult to measure accurately from observations.

The diagnosis of vorticity changes also implies a need for the divergence since the vertical stretching of vortex tubes has long

been recognized as the major source of vorticity in cyclone scale systems. For inviscid, synoptic scale motions, the vorticity equation may be approximated as

$$D(f + \zeta)/Dt = -(f + \zeta)\delta \qquad (1.1)$$

where f is the Coriolis parameter, ζ is the vertical component of relative vorticity and δ is the horizontal divergence. Here, divergence need only be known at one level to estimate the Lagrangian vorticity change at that level. Equation 1.1 is usually applied in its quasigeostrophic form by neglecting ζ coupled to the divergence (setting f=constant) and approximating the substantial derivative by the rate of change following the geostrophic flow. As an alternative to estimating divergence directly from winds, it can be calculated given the vertical motion field obtained from the 'ω' (=Dp/Dt) equation (Holton p137)

$$f_0^2\omega_{pp} + \sigma\nabla^2\omega = f_0(\,\mathbf{v}\bullet\nabla\eta\,)_p + \nabla^2(\,\mathbf{v}\bullet\nabla\alpha\,) + C_p^{-1}\nabla^2(\alpha s). \qquad (1.2)$$

Here the gradient operator is two dimensional, the winds and vorticity are geostrophic, $\alpha=RT/p$, $\sigma(p)=-\alpha(\ln\theta)_p$ is the static stability parameter, $s=C_p\ln\theta$ is the specific entropy, and friction has been neglected. The omega equation, together with appropriate boundary conditions forms an elliptic boundary value problem provided $\sigma>0$ and also completes the quasigeostrophic (QG) system of prognostic equations (vorticity, ω and mass continuity). There are other ways to write the r.h.s. of (1.2), but this form of the ω equation has led to partitioning the r.h.s. as two separate effects,

"differential vorticity advection" (first r.h.s. term) and "thermal advection" (second term), (Petterssen 1955, Sanders 1971, Tsou et al. 1987). This distinction is rather arbitrary, however. That these terms tend to cancel was noted by Sutcliffe (1947) and Trenberth (1978), who both proposed the advection of absolute vorticity by the thermal wind as a useful approximation to the inhomogeneous terms.

The ω equation has since been reformulated by Hoskins, Draghici and Davies (1978) who write the r.h.s. of (1.2) as twice the horizontal divergence of a vector $\mathbf{Q}$. The advantages of the Q-vector formulation are that one can estimate the sign and relative magnitude of vertical motion (away from boundaries) from a single vector field. The Q-vector field turns out to be mostly divergent, hence $\nabla \cdot \mathbf{Q}$ is rather easily deduced in practice (Hoskins and Pedder, 1980).

Results of studies using the vorticity and omega equation diagnostics further supported the importance of ascent roughly 1/4 wavelength downstream of large amplitude positive vorticity features in the upper troposphere. Since these features were believed to exist prior to low level development, important variations in the low level structure were required which favored cyclogenesis only at certain times. Emprical findings by Petterssen et al. (1955) supported his proposed hypothesis that "cyclonic development at sea level commences when and where an area of positive vorticity advection in the upper troposphere becomes superimposed upon a frontal zone at sea level". Sanders (1971) offered some quantitative support of this by considering solutions

to the quasigeostrophic system for an idealized wavelike perturbation in the presence of vertical shear. His basic findings were:

(1) Intensification of the sea level system is associated with a low level divergence field partly in phase with the surface pressure perturbations. The stretching of vortex tubes is in turn related to vertical motion required to preserve thermal wind balance in the presence of vorticity advection increasing with height. This effect arises from the shear and westward tilt with height imposed on the perturbation in his study. The growth rate of the disturbance is found to be nearly linearly proportional to the shear.

(2) The translational velocity of the 1000mb geopotential perturbation is determined primarily by low level temperature advection (and is maximized for a warm core surface low).

(3) The maximum growth rate for a given vertical shear occurs for disturbances with wavelengths between 1500 and 3000 km.

This analysis qualitatively reproduced the results of the theoretical calculations performed earlier by Charney and Eady which we discuss later in this chapter. However, the form of the perturbations was assumed *a priori* on the basis of qualitative resemblance to observed systems.

Over time, a popular view arose that there existed two basic types of development which Pettersen and Smebye (PS hereafter) tried to define in their 1971 paper. They based the character of two prototypes of cyclogenesis on differences in the vorticity evolution at upper levels and the strength of the low level

baroclinicity. In summary, type 'A' cyclones were frontal waves having initially large amplitude at low levels compared to aloft, similar to the classical solutions obtained by Charney. Amplification at upper levels occurred later, but was viewed as a by-product of the low level development rather than an instigator.

Type 'B' developments depended on the existence of an intense upper level feature prior to surface cyclogenesis. One gets the impression that this type of development is intended to be analogous to that described by Petterssen (1955). However, PS are very unclear concerning the importance of surface baroclinicity. Low level fronts may be present in their type 'B' scenario, but PS stress the smallness of low level temperature gradients, which seems contradictory.

There are other weaknesses in the classification scheme proposed. First, for type 'A', it is not mentioned how one distinguishes between upper level wave amplification associated with the low level cyclogenesis (Sutcliffe's "self development") and growth related to other processes (local interference effects, for instance). Second, there is no clear dynamical basis for separating developments on the basis of dominance of either "vorticity advection" or "thermal advection" (Trenberth, 1978). Boyle and Bosart (1986) present a case where there is a large amplitude pre-existing upper wave, but the diagnosed vertical motion is associated almost equally with both vorticity and themal advection throughout the development. Finally, there may be other characteristics which would make this class separation of cyclogenesis more meaningful. Such quantities as phase speed,

precipitation (where it occurs relative to the cyclone and the overall influence of latent heat released in condensation) and the decay process may vary significantly depending on whether or not the amplitude aloft is initially large.

The effect of latent heat release on cyclones has also been investigated using the vorticity and ω equations (e.g., Danard 1964, Tracton 1973, Tsou et al. 1987, Gyakum and Barker 1989). For ascent in saturated, stably stratified regions (with respect to a moist adiabat), the diabatic heating may be taken proportional to ω (Haltiner and Williams, 1980). This allows the heating to be incorporated into the l.h.s. of 1.2 by introducing a modified static stability parameter, σ_m, reflecting the moist stability. A disadvantage of the ω equation consistent with QG is that no horizontal variation of σ_m is allowed, hence this amounts to reducing the stability everywhere. By not making the QG approximation, the up-down asymmetry may be included (see chapter 2).

In general, however, neither the "continuity" nor the "vorticity-ω" approach is very adept at isolating the features of the flow that are crucial to development. In addition, because vorticity has an important source in adiabatic motion, it has limited use for diagnosing the effects of condensation on cyclogenesis. Given the amount of "noise" and clutter that may be seen by even a casual glance at weather charts, one needs a way of distinguishing features and processes crucial to development in a dynamically meaningful way. This is important if we are to

compare observations to the idealized environments of theory and models of cyclogenesis. The following section describes the use of potential vorticity as a diagnostic tool for this purpose.

Potential Vorticity Diagnostics

Although potential vorticity has been used to diagnose atmospheric motions for some 50 years now, extensive application of its dynamical properties in observational work has only been made within the last decade (see HMR for a thorough review). Ertel's potential vorticity and its prognostic equation (Ertel, 1942) are defined by

$$q = \rho^{-1} \eta \bullet \nabla \theta \qquad (1.3a)$$

$$Dq/Dt = \rho^{-1} (\eta \bullet \nabla Q + \nabla\theta \bullet \nabla \times \mathbf{F}) \qquad (1.3b)$$

where ρ is the density, η is the three dimensional vorticity vector, $Q=D\theta/Dt$ and $\mathbf{F}$ is the frictional force. Hence, assuming adiabatic, frictionless motion, q is conserved following the flow.

Examination of potential vorticity in the upper troposphere and lower stratosphere (Eliassen and Kleinscmidt 1957, Bleck and Mattocks 1984 and HMR) has helped clarify the identity of the mobile upper waves often involved in cyclogenesis (Sanders 1986, 1987). These can be viewed as undulations in the tropopause, where we consider the tropopause as a surface of constant PV located in the sharp transition region between tropospheric and

stratospheric air (Danielsen, 1968). Maps of PV are often displayed on isentropic surfaces. When the r.h.s. of 1.3b vanishes, PV is conserved following the "horizontal" wind in this coordinate system. If the hydrostatic approximation is valid, this is the almost exactly the horizontal wind in geometric coordinates. Also, in q coordinates, the formula for PV reduces to

$$q = -g\,(\partial p/\partial\theta)^{-1}(\,f + \zeta_\theta\,) \qquad (1.4)$$

where ζ_θ refers to the the vertical component of vorticity computed on an isentropic surface. On such surfaces, troughs (ridges) correspond to deflections of the tropopause toward lower (higher) ambient values of PV. The height of the tropopause also varies with these disturbances, being depressed (elevated) in troughs (ridges). As shown by Thorpe, 1986, the difference in tropopause height between realistic positive and negative PV perturbations may exceed 5km.

In addition to its quasi-conservative properties, potential vorticity also determines the flow by which it is advected, hence PV a dynamically active "tracer" of air motions. The work by HMR emphasizes that given the PV distribution and certain constraints, one can calculate a unique flow associated with it. This is known as the invertibility principle. One constraint is that the calculated flow must adhere to a prescribed relation between the wind and mass fields, an example being the thermal wind equation. This constraint, known as a "balance condition", allows one to set up a

mathematical boundary value problem that relates q to the flow. A second constraint is that boundary conditions must be specified. In general, this means specifying the distribution of θ on the horizontal boundaries and some component of balanced wind on the lateral boundaries. If the domain is laterally infinite and not periodic, a reference state must be specified. Third, existence of a well posed problem requires the system to be elliptic. For inversions of Ertel's PV, this necessitates $f \cdot q > 0$, a condition which eliminates buoyant convection and symmetric or inertial instability. Therefore, by our definition, these types of motions cannot be considered as part of the "balanced" flow. The usefulness of the invertibility property of PV depends on the accuracy of the mathematical balance relation imposed.

As an application of invertibility, consider pseudo-potential vorticity (Charney and Stern 1962). Equation (1.1) may be combined with the QG thermodynamic equation to obtain a conservation statement for a scalar following the geostrophic flow (in z coordinates)

$$D_g q = D_g\{ \nabla^2\psi + \beta(y-y_o) + f_o^2\rho^{-1}(\rho N^{-2}\psi_z)_z \} = 0 \qquad (1.5)$$

Here ψ is the geostrophic stream function ($\psi=\phi/f_o$), D_g is the substantial derivative following the geostrophic motion, $\rho=\rho(z)$ is the density, $N^2=N^2(z)$ the Brunt Vaisala frequency and $\beta=df/dy$ evaluated at $y=y_o$. The expression is valid in the absence of vertical gradients of diabatic heating and when the curl of the

frictional force has no vertical component. The complete system needs boundary conditions. Assuming a flat lower boundary, we have conservation of potential temperature $D_g(\psi_z)=0$, $(z=z_0)$. At the top either a rigid lid is imposed, in which case the upper and lower boundary conditions are the same, or boundedness of the solution is required as $z\rightarrow\infty$. In many theoretical applications, the domain is periodic in x and bounded in y. The perturbation flow is usually forced to vanish on the north and south walls.

This system consists of a conserved quantity q related to the balanced (geostrophic) flow by an elliptic operator (for $N^2 > 0$). The basic scaling assumption which leads to this conservation relation is that the spatial and temporal Rossby numbers U/f_oL and $1/f_oT$ must be small compared to unity. Here, U is a characteristic variation of the flow, L is a characteristic length scale over which it varies and T is a time scale for the motion. The balance condition is a trivial algebraic expression $\psi=\phi/f_o$. In principle, given any arbitrary initial distribution of q, one can invert it to find the ψ field, advect the q field, invert again and so on. An important point is that the definition of q is a linear equation for ψ, hence we may invert any ensemble of q anomalies individually and then add them up to recover the total flow. The strength of a given q anomaly is thus measured by the strength of the balanced flow associated with it. This approach is especially useful in assessing the interaction of isolated anomalies (as in a problem with many point vortices). An example is the qualitative argument for Rossby wave propagation (Pedlosky 1979, p102 and HMR) which

utilizes the invertibility principle and the conservation of q. In addition, Bretherton (1966a) showed that the distribution of θ on the lower boundary (θ_B) is equivalent to a δ-function contribution to the interior PV just above the ground. This mathematical device allows one to think of the lower boundary θ field as part of the total potential vorticity distribution.

As previous observational work has suggested, there are likely only a few distinct PV features associated with most cases of cyclogenesis. It is therefore not our goal to dissect the flow ad infinitum, but rather to identify coherent PV distributions and assess their relative contributions to development using the concepts of invertibility and PV conservation.

We have already mentioned the upper tropospheric waves that synopticians have long associated with cyclogenesis. Other authors (Manabe 1956, Uccelini et al. 1985, Boyle and Bosart 1986, Hoskins and Berrisford 1988) have mentioned the presence of low level PV perturbations near the warm front in cyclones. All of these authors cite latent heat release as the most likely source of this low level PV. Hoskins and Berrisford (Hoskins, personal communication) have tried to estimate the contribution of such a low level anomaly of Ertel's PV found in the Eastern Atlantic storm of October, 1987, using a two dimensional semi-geostrophic inversion technique. They find the low level winds enhanced by nearly 20 ms^{-1} by this feature. There are also perturbations of θ_B which can be quite pronounced in cyclones. Although Hoskins and Berrisford find such features unimportant in the mature structure

of their case, Thorpe (1986) has shown that a realistic boundary anomaly of potential temperature can be associated with vorticity of order the Coriolis parameter.

Potential Vorticity in Simple Models

In the reconciliation of observations with the theoretical solutions for developing disturbances, PV concepts can also be of use, since most of the of the simple models of cyclogenesis yield perturbations with very distinctive PV structures (although the pressure fields may have many similarities). Of course, many variations on the original works of Charney (1947) and Eady (1949) have been studied. For simplicity, we shall consider only the classical structures in those two works as prototypes for developments involving critical layer and tropopause PV anomalies respectively.

Robinson (1989) has performed a study in which he calculates the flux of PV (and surface θ) at various levels using velocities obtained by inverting PV at other levels as well as surface θ. However, it is not clear how far this approach goes toward "explaining" baroclinic instability by addressing the issue of causality (Lindzen, 1988). It seems to give more insight into transient developments of the type discussed by Farrell (1984, 1989) or in assessing what would happen if the structure of a mode were suddenly perturbed. In dealing with modal solutions (or "phase locked" growth in the real atmosphere) we will simply try to identify consistency with certain theoretical solutions.

With the above discussion in mind we present an analysis of the Charney mode (k=2, l=1.47, N=0.012 s-1 and r=1.5 from Snyder and Lindzen 1988) and the Eady mode (k=2, l=1.47 and $S = (NH/fL)^2 = 0.5$ from Pedlosky 1979). These are designed to indicate a possible range of structures we may encounter. Figures 1.1(a) and (b) show the perturbation θ and geopotential respectively, while in (c) and (d) we have calculated ϕ' associated with the temperature perturbation at the top (c) and at the bottom (d) boundaries. We note the familiar eastward tilt with height of the thermal field and the larger westward tilt with height of the geopotential (roughly $\pi/2$ bottom to top). There is no variation of interior PV in the Eady model, hence (c) and (d) sum to the total perturbation. We see the phase shift between these two anomalies is roughly 0.4 wavelengths with warm temperatures on the lower boundary corresponding to negative ϕ' and the opposite on top. One qualitative interpretation (Bretherton 1966b, and HMR) is of counterpropagating Rossby waves at each boundary which are deep enough to "lock on" to each other. This means that there is an upshear phase shift between the lower and upper waves that allows the circulation from one to amplify the other and slow the other's propagation enough to keep the structure fixed. The downgradient heat flux at one boundary is, in fact, completely due to the presence of the θ anomaly at the opposite boundary.

The Charney mode has its own characteristic signature which is shown in figure 1.2. There are significant PV perturbations in the interior concentrated at the steering level and thermal anomalies at the lower boundary (the calculation was performed

with a lid at 4 scale heights, but thermal anomalies there are insignificant). A phase relationship very similar to the upper and lower Eady perturbations exists here between the PV at the steering level (2 km) and θ at the ground, but the interior PV has a significant phase structure of its own. HMR go through a similar kinematic arguement for this structure as well. For purposes of identifying such a structure it is sufficient to know that the main PV is at the steering level, the geopotential anomaly associated with it is comparable in strength to that of the θ_B field and the phase lag between the two is about 0.4 wavelengths.

For baroclinic growth of non-modal form, there are an infinite number of properly configured initial perturbations that will grow transiently. Farrell (1989) has removed much of this arbitrariness by seeking the initial structure that grows maximally for a given basic state in a given time, provided one specifies what norm is used to measure the amplitude. It is unfortunate that the richness of these "optimal" initial structures is not likely amenable to observational identification as Farrell points out. It is also not clear why the atmosphere should select an initial state that is optimal for growth. However, his works have emphasized the possible robustness of transient developments. The degree to which the vertical structure of the PV changes during development can be useful for determining the relative roles of transience and phase locked growth in a given cyclogenesis event.

The addition of latent heat released in the condensation of water vapor can significantly alter the structures described above.

For instance, Emanuel et al. (1987) parameterize the effect of the condensation as reducing the effective static stability to near zero in the ascent region of an Eady model. In semigeostrophic theory, this means that the moist Ertel's PV (q_e) becomes very small where air is rising and assumed saturated. A PV conservation law applies here as well, provided we define the PV in this region using θ_e as the thermodynamic variable

$$\theta_e = \theta \exp(L_v w/C_p T) \qquad (1.6)$$

where L_v is the latent heat of condensation (assumed constant), C_p is the specific heat of air at constant pressure, w is the (saturation) mixing ratio and we have ignored the effects of water vapor on the heat capacity. In fact, in a saturated atmosphere with no liquid water, q_e with θ_e on the boundaries specifies the invertibility problem for the flow (Emanuel et al.). Conservation even in the presence of gradients of diabatic heating offers a conceptual advantage over viewing the problem in terms of dry PV, for which sources and sinks would exist. However, such a state of continued saturation over an entire baroclinic wave is a rather contrived situation. Since the atmosphere is only locally saturated, different forms of PV in the saturated and unsaturated regions would be needed to have conserved quantities both places. Then one would have an internal boundary at the saturation interface along which θ or θ_e would have to be specified. This would hardly simplify the problem because the boundary would be free to move in the real atmosphere and take on very contorted

shapes.

As it turns out, the vertical derivative of the heating generally dominates the generation of dry PV, being positive below the heating maximum and negative above (eq 1.3b). As shown by Emanuel et al., the positive PV generation maximizes at the ground underneath the narrow ascent region. This updraft actually collapses to a sloping sheet in the limit $q_e \rightarrow 0$. Because the flow in the generation region is less than the wave speed, the high PV extends in the upshear direction with time (in the wave's frame of reference). The absence of diabatic heating (and friction) at the boundaries implies that the mass weighted integrated PV in the domain must remain constant (Haynes and McIntyre, 1987). The low level generation is compensated in this integral sense by destruction of PV aloft. The negative anomaly aloft is much more spread out however and is partly advected downstream by the shear flow. Both the analytical and numerical results presented in this paper reveal increased growth rates in the moist waves of about a factor of two relative to the dry waves, with no change in the phase speed.

The effects of latent heat release have also been incorporated into the Charney problem as a Wave-CISK model of cumulus heating (Snyder, 1989). The addition of such heating in the Charney problem does not always lead to enhanced growth with respect to the corresponding dry modes. The effect of such heating seems to involve the relation of its vertical structure relative to the profile of $u(z)-c_r$ (at least for small growth rates and weak heating that

obeys certain thermodynamic constraints). When PV generation occurs at the critical level, it tends to cancel the critical level PV of the dry mode and stabilize the perturbation. If the generation region is above the critical level, there is little effect of the heating; this is a regime applicable to short wavelengths. Finally if the heating maximum coincides with the critical level, there is less opportunity for cancellation and enhanced growth is possible. In general for realistic heating parameters, the most destabilization occurs when the shear is large and the heating confined to low levels.

Potential vorticity has other sources and sinks from such processes as radiation, evaporation of water and turbulent mixing. In this thesis, we will not explicitly consider the influence of these processes on cyclogenesis. The importance of evaporation in cyclones is largely unknown, perhaps because of its complexity and the difficulty of obtaining reasonable evaporation rates from data. Radiation in the troposphere has a time scale compatible with cyclogenesis only near the ground. The effect of heating (cooling) at the ground on the pressure field is nearly cancelled by the destruction (creation) of potential vorticity just above the surface. Turbulent mixing in the boundary layer complicates this picture, however. In addition, turbulence occurs in the free atmosphere and can act as a source of PV on the scale of observations, especially near the tropopause (Shapiro, 1976). Limitations of the data we use rather than the unimportance of these processes will be the primary reason for their neglect.

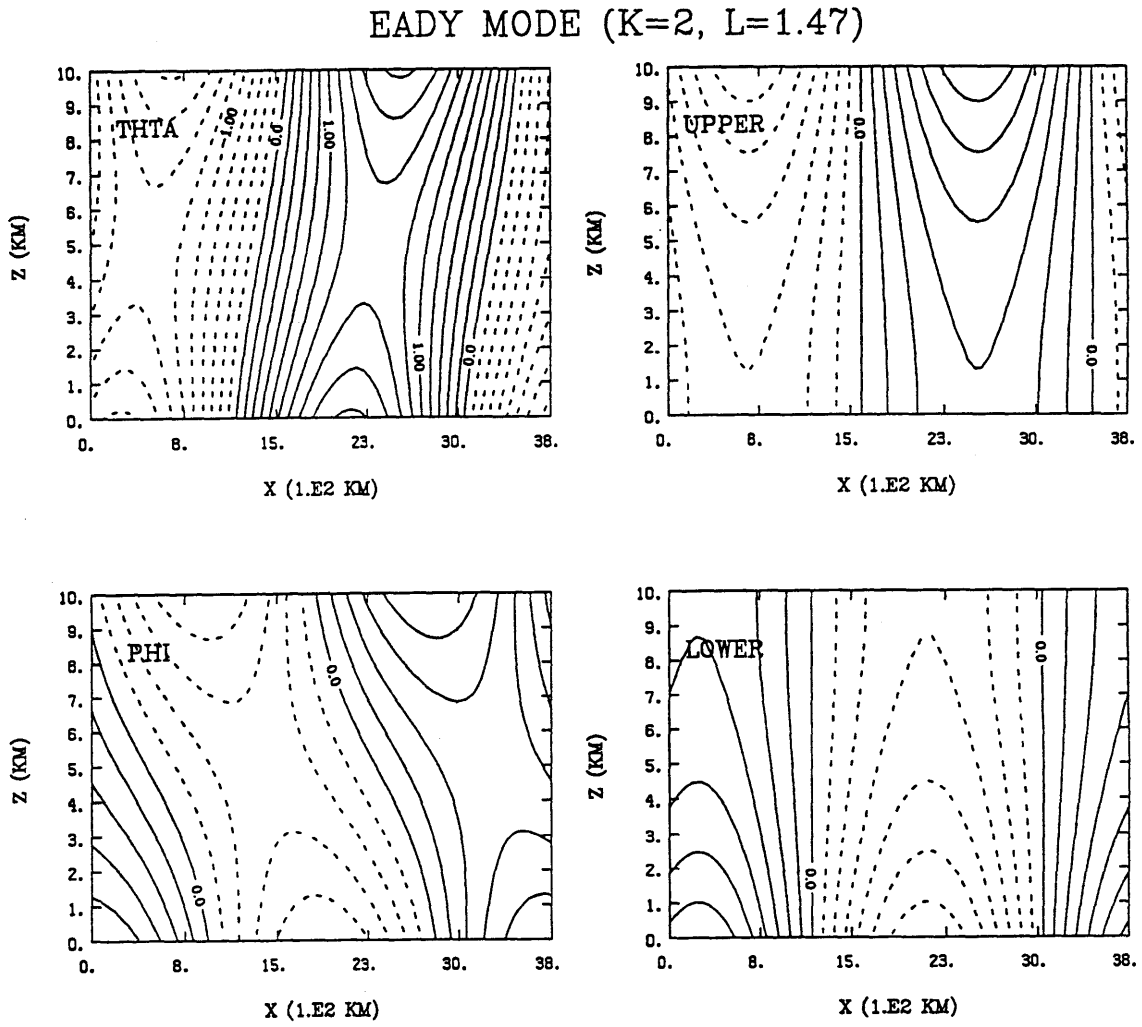


Figure 1.1 Eady mode fields; (a) potential temperature (b) geopotential perturbation (c) geopotential perturbation associated with only the upper boundary temperature perturbation and (d) geopotential associated with the lower boundary thermal field. All fields are nondimensional (linear mode amplitude is arbitrary). Contour interval for all geopotential fields is 0.2

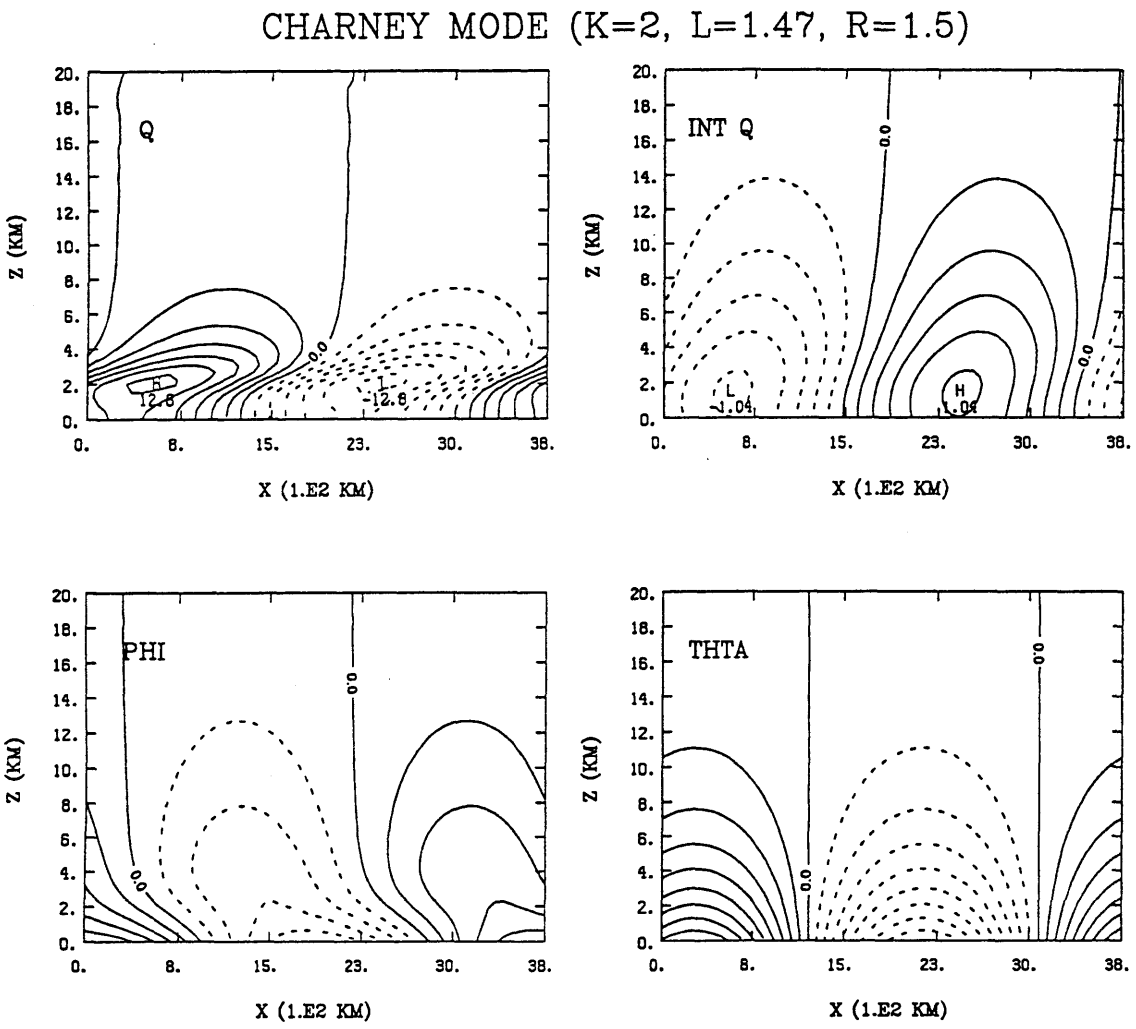


Figure 1.2 As in figure 1.1, except for Charney mode and (a) shows PV rather than potential temperature.

Chapter 2: Diagnostics

Here we present further details of the diagnostics to be used in this study. Having discussed quasigeostrophic pseudo-PV in Chapter 1, we concentrate here on developing a technique for calculating and inverting Ertel's potential vorticity. The salient feature of the diagnostic framework we develop is that we require only the potential vorticity, relative humidity and boundary conditions as input parameters.

Data and Computation of PV

An obvious disadvantage of PV is that is cannot be measured directly but rather must be calculated from the wind, temperature and pressure fields. The data we will use to do this consists of the gridded final analyses from the National Meteorological Center (NMC) (see Trenberth and Olsen, 1987 for an overview of the data and assessment of qualtity). The format is a global latitude-longitude grid with 2.5^0 spacing in both horizontal directions and 10 levels in the vertical (1000, 850, 700, 500, 400, 300, 250, 200, 150, and 100mb). The fields we will use at these levels are wind, temperature, geopotential height and relative humidity (up to 300mb) along with pressure and temperature at the earth's surface, all analyzed twice daily at 00 and 12 GMT. The initial guess for these fields consists of the 12 hour forecast of

the NMC Global Spectral Model; the primary data source is the conventional upper air and surface network, with supplementary data supplied by aircraft and some satellite information. The analysis performed on the wind and temperature is "multivariate optimum interpolation" (Lorenc 1981), but the data have not undergone a formal initialization procedure.

In this study, we will restrict our attention to cyclones over North America, which affords us the opportunity of examining the raw soundings and the surface hourly and synoptic reports on which the NMC analysis is based. Using the GEMPAK analysis package we can also perform objective analyses (single parameter Barnes' scheme) to check the PV calculated from the NMC data.

The basic calculation of potential vorticity will be done by expanding the dot product in 1.3a into three terms (ignoring the components of vorticity involving vertical velocity)

$$q = -g\kappa\pi p^{-1} (\eta\theta_\pi - (a\cdot\cos\phi)^{-1}v_\pi\theta_\lambda + a^{-1}u_\pi\theta_\phi). \qquad (2.1)$$

Here, $\pi(p)=C_p\,(p/p_0)^\kappa$ is the Exner function, $\kappa=R/C_p$, a is the earth's radius, λ is the longitude, ϕ the co-latitude and subscripts denote partial differentiation with respect to the subscript variable. We introduce the Exner function vertical coordinate because of the simplicity of the resulting hydrostatic relation (appears in a Boussinesq form). Spherical coordinates are introduced for convenience in performing calculations from latitude-longitude based data and to allow the full variation of the Coriolis parameter. From 2.1 we obtain the PV at 8 levels in the vertical

from 850 to 150mb by using centered finite differences to estimate derivatives. Appendix A provides a crude estimate of the expected error in PV from random wind and temperature errors. For this data, errors range from 0.2 PVU at low levels to 1.2 PVU in the lower stratosphere where 1 PVU = 1 m^2 K kg^{-1} s^{-1} (HMR). There is a tendency for random errors in PV over one grid volume to be cancelled out in adjacent volumes. Hence, the balanced flow, being an integral over the PV, may be relatively uneffected by small scale noise.

Given that 2.1 contains only first derivatives of observed quantities, it would have been better perhaps to stagger the grid in the vertical. The problem with this occurs at the lower boundary where we must specify the potential temperature in the invertibility problem. The 1000mb level is generally below the earth's surface in our domain and the field of 1000mb temperature in the NMC data is largely extrapolated downward given the surface temperature and low level static stability. This produces 1000mb temperatures that are not hydrostatically consistent with the height field. The reason is that the 1000mb geopotential field is calculated by integrating the hydrostatic relation downward from the surface using a standard atmosphere profile of temperature which may depart significantly from the profile just above the ground. In our calculations we will use the mean potential temperature in the layer between 850 and 1000mb as our lower boundary condition for inverting the PV. Consistent with this, we use the height field to estimate the static stability at 850mb (and

at 700mb over high terrain where 850mb is below ground). We use the analyzed winds at all levels, even where they have been extrapolated below ground.

To obtain the upper boundary condition, we integrate the static stability upward from our lower boundary θ at 925mb up to 125mb. We are, in effect, specifying the mean static stability in our domain by imposing θ at the top and bottom boundaries. If this is not consistent with the mean stability used in the computation of PV, there can be a bias in the domain integrated absolute vorticity. Of course, if the complications at the lower boundary did not exist, we could use temperatures at all levels and stagger the PV grid which would guarantee consistency between the mean stability and θ at the two boundaries.

Inversion of PV

In chapter II, we presented the inversion problem for quasigeostrophic pseudo-potential vorticity in terms of an elliptic boundary problem for the geostrophic flow given PV and θ on the boundaries. This pseudo-PV is conserved following the horizontal geostrophic flow with errors being $O(R_0)$. On the other hand, Ertel's potential vorticity obeys an unapproximated conservation relation in the absence of diabatic and frictional effects. Charney and Stern (1962) showed that as long as the Rossby number is small, the variation of pseudo-PV on a pressure surface is proportional to the variation of Ertel's PV on an isentropic surface. As pointed out

in HMR however, there are recurring situations where the variation of the two is not approximately the same. One is in frontal zones, where the slopes of the isobaric and isentropic surfaces may substantially depart from each other. Another is near the tropopause, where horizontal variations in the static stability can be first order effects. In addition the geostrophic balance assumption may suffer quantitative inaccuracies in regions of strong flow curvature. Hence, for studying real atmospheric flows, it would be useful to have an invertibility relation for Ertel's potential vorticity that is accurate in situations of large flow curvature.

The equations we develop for this purpose are based on the systematic neglect of the irrotational part of the flow compared to the nondivergent part. The balance condition we will use was first formulated by Charney (1955) and is also derived in Haltiner and Williams (1980). The procedure begins by decomposing the horizontal wind field into nondivergent and irrotational parts (denoted $\mathbf{v}_\psi$ and $\mathbf{v}_\chi$ respectively). In an unbounded or periodic domain, Helmholtz' Theorem states that such a partitioning is unique. However, as pointed out recently by Lynch (1989), in a bounded domain there can be a contribution from the harmonic field (no curl or divergence) such that $\mathbf{v}_\psi + \mathbf{v}_\chi \neq \mathbf{v}$. In realistic cases in a bounded domain, however, we shall show that the momentum of the harmonic field is quite small compared to the other two parts of the velocity field.

The Charney Balance Equation is obtained by operating with the horizontal divergence on the momentum equation and performing a scaling analysis in which terms proportional to $\mathbf{v}_\chi$ and vertical velocity are neglected compared to those proportional to $\mathbf{v}_\psi$. For the nondivergent flow we then define a stream function

$$u_\psi = - a^{-1} \Psi_\phi \qquad v_\psi = (a \cdot \cos\phi)^{-1} \Psi_\lambda \tag{2.2}$$

such that $\zeta = \nabla^2 \psi$ is the full vorticity (with the Laplacian in spherical coordinates). The resulting balance condition may be written

$$\nabla^2 \Phi = \nabla^2 \Psi + \nabla f \bullet \nabla \Psi + 2 \cdot (a \cdot \cos\phi)^{-2} \{ \Psi_{\lambda\lambda} \Psi_{\phi\phi} - (\Psi_{\lambda\phi})^2 \} \tag{2.3a}$$

where ∇ is the horizontal gradient operator. A similar scaling analysis may be used on the definition of PV (2.1) to relate q to the geopotential Φ and the streamfunction Ψ,

$$q = g\kappa\pi p^{-1} \{ (f + \nabla^2 \Psi) \Phi_{\pi\pi} - (a \cdot \cos\phi)^{-2} (\Psi_{\lambda\pi} \Phi_{\lambda\pi}) - a^{-2} (\Psi_{\phi\pi} \Phi_{\phi\pi}) \}. \tag{2.3b}$$

This equation combined with the Balance Equation forms a system of two coupled nonlinear equations. We shall refer to this as the Balance Equation System (BES) to distinguish it from 2.3a alone.

A system very similar to the BES was investigated by Charney (1962) and found to be elliptic for $q > 0$. We note that the condition for ellipticity of the Charney Balance Equation by itself as a problem for Ψ given Φ is approximately $\nabla^2 \Phi + f^2/2 > 0$ (Courant and

Hilbert 1962). This condition is frequently not satisfied in the atmosphere (Iversen and Nordeng 1982) whereas $q > 0$ is a less stringent requirement that is generally observed to hold. Even so, the PV calculated from data can be negative locally, in which case, there will be no solution to the boundary value problem we wish to pose. We therefore will set negative values of PV equal to a small positive constant well within the uncertainty of the calculated values. Support for this approach is that we have observed PV to become negative in data sparse regions more frequently than in data rich regions.

To complete the problem, we must specify boundary conditions. At the upper and lower boundaries we specify θ and the condition on Φ is just the hydrostatic equation

$$\Phi_\pi = -\theta \qquad (\pi = \pi_0 \text{ and } \pi = \pi_t) \qquad (2.3c)$$

Equation 2.3b also requires a condition on Ψ at the upper and lower surfaces. We adopt a geostrophic condition, namely

$$\Psi_\pi = -\theta/f_0 \qquad (\pi = \pi_0 \text{ and } \pi = \pi_t) \qquad (2.3d)$$

A more consistent relation might be derived from the vertical derivative of the Balance Equation, but we have found the interior solution is very insensitive to the condition imposed on Ψ since the term containing the boundary information is generally small (but kept for consistency). Indeed, the last two terms in 2.1 can be eliminated by a transformation to isentropic coordinates.

On lateral boundaries, we require the geopotential to match its analyzed value. The streamfunction is also specified on the lateral boundaries by integrating

$$\frac{\partial \Psi}{\partial s} = \mathbf{v} \bullet \mathbf{n} - \frac{\int_C \mathbf{v} \bullet \mathbf{n}\, dl}{\int_C dl} \qquad (2.3e)$$

around the edge where 'C' is a closed path around the edge of the domain, **n** is the outward facing normal and 's' implies a direction along the edge moving counterclockwise (parallel to **l**). Because there can be a net divergence of the observed wind over the domain, the integral of the normal velocity around the edge need not vanish. The second term on the right hand side of 2.3e subtracts off the net divergence so that Ψ is continuous everywhere along the edge. The constant of integration in 2.3e is supplied by setting $\Psi=\Phi$ at one point on the boundary (a similar condition was used by Iversen and Nordeng, 1982).

Method of Solution

Because the BES is coupled and nonlinear, solution even by numerical methods is not straightforward. The technique we describe below was developed largely through experimentation; however, it appears to be quite general in its ability to converge to a solution.

The complexity of the equations led us to consider an iterative method of solution, namely a modified form of successive over relaxation (SOR). To describe this procedure, we need to refer to the discretized forms of 2.3a and 2.3b. In this section, let Ψ and Φ

denote the discrete values of the streamfunction and geopotential respectively. In general, three subscripts are needed to specify a gridpoint, however, we will only use subcripts to denote locations relative to a particular point. For example, $\Psi_{i,j-1,k}$ will simply be Ψ_{j-1}. In what follows, subscripts i,j and k denote latitude, longitude and π(p) respectively. With this notation, the finite difference forms of 2.3a and 2.3b are

$$\forall^2\Phi = f\forall^2\Psi + (\Omega\cdot\cos\phi)(\Psi_{i-1}-\Psi_{i+1})/\Delta_y + (2\cdot\cos^{-2}\phi)\cdot(\Delta_x^{-2}\cdot\Delta_y^{-2})\cdot$$
$$\{(\Psi_{j+1}+\Psi_{j-1}-2\Psi)(\Psi_{i+1}+\Psi_{i-1}-2\Psi) - \Lambda\} \qquad (2.4a)$$

and

$$q = g\kappa\pi p^{-1}\{(f + \forall^2\Psi)((\Phi_{k+1}-\Phi)/\Delta_{\pi+} - (\Phi-\Phi_{k-1})/\Delta_{\pi-})/\Delta_\pi - \Theta\} \qquad (2.4b)$$

where

$$\Lambda = (\Psi_{i-1,j+1}-\Psi_{i+1,j+1}-\Psi_{i-1,j-1}+\Psi_{i+1,j-1})^2/16$$

$$\Theta = (\Delta_\pi^{-2})\cdot[(\Delta_x^{-2}\cdot\cos^{-2}\phi)(\Psi_{j+1,k+1}-\Psi_{j-1,k+1}-\Psi_{j+1,k-1}+\Psi_{j-1,k-1})\cdot$$
$$(\Phi_{j+1,k+1}-\Phi_{j-1,k+1}-\Phi_{j+1,k-1}+\Phi_{j-1,k-1})/16 -$$
$$(\Delta_y^{-2})(\Psi_{i-1,k+1}-\Psi_{i+1,k+1}-\Psi_{i-1,k-1}+\Psi_{i+1,k-1})\cdot$$
$$(\Phi_{i-1,k+1}-\Phi_{i+1,k+1}-\Phi_{i-1,k-1}+\Phi_{i+1,k-1})/16\ ]$$

and we have introduced the symbols

$$\forall^2(A) = \cos^{-2}\phi\{(A_{j+1}+A_{j-1}-2A)/\Delta_x + \cos\phi((A_{i-1}-A)\cos\phi_{i-1/2} -$$
$$(A-A_{i+1})\cos\phi_{i+1/2})/\Delta_y\};$$

$\Delta_y = a \cdot \Delta\phi$; $\Delta_x = a \cdot \Delta\lambda$; $\Delta_\pi = (\pi_{k+1} - \pi_{k-1})/2$; $\Delta_{\pi+} = (\pi_{k+1} - \pi)$;

$\Delta_{\pi-} = (\pi - \pi_{k-1})$

Our iteration begins with an initial geopotential field taken from the analysis, and initial stream function obtained by solving $\nabla^2\Psi = \zeta$, the observed relative vorticity, at each level. The iteration process we describe is nested, hence it requires two iteration indices. The superscript ω will be the "major" iteration index, and ν the the "minor" index. A major iteration cycle consists of finding a solution for $\Psi^{(\omega+1)}$, and using that solution to solve for $\Phi^{(\omega+1)}$. The minor iterations are those necessary to produce a sufficiently accurate $\Psi^{(\omega+1)}$ or $\Phi^{(\omega+1)}$ from an initial guess of $\Psi^{(\omega)}$ or $\Phi^{(\omega)}$.

A simple approach to the iteration cycle would be to solve 2.4a for $\Phi^{(\omega+1)}$ given $\Psi^{(\omega)}$ then solve 2.4b for $\Psi^{(\omega+1)}$ given $\Phi^{(\omega+1)}$ and then repeat the process until the system converged. Convergence of the system means that the equation for $\Phi^{(\omega+1)}$ is satisfied to the required accuracy on the first iteration after the insertion of the updated Ψ field ($\Psi^{(\omega+1)}$). This approach is convenient because the equations are linear for both variables at each iteration step. Unfortunately, this method does not yield convergence. We found it necessary to make each variable satisfy both equations simultaneously during the iteration process rather than one equation at a time.

The equation for the geopotential we solve is simply the sum of 2.4a and 2.4b, which is approximately a three dimensional

Poisson equation and is linear in $\Phi^{(\omega+1)}$. The equation for $\Psi^{(\omega+1)}$ is more complicated and contains the important nonlinearities in the system. This relation is obtained by solving 2.4a for Φ and plugging the expression into 2.4b. The equation one obtains for Ψ will have higest order terms of the (analytic) form $f\eta^{(\omega+1)}\,\nabla^2\Psi^{(\omega+1)}$ and $\eta^{(\omega+1)}.\Psi^{(\omega+1)}_{\lambda\lambda}\Psi^{(\omega+1)}_{\phi\phi}$, the absolute vorticity η coming from the PV equation (2.4b). At each minor iteration for the stream function, we let $\Psi^{\nu+1} = \Psi^{\nu} + \delta$ and solve for the value of δ that eliminates the error in Ψ^{ν} at each grid point. The result is a cubic equation for δ. In practice, however, we replace $\eta^{(\omega+1)}.\Psi^{(\omega+1)}_{\lambda\lambda}\Psi^{(\omega+1)}_{\phi\phi}$ by $\eta^{(\omega)}.\Psi^{(\omega+1)}_{\lambda\lambda}\Psi^{(\omega+1)}_{\phi\phi}$ which reduces the order of the equation for δ to a quadratic. If the roots of the quadratic are real, we choose the branch that would go to zero in the limit of vanishing residual. If the roots are complex, as can occur with an inaccurate initial guess, we take the real part. Complex roots do occur in the initial stages of the iteration process, but disappear as the system converges.

We make one further simplification by treating both Λ and Θ as functions of the 'ω' superscript variables alone. This implies a two dimensional relaxation for $\Psi^{(\omega+1)}$ is all that is necessary. The upper and lower boundary values of $\Psi^{(\omega+1)}$ are obtained using a forward difference approximation of 2.3d which is implemented after $\Psi^{(\omega+1)}$ is obtained over the entire domain. Hence during the iteration for $\Psi^{(\omega+1)}$ we are effectively specifying Ψ on the horizontal boundaries as $\Psi^{(\omega)}$ but upon convergence of the major

iteration cycle, we do satisfy 2.3d to the required accuracy. In the equation for $\Phi^{(\omega+1)}$, we implement the upper and lower boundary conditions directly by treating them as inhomogeneous terms (Haltiner and Williams, 1980).

For the minor iterations we generally found it useful to overrelax, even for obtaining $\Psi^{(\nu+1)}$ from the solution to the quadratic. The computations are carried out over a grid of dimension 26x45 (NS x EW), centered over North America from 12.5^0N to 75^0N. We found an optimal relaxation parameter lay between 1.7 and 1.8 for both the Ψ and Φ equations. For the major iterations it was essential to underrelax to obtain the estimates of $\Psi^{(\omega+1)}$ and $\Phi^{(\omega+1)}$. Hence for intermediate solutions $\Psi^{(\omega+1)}_0$ and $\Phi^{(\omega+1)}_0$, we calculated $\Psi^{(\omega+1)} = \alpha\Psi^{(\omega+1)}_0 + (1-\alpha)\Psi^{(\omega)}$ and $\Phi^{(\omega+1)} = \alpha\Phi^{(\omega+1)}_0 + (1-\alpha)\Phi^{(\omega)}$. We found $\alpha<1$ was necessary for convergence and that $\alpha_{optimal}$ was between 0.5 and 0.75 with considerable case to case variation. Choosing a smaller value of α was usually helpful when convergence was slow. Provided $\alpha<1$, there was no case of divergence of the iteration process, however, on occasion, there seemed no choice of parameters that would yield convergence either. In these cases, we identified points where convergence was slow and discovered these to always be in extensive regions of very small PV. Hence, we slowly incremented the PV toward higher values at these points until convergence was achieved. In practice, this required a total change in PV of less than 0.1 PVU at isolated points. Of the four cases we shall study, this was necessary in

obtaining some of the balanced fields for the fourth case only (chapter 4).

The usual test for convergence was that $|\Phi^{(v+1)} - \Phi^{(v)}|/g < 0.1(m)$ and $f_0|\Psi^{(v+1)} - \Psi^{(v)}|/g < 0.1(m)$ everywhere in the domain. For these threshold values and the grid size mentioned above, the number of major iterations needed to obtain convergence was roughly 15-20. The number of minor iterations for each major cycle began at about 100 and decreased steadily to 1. For the initial guesses described above, the calculation required approximately 6 minutes on a VAX 3500.

Since the system is nonlinear, one question is whether the approximate solution so obtained is unique (to the accuracy imposed). We can offer no formal proof of this based on the continuous equations. However, we have performed tests of the sensitivity of convergence to the initial guess and found it to be a robust property. Even with the geopotential and stream function set equal to their layer average values initially (except at the lateral boundaries), the procedure converged to same solution as with the standard initial guess, although it took twice as much computer time. We have also performed comparisons of the balanced flow obtained by the above method with the "observed" winds from the NMC analyses. Examples are presented at the end of this chapter (figures 2.1 and 2.2).

Perturbations

Having obtained a balanced wind and mass field, we are ready to dive into the central problem of calculating the contribution from individual PV and lower boundary potential temperature (θ_B) perturbations to the total flow. First, however, we must specify how the perturbations are to be defined.

We will employ two definitions here, both of which view the cyclone as a transient feature. The first identifies a perturbation as a departure from a time mean, the second, the change over a fixed time interval. Of course, difficulty arises from uncertainties in the appropriate averaging time or the best time interval over which to measure the change.

For definition one, we average over a time corresponding to a multiple of the local period of the synoptic features. For example, given a cyclone in a particular region, the averaging period would be the time it takes for the next cyclone upstream to reach that region (or a multiple of that time).

The time period appropriate for the second definition is probably the time over which the cyclone develops. If the cyclone is very weak at the initial time, the difference between the two times will reveal the growth that took place, independent of whether the perturbations are periodic.

We now develop the specific equations that will be used to relate anomalies in PV and θ_B to flow perturbations. The nonlinear

nature of the equations complicates our task. Since the focus of this analysis is on PV, we will first do our averaging on this field and then require the mean and perturbation flows to satisfy the appropriate balance relations. In this section we will be rather general in referring to mean and perturbation fields and later point out how the chosen definition of the perturbation fits into this framework.

The PV, θ_B, Ψ and Φ fields are decomposed into a mean part and a perturbation where the mean is time independent; $q=q^{(b)}(\lambda,\phi,\pi) + q'(\lambda,\phi,\pi,t)$ and the same for Ψ and Φ, where 'b' refers to means and primes to perturbations. We substitute these into 2.3a and 2.3b and group the terms that do not depend on time. The resulting equations for the mean fields are exactly the same as for the total fields. Because of the nonlinearities, $\Psi^{(b)}$ and $\Phi^{(b)}$ will generally not satisfy these equations and we must invert the mean PV to find a balanced mean flow. We do, however, use the time averaged Ψ and Φ as lateral boundary values for the balanced mean state.

The perturbation equation results from simply subtracting the mean equations from 2.3a and 2.3b. The fields of Ψ' and Φ' of course satisfy this equation by definition. Our desire now is to break up the q' field and be able to calculate the flow associated with each part of the PV individually. We introduce a much simpler, hypothetical equation system for the purposes of explaining how we go about this.

Let $q(t)=A(t)B(t)$ and assume that A and B are related by some other equation. Analogous to our preceding discussion, we solve

the total system for A and B then define an equation for the mean $q^{(b)} \equiv A^{(b)}B^{(b)}$ along with the corresponding relation of $A^{(b)}$ to $B^{(b)}$. The perturbation equation for q' is

$$q' = A^{(b)}B'(t) + B^{(b)}A'(t) + A'(t)B'(t). \qquad (2.5a)$$

Now consider $q'(t)=\Sigma_n q_n$ and the same for A and B. Substitution of these summations into the last term of the perturbation equation will result in a series of cross terms,

$$q' = A^{(b)}B'(t) + B^{(b)}A'(t) + A_1B_1 + A_1B_2 + ... + A_NB_N \qquad (2.5b)$$

where we have considered the q' field to be decomposed into N parts. Not only is interpretation of these terms difficult, but it is not clear how to proceed to generate a series of equations relating each part of the PV field uniquely to an A_n and B_n (either in a coupled or uncoupled system of equations). There are two choices for the partitioning that seem to represent the reasonable extremes of possibilities. One is

$$q_n = A^{(b)}B_n + B^{(b)}A_n + A_n(B_1 + B_2 + ... B_N) = A^{(b)}B_n + BA_n \qquad (2.5c)$$

and the other is

$$q_n = A^{(b)}B_n + B^{(b)}A_n + B_n(A_1 + A_2 + ... A_N) = AB_n + B^{(b)}A_n \qquad (2.5d)$$

We simply choose the average of these, hence

$$q_n = (A^{(b)}+A'/2)B_n + (B^{(b)}+B'/2)A_n. \qquad (2.5e)$$

This expression is invariant under exchange of A and B, a symmetry not present in the other choices. Of course another alternative is to simply drop the nonlinear terms altogether. As shown by Thorpe (1986), this is justified for some superpositions of rather intense anomalies, but not others. The deviation of the environment from

its reference state can be significant near strong PV perturbations. This is accounted for in a crude way if the coefficients of A_n and B_n contain part of the total perturbation field.

If we apply the above partitioning to our real perturbation equations the result is

$$\nabla^2\Phi_n = \nabla^2\Psi_n + \nabla f \bullet \nabla\Psi_n + 2\cdot(a\cdot\cos\phi)^{-2}\{ \Psi^*_{\lambda\lambda}\Psi_{n\,\phi\phi} + \Psi^*_{\phi\phi}\Psi_{n\,\lambda\lambda} - 2\Psi^*_{\lambda\phi}\Psi_{n\,\lambda\phi} \} \qquad (2.6a)$$

$$q_n = g\kappa\pi p^{-1}\{ (f + \nabla^2\Psi^*)\Phi_{n\,\pi\pi} + (\Phi^*_{\pi\pi})\nabla^2\Psi_n - (a\cdot\cos\phi)^{-2}(\Psi^*_{\lambda\pi}\Phi_{n\,\lambda\pi} + \Phi^*_{\lambda\pi}\Psi_{n\,\lambda\pi}) - a^{-2}(\Psi^*_{\phi\pi}\Phi_{n\,\phi\pi} + \Phi^*_{\phi\pi}\Psi_{n\,\phi\pi}) \} \qquad (2.6b)$$

where $\Psi^*=\Psi^{(b)} + \Psi'/2$ and $\Phi^*=\Phi^{(b)} + \Phi'/2$. The upper and lower boundary conditions are

$$\Phi_{n\,\pi} = -\theta_n \quad \text{and} \quad \Psi_{n\,\pi} = -\theta_n/f_0 \quad (\pi=\pi_0,\ \pi=\pi_t) \qquad (2.6c)$$

Once we break up the PV field, there are no obviously correct lateral boundary conditions to impose. We shall generally force the perturbation to vanish on the lateral boundaries, but the advantage of the data set we are using is that the boundaries can easily be pushed out one or two Rossby radii from our region of interest. Inversion over the entire hemisphere, while probably the best solution, is not practical in our case.

Tendency Calculations

The diagnostic outlined in the preceeding section is designed to determine which features in the PV field contribute most to the circulation of the cyclone and how these contributions change during the course of the development. We will also examine the origin of the perturbations of PV and θ_B and attempt to assess the importance of diabatic and frictional processes by identifying the PV generated in a nonconservative fashion.

A useful diagnostic in QG is the height tendency equation which can be obtained from the local time derivative of the pseudo PV.

$$q^{(QG)}_t = \nabla^2\Psi_t + f_0^2\rho^{-1}(\rho N^{-2}\Psi_{tz})_z \qquad (2.7a)$$

The relation of height tendency to PV tendency is mathematically the same as that between the perturbations of each at a single time. Hence, we can calculate the flow tendency associated with the tendency of any part of the PV field. There is another way to view this problem, however. From the PV equation, we can write the local tendency of PV as

$$q^{(QG)}_t = -\mathbf{v}_g \bullet \nabla q^{(QG)} + f_o\rho^{-1}(\rho Q/\Theta_z)_z + f_o\mathbf{k}\bullet\nabla\mathbf{x}\mathbf{F} \qquad (2.7b)$$

where $Q=D\theta/Dt$, $\Theta(z)$ is the reference state θ, $\mathbf{F}$ the frictional force and superscript 'QG' refers to quasigeostrophic PV. Thus we can

break up the flow and advect the total PV field with the flow due to individual anomalies of PV. We can, for example, calculate the height tendencies resulting from the advection of lower boundary θ anomalies by the flow belonging to upper level PV. There are also the nonconservative terms on the r.h.s. of 2.7b, however, at any instant, they only contain the direct effect of such processes on the PV. Anomalies already generated by diabatic heating, for example, may advect PV or boundary θ and influence development in an important way. By isolating the circulation associated with such anomalies we can obtain a more complete picture of the total effect of nonconservative processes on cyclogenesis.

The remainder of this section develops a diagnostic for the tendency of the balanced flow related to changes in Ertel's PV. The prognostic balance equations (PBE's) have been integrated or used diagnostically by several authors (Charney 1962, Krishnamurti 1968, Dimego and Bosart 1982, Pagnotti and Bosart 1984, Iversen and Nordeng 1984). Our use of this system will be more in the spirit of Charney's work since we are principally concerned with changes in PV. As pointed out by Gent and McWilliams (1983), the PBE's in physical coordinates posess an energy invariant, but do not conserve potential vorticity exactly. The inconsistency seems to stem at least partly from the neglect of the irrotational flow in the definition of PV (eq 2.3b). Charney was able to include this term in his numerical integrations by using its value at the previous time step. However, the smallness of this term's contribution to the PV at any instant makes it unimportant except

in long time numerical integrations.

The appropriate expressions for our purposes are obtained by taking a local time derivative of the BES

$$\nabla^2\Phi_t = \nabla^2\Psi_t + \nabla f \bullet \nabla\Psi_t + 2\cdot(a\cdot\cos\phi)^{-2}\{ \Psi_{\lambda\lambda}\Psi_{t\phi\phi} + \Psi_{\phi\phi}\Psi_{t\lambda\lambda} - 2\Psi_{\lambda\phi}\Psi_{t\,\lambda\phi} \} \qquad (2.7a)$$

$$q_t = g\kappa\pi p^{-1}\{ (f + \nabla^2\Psi)\Phi_{t\,\pi\pi} + (\Phi_{\pi\pi})\nabla^2\Psi_t - (a\cdot\cos\phi)^{-2}(\Psi_{\lambda\pi}\Phi_{t\lambda\pi} + \Phi_{\lambda\pi}\Psi_{t\lambda\pi}) - a^{-2}(\Psi_{\phi\pi}\Phi_{t\phi\pi} + \Phi_{\phi\pi}\Psi_{t\phi\pi}) \} \qquad (2.7b)$$

We shall treat the terms not differentiated in time as known, non-constant coefficients whose values are obtained from the solution to the BES. In our numerical solution, this is equivalent to taking one forward time step.

A complication here, relative to the QG case, is that we must allow for advection of PV vertically and by the irrotational part of the wind in addition to advection by the nondivergent flow. To determine ω and $\mathbf{v}_\chi$ ($=\nabla\chi$ where χ is the velocity potential), we need two more equations. One of these is a modified ω equation (presented in Iversen and Nordeng 1984, p2050 with b=1, c=d=0 in their parameter list) and the other is continuity. The equation system can be written schemtically as

$$\nabla^2\Phi_t - L_1(\Psi_t) = 0 \qquad (2.8a)$$

$$q_t = L_2(\Phi_t) + L_3(\Psi_t) \qquad (2.8b)$$

$$L_4(\omega) = F(\Phi,\Psi,\Psi_t,\chi) \tag{2.8c}$$

$$\nabla^2\chi + \pi^{1-1/\kappa}\left(\pi^{1/\kappa-1}\omega\right)_\pi = 0 \tag{2.8d}$$

where each L_i denotes a linear operator that in general depends on the balanced Ψ and Φ. For the ω equation, we stagger the vertical discretization with respect to the mandatory levels. The progostic equation for PV (1.3) is used to determine the local tendency from advection (by ω, $\mathbf{v}_\psi$ and $\mathbf{v}_\chi$) and from friction and gradients of diabatic heating.

The above system is solved by a simultaneous relaxation method for the four quantities Ψ_t, Φ_t, ω and χ. We set each of these equal to zero on the lateral boundaries (see Gent and McWilliams for a more accurate set of lateral boundary conditions). At the top and bottom, we use the thermodynamic equation to calculate θ_t and from 2.3c and 2.3d, this determines the lower boundary condition for Ψ_t and Φ_t. Because of the staggered grid for the ω equation, the vertical velocity does not vanish where we apply the thermodynamic boundary conditions. We set ω=0 at 75mb and prescribe its value at 1000mb according to a topographic condition described as follows.

We calculate a frictional velocity at the surface by interpolating the balanced geostrophic wind to the pressure at the surface of the earth, then requiring a three way balance between the Coriolis, pressure gradient and frictional forces. The form of the friction is linear in velocity with a coefficient that varies in space chosen to give the observed angle (μ) between the surface

gradient and frictional velocities. For $\mathbf{F}=-\alpha(\lambda,\phi)\mathbf{v}$, $\mu=\arctan(\alpha/f)$, with α chosen such that $\mu \approx 30^{\circ}$ over land and 10° over water. There is also a dependence of α on the surface pressure, such that μ can be as large as 40° over high terrain. No attempt has been made to accurately model the flow in the presence of realistic topography or the true physics of turbulence in the boundary layer. Given the frictional velocity and distribution of the surface Exner function (π_s), we calculate the surface vertical velocity $\omega_{topog}= -\mathbf{v}_{fric}\bullet \nabla\pi_s$. We also calculate the horizontal divergence of $\mathbf{v}_{fric}$ at the surface and use the continuity equation to extrapolate ω from there to the 1000mb level (holding the divergence constant). The complete lower boundary condition for ω is then $\omega_{1000mb} = \omega_{topog(1000mb)} - (\theta)^{-1}(\partial\Phi/\partial t)|_{1000mb}$ where the last term represents the height tendency of the 1000mb surface.

The values of ω and $\mathbf{v}_{\chi}$ at the levels where the thermodynamic equation is applied will change with each iteration. Hence, θ_t will also change which in turn means that the lower boundary condition for Ψ_t and Φ_t is allowed to evolve during the iteration process. This does not introduce problems in the convergence of the system, however, since the dominant local change of boundary θ is by far from horizontal advection by the nondivergent wind (except perhaps near topography).

A final point concerns the treatment of nonconservative processes. We have discussed a crude implementation of friction at the lower boundary, but will ignore any friction or subgrid scale

mixing in the interior. As pointed out by Shapiro (1976) and recently reviewed by Keyser and Rotunno (1990), transports of heat and momentum by subgrid scale eddies can lead to sources and sinks of PV on the gridscale. The region on the cyclonic shear side of strong upper tropospheric jets (where the Richardson number often is < 1) appears most susceptible to this "generation".

Our main concern regarding nonconservative processes will involve latent heat released in stably stratified, saturated ascent since we can include this process with a minimum of parameterization. As shown in Haltiner and Williams (1980) the heating from condensation may be expressed as ω times the variation of θ with pressure on a moist adiabat.

As mentioned in chapter 1, diabatic heating of this form can be incorporated into the l.h.s. of the omega equation. The modified equation has no explicit heating term, rather, the static stability is replaced by a "moist" static stability which is zero if the real lapse rate is moist adiabatic. This modified stability is only implemented in regions of saturated ascent, the locations of which are not known initially. Although we have relative humidity analyses, the areas of ascent must be discovered through the iteration process. At each pass through the grid in our numerical relaxation, we check for both ascent and saturation and use the moist stability if both conditions are met. Our saturation threshold is a relative humidity of 80%, a value which usually covers the regions of falling precipitation. Rawinsondes generally do not measure 100% relative humidity even in clouds.

Furthermore, moisture analyses tend to be too dry near the edges of precipitating regions because of the interpolation scheme used. Our results are not sensitive to the choice of saturation threshold as long as it is between 70% to 90%. However, as we increase the threshold above 90%, the area of saturation becomes significantly reduced. At low temperatures we reduce the threshold relative humidity to crudely account for the presence of ice (the threshold value is a bit less than 60% at the tropopause).

A technical point is that the levels of analyzed relative humidity do not correspond to the levels at which omega is calculated. The humidity we use to determine the existence of saturation is that from the next mandatory level above the omega level. Humidity analyses were not available above 300mb. For these upper levels, the air was assumed saturated if the same column was saturated at 300mb and if the level was in the troposphere ($q < 1.5$ PVU).

The ellipticity of the ω equation depends on the effective static stability being positive. However, to be consistent with balanced motion, we really should require the moist PV to be non negative in regions of saturated ascent. From 2.1 (with θ replaced by saturation θ_e), we solve for a second moist stability assuming $q_e=0$ and keeping the absolute vorticity and the last two terms in 2.1 fixed. This second stability (associated with zero moist potential vorticity) is used if it is larger than the actual moist stability.

Examples

We now present two examples of the inversion techniques outlined in this chapter. For each of these, we first calculate potential vorticity from the NMC data as described in the first part of this chapter. The remaining calculations are performed using only the PV distribution, the relative humidity analysis and boundary conditions. In both figures 2.1 and 2.2, the observed winds from the NMC data appear in the upper right panel. The upper left plot shows the balanced nondivergent winds ($\mathbf{v}_\psi$) at the same level. The middle left hand figure shows the irrotational part of the flow ($\mathbf{v}_\chi$) calculated from the PBE's (2.8) and the lower left figure shows $\mathbf{v}_\psi + \mathbf{v}_\chi$.

Figure 2.1 presents the winds at 850mb for 00Z (=00GMT) 15 December 1987 which happens to be a time during the development of the case studied in Chapter 3. From figure 2.1e, we see that most of the difference between the observed winds and $\mathbf{v}_\psi$ has a clear divergent signature. Figure 2.1f shows that the divergence we calculate accounts for a good deal of the difference in figure 2.1e. Remaining discrepancies are mainly confined to regions of significant topography over Western North America. It is not clear how much of the difference in figure 2.1f can be attributed to real topographic effects (creating unbalanced motion) and how much to extrapolation of data below ground.

Figure 2.2 shows winds at 300mb for 12Z 27 December 1987 in

the same format as figure 1 (except the divergent winds and difference fields are scaled by a factor of 4). Despite the complicated flow pattern, $\mathbf{v}_\psi$ agrees very well with the observed winds. There is a great deal of deformation in this flow, but little divergence. On the other hand, the ageostrophic winds at this level (not shown) are quite large in places. We note that the vector difference in 2.2(f) is small and furthermore, that the part of the residual without curl or divergence is even smaller. Thus, even though the domain we use is bounded, Helmholtz' Theorem still appears approximately valid.

The relative discrepancies between the balanced and observed winds appear much smaller in this second example. This is true in general when comparing upper and lower balanced winds, perhaps because of the effects of topography and surface friction. In addition, deep convection was occurring at the time of the first example, but not in the second. The neglect of the irrotational flow compared to the nondivergent flow at low levels was a poorer approximation in the first case. In fact, these two illustrations of our technique probably represent the range of accuracy of our balance assumption. These examples serve to indicate that the balance approximation we have chosen is adept at handling very complicated synoptic scale flow configurations with no restrictions on shear or curvature (aside from the conditions for ellipticity of our system). With the diagnostic tools discussed in this chapter, we now begin the examination of four cases of cyclogenesis in detail.

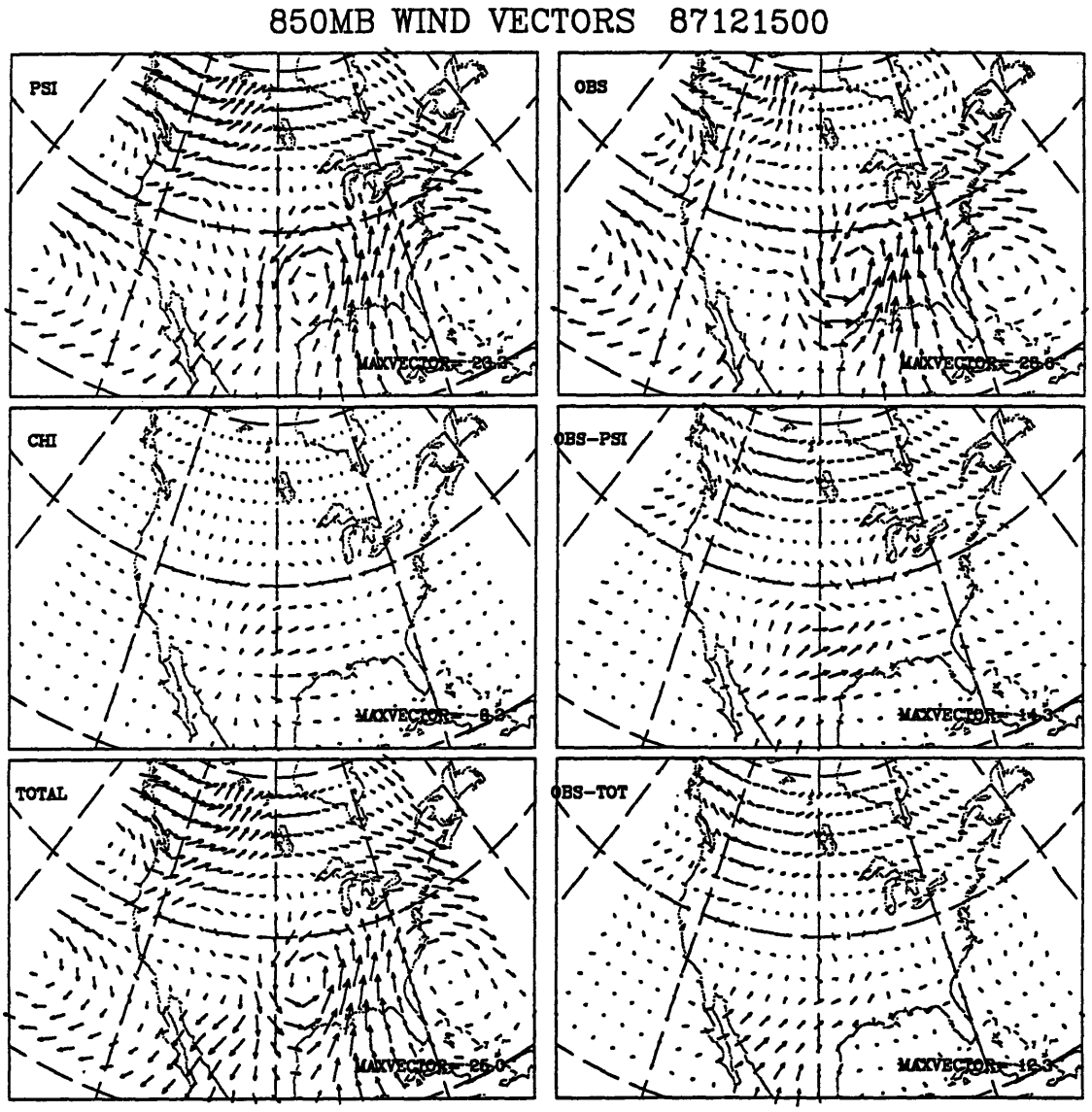


Figure 2.1 Winds at 850mb for 00GMT 15 December 1987. For this and all multipanel plots in this thesis, (a) is at upper left and we increment alphabetically downward. Hence, (c) is bottom left, (d) is top right in this case. Also note that on all vector-plots, the maximum vector magnitude will be plotted in the lower right corner. Another general convention used will be to plot latitude and longitude lines 20^0 apart with values always being multiples of 20^0. Continental outlines will appear with dotted lines. For orientation, the approximate latitude and longitude at the center of each figure will be given; here, the center is near 40N, 100W. For this plot we have (a) v_ψ; (b) v_χ; (c) $v_\psi + v_\chi$; (d) NMC analyzed winds; (e) d-a; (f) d-c

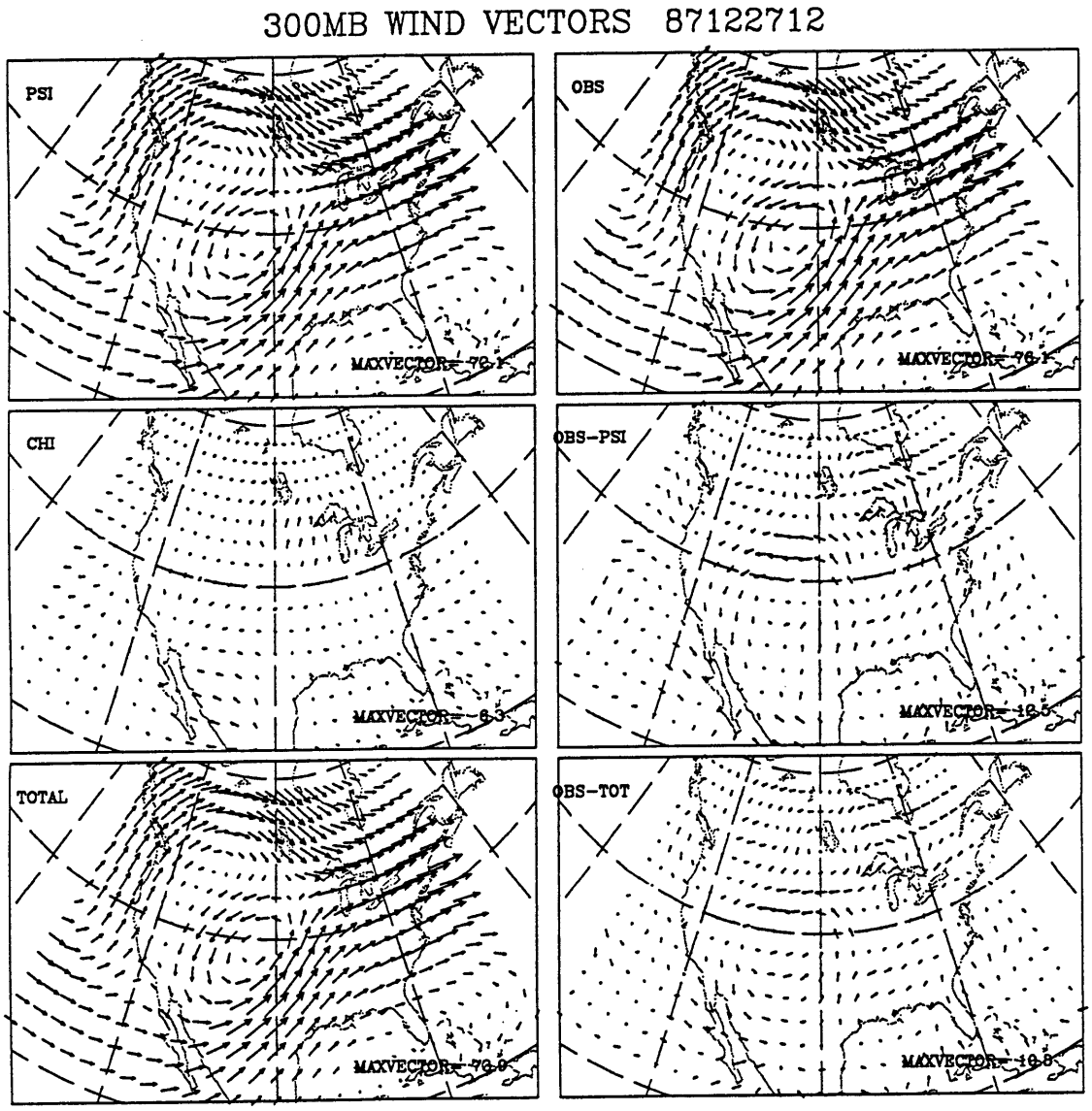


Figure 2.2; Winds at 300mb for 12GMT 27 December 1987. Conventions as in figure 2.1 except the fields in b, e and f have been scaled by a factor of 4 relative to the fields in a, c and d.

Chapter 3: Case I; December, 1987

The first case of development we present occurred between 00Z (same as 00GMT) 14 December and 12Z 15 December over the central United States. This event was chosen both because of its robustness and because it remained within a region of relatively dense data coverage. Though a strong cyclogenesis, there are many cases published in the literature which occurred in this area that are at least as intense (Pettersen et al. 1955, Palmen and Newton 1969). To the extent that published data allows comparison, the structure and evolution of this case is broadly similar to some of these other developments.

Figure 3.1 summarizes the evolution of the balanced low level circulation and lower boundary potential temperature field (θ_B). The winds are the average of $\mathbf{v}_\psi$ at 850mb and 1000mb (frictional velocities not included) and θ_B represents the mean potential temperature in the same layer. At 00Z the 14th, there was significant damming of cold air in the lee of the Rockies, a rather common occurrence preceding midwest and Gulf Coast cyclone developments (Saucier, 1949). To the east of this, a cyclonic circulation began to spin up on the southern edge of the strong baroclinic zone in phase with a warm perturbation in the thermal field. The circulation center moved northward to 40N, 90W by 12Z the 15th at which time the wave in the thermal field appeared quite amplified. This thermal pattern moved offshore by

12Z the 16th, when we note another low level cyclonic circulation, once again in phase with the warm anomaly at the lower boundary.

There were large amounts of precipitation associated with the main development, both of the convective and stratiform type. Figure 3.2 shows 24 hour precipitation totals (12Z 14 to 12Z 15) over the central United States along with radar summaries at 0035Z and 1135Z on the 15th. Deep convection in a developing squall line is evident over Arkansas, near and just to the south of the cyclone position. Tracton (1973) frequently found the occurrence of deep convection near the center of incipient cyclones in this region. There is also a great deal of stratiform precipitation to the north and northwest of the system with isolated deeper cells. Precipitation totals exceeding one inch in 24 hours were common in the stratiform region (much of which fell in 8 to 12 hours). The report of 4.21 inches of precipitation at Oklahoma City (OKC) is erroneous (the actual total is unknown, though likely about 3/4"). When 24 hour totals are unavailable from stations, the six hour totals (ending at 12Z the 15th) are plotted instead. This accounts for the very small total at Kirksville, Missouri (0.22") for example.

For the evolution at middle and upper levels, we display the PV on the 315K and 295K isentropic surfaces in figure 3.3 and 3.4. Isentropic analyses were produced by linearly interpolating (in θ) the mandatory level winds and pressures. Potential vorticity was then calculated from equation 1.4. First the relative vorticity was computed from centered finite differences of wind on θ. The

Coriolis parameter was added to this and the result multiplied by the static stability over a layer of 10K extent. The 315K surface is convenient for displaying the upper tropospheric waves, the 295K surface for interior tropospheric PV anomalies.

The 315K winds and PV taken together show a highly amplified system over western North America at 00Z the 14th, with a short wavelength ridge centered near 50N, 130W and a deep trough located near longitude 115W. Note that the winds are very nearly parallel to the PV at this time, and the slow eastward progression in the 12 hours thereafter suggests that PV advection is indeed weak despite strong winds (over 60 ms^{-1}) and large horizontal PV gradients near the tropopause. By 00Z on the 15th, there is significant advection evident especially near 110W on the upstream side of the trough. We can also note the appearance of a short wavelength system on the West Coast about this time and the pronounced weakening of the western ridge and "sharpening" of the ridge east of the trough. After this time, there is a rather spectacular wrap up of the PV field over Eastern North America.

A fairly obvious but important point is brought out by the above figure, namely, that variations of potential vorticity on scales much smaller than a deformation radius are not apparent in the balanced winds. This fact may pertain directly to the rapid eastward acceleration of the southern end of the intense upper trough after 12Z the 14th. The net effect of the aforementioned upstream shortwave feature impinging on this trough seems to have been an overall reduction in zonal scale of the PV. The

integral over this distribution does not reflect the presence of the smaller scale wave; hence it yields an almost straight northwesterly current on the upstream side of the major positive PV anomaly. The flow is substantially across the PV contours on the southern end of the trough, and rapid advection downstream is henceforth evident.

The important feature at 295K is the positive PV anomaly that becomes prominent near 42N, 90W by 12Z the 15th. The fact that it is a pronounced maximum of PV on an isentropic surface, far removed from any comparable values, suggests a nonconservative origin. Its near coincidence with a region of rather heavy stratiform precipitation would imply a diabatic influence in the generation. In addition, one may note from figure 3.3 that there is a substantial loss of PV in the upper trough between 00Z and 12Z the 15th. The area of enhanced low level PV coincides nicely with the area of reduced PV aloft. This is a sign of the expected influence of diabatic heating at levels between those shown (HMR, Haynes and McIntyre 1987). PV is destroyed aloft, created below, and the mass weighted volume integral must be conserved. Haynes and McIntyre refer to this process as dilution and concentration of PV, an interpretation which appeals to the similarity between PV and the mixing ratio of a tracer in its conservation equation. Above the heating maximum there is addition of mass to isentropic layers (dilution) and a removal of mass below (concentration).

Another view of the PV evolution may be examined via a

cross section analysis (figure 3.5). Shown are longitude-"height" cross sections constructed for the first four times shown in the previous three figures. The vertical coordinate is actually the pseudo-height (Hoskins and Bretherton 1972), which varies as $(1 - \pi(p)/\pi_0)$. Note that the physical height is greater than the pseodo-height for the parameter choices used in Hoskins and Bretherton (the ratio is about 1.2). The ordinate labels correspond to the mandatory levels and they have been plotted evenly spaced. The basic structure of the trough strongly resembles the prototypical solutions obtained by Thorpe (1986) for cold anomalies both at the tropopause and at the surface. However, the features in this case are stronger than in Thorpe's, a point to be quantified in the next section. Taking the 1.5 PVU contour as the tropopause (HMR), we see that it varies in elevation over a range greater than 7km in physical coordinates. The shortwave upstream of the trough also appears as a small scale tropopause undulation by 00Z the 15th. By 12Z the 15th, there is a column of high PV air that extends throughout the troposphere near 90W. A similar "PV tower" has also been observed by Hoskins and Berrisford (1988) for the Eastern Atlantic storm of October, 1987.

Quantitative Contributions

Given the observed structures of PV noted above, we now wish to determine how these features contribute individually to the total perturbation flow. The "importance" of any given feature

is judged either by its direct contribution to the cyclone flow field, or by its importance in amplifying other significant PV anomalies. In principle, with the "Green's Function" technique outlined in Chapter II, the only limitation to the fineness of our decomposition of the PV field is the resolution of the data. However, the key question in practice is how to choose perturbations that have dynamically significant identities.

Observational and theoretical studies referred to in Chapter 1 suggest that partitioning in the vertical may be the most physically relevant. Hence, that will be our starting point for identifying perturbations. As an example of our technique, we present figures 3.6 and 3.7 which show the perturbation vorticity at 850mb associated with q' at various levels for 12Z 15 December. In this case, perturbations were computed as the departure from a five day average over the period 00Z 14 to 12Z 18 December. We choose 850mb as the lowest interior level for which the balanced nondivergent streamfunction is available. Figure 3.6 shows results for the balance equations, 3.7 displays the results of an inversion of QG pseudo-potential vorticity. For calculating QG pseudo-PV we have used the geopotential obtained from the BES solutions. Results are very similar using the observed heights, but there is more noise especially with the contributions from low level PV.

In 3.6, the largest single contribution to vorticity is from the lower boundary thermal anomalies with maximum postive values as large as the Coriolis parameter (middle right of top left figure). A broad region of negative relative vorticity is found between 110W

and 90W. From the 850mb PV, we note a strip of positive vorticity embedded in the frontal zone near 42N, stretching from 95W to 75W. Negative contributions to vorticity are found elsewhere over the eastern states. The vorticity associated with PV at higher levels gradually loses detail, as one would expect from the character of the equations. We note, however, that these fields are nearly in phase, especially concerning positive vorticity.

The QG calculation, on the other hand, strongly emphasizes the positive low level PV perturbation near the cyclone center. At this point the actual relative vorticity is 1.6 times the Coriolis parameter and the circulation is embedded within a strong baroclinic zone. It is likely that we have overstepped the bounds of quasigeostrophic validity. However, good agreement between figures 3.6 and 3.7 is apparent in most other places. Indeed, the same comparison as above shows much better agreement between the two methods in the early stages of development.

We shall hereafter only discuss inversions of Ertel's PV. From figure 3.6 and the structure of PV already presented, a simplification of the perturbation structure is suggested. Since contributions from 700mb and up are nearly in phase, we group q' at these levels into a single anomaly. Before 12Z the 15th, there were no significant PV anomalies at 700mb. Its inclusion in the "upper" PV is supported by figure 3.3d and by its difference in structure from the lowest level PV anomaly. The amalgamation of PV at several levels is necessary if we wish to talk about all perturbations associated with the dynamic tropopause.

Although the θ_B and low level PV fields do not have a well defined phase relation, they are intimately related dynamically. By grouping these together, however, we cannot hope to identify structures such as the Charney mode (Chapter 1) if they exist. The perturbation at 850mb does not grow significantly as the θ_B perturbations amplify, however. Rather, the low level PV becomes elongated along the isotherms in the frontal zone. In view of the close relationship of the low level PV to the surface front and thus to the θ_B field, we shall group these two fields together as a second perturbation. In some of the other cases we examine, it will be useful to examine low level PV and θ_B anomalies separately.

We now discuss the time history of the contributions of the two perturbations to the low level vorticity. Figures 3.8 and 3.9 reveal the time sequence of the 850mb signature of the "lower" and "upper" perturbations respectively. The signature of the lower perturbations (θ_B and q' at 850mb) shows a growing perturbation that is roughly stationary east of the Rocky Mountains between 30N and 35N until 00Z the 15th. The positive vorticity feature moves northeastward to 40N, 85W by 12z on the 15th at an average speed of 20 ms^{-1}. This motion is also indicated by the thermal wave in figure 3.1 and indeed, much of the vorticity shown in this figure is related to lower boundary thermal anomalies. The maximum positive contribution by 12Z the 15th is about $1x10^{-4}$ s^{-1}. The secondary coastal development is clearly seen by 00Z the 16th near

40N, 75W.

The remainder of the perturbation vorticity is associated with the "upper" PV and is presented in figure 3.9. There is a marked signature of the upper positive PV anomaly in the vorticity field as it moves eastward from the southwestern United States. The initial weakening of the vorticity contribution is not so much a reduction of perturbation PV as it is a reduced "penetration depth" in the lower troposphere. If we replace Ψ^* and Φ^* in eq. 2.6 with their layer average values and repeat the calculation, we remove much of the difference between the extrema in low level vorticity at 00Z and 12Z on the 14th. The maximum positive vorticity values are reduced to roughly 3.5×10^{-5} s $^{-1}$in this calculation, whereas negative values are relatively unchanged. Following this time, we see enhanced negative vorticity to the east of the trough, a reflection of the growing upper ridge. By 12Z the 15th, the maximum positive vorticity is roughly 1×10^{-4} s $^{-1}$ and the minimum is -4.5×10^{-5} s $^{-1}$ located near 42N, 80W. Because of the difference in elevation between the positive and negative PV perturbations aloft (figure 3.5), the magnitude of the low level negative vorticity associated with the upper ridge is quite remarkable. The increase of the positive vorticity signature between 00Z and 12Z the 15th results from the rearrangement of PV from higher to lower levels, likely associated with latent heat release.

We can see this rearrangement in figure 3.10 which shows the contributions from individual levels to the total 850mb vorticity signature of the upper anomaly over the central U.S. For

each time shown in figure 3.9, we have integrated the vorticity associated with PV at each level over an area that is roughly enclosed by the $2x10^{-5}$ s^{-1} vorticity contour and centered on the maximum value. Note that figure 3.10 does not show the vertical structure of the PV anomalies, but rather of their contributions to the cyclonic circulation at 850mb. The salient feature is the decrease with time of the level of maximum influence, beginning near 400mb at 00Z the 14th and ending at 700mb by 12Z the 15th.

Another look at the evolution of these two perturbations is presented in figures 3.11 and 3.12. Shown are cross sections of the balanced geopotential height perturbations from the lower and the upper anomalies as well as the total fields. Figure 3.11 shows the structure at 00Z (left) and 12Z (right) on the 14th while figure 3.12 has the same layout except for 00Z and 12Z 15 December. As can also be seen in figures 3.7 and 3.8, the phase relation between the upper and lower anomalies is evolving throughout the development such that by 12Z the 15th, the superposition of the two circulations at low levels is significant. The minimum in the 1000mb geopotential is -320m and the largest negative contributions from the upper and lower anomalies individually are about -200m and -230m respectively. Performing an integration of vorticity contributions over the total 850mb positive vorticity perturbation (method analogous to that used in figure 3.10), we find roughly equal influence from the upper and lower anomalies. Therefore, the transient superposition of anomalies was significant in this case.

Further inspection of figures 3.11 and 3.12 reveals that although superposition was important (especially in vorticity), the meridional geostrophic (and balanced) low level flow is in phase at all times with the growing lower anomaly. The increase of the meridional flow associated with the upper PV is due to the explosive growth of the downstream ridge aloft coincident with the redistribution of the positive PV to lower levels. The structure of this development was such as to allow growth of the lower anomaly by advection on the basic gradient of potential temperature, in conjunction with the favorable superposition of the upper level feature.

Origin of Perturbations

We have seen the structure and evolution of PV for this case and have identified the important perturbations and assessed their quantitative contributions to the flow. We now consider the origin of these features.

In figures 3.11 and 3.12, we saw evidence for the importance of the upper anomaly in the development of the lower perturbation. Further evidence is presented in figure 3.13 which shows θ_B and the low level winds associated with the upper perturbation. East of 100W, we see the increasing southerly flow associated with the upper trough is in phase with the developing thermal anomaly. The winds associated with the lower anomaly field (figure 3.14) show a strong northerly component to the west of the warm thermal

anomaly that is offsetting the warm advection associated with the upper PV. In fact, this flow is acting to amplify the cold phase of the thermal perturbation, not the flow from the upper PV. By 12Z the 15th we have significant low level frontogenesis taking place east of the Appalachians, after which the thermal anomaly propagates rapidly eastward along this gradient in the manner of a surface Rossby wave. We should point out that the low level frontogenesis and damming of cold air east of the Appalachians (Bell and Bosart, 1988) is a process we cannot hope to capture adequately with the balance equations we are using. There is considerable evidence for inherently mesoscale features playing an important role in some coastal cyclogenesis events in this region (Bosart 1981, Pagnotti and Bosart 1984). Still, it may be possible to view this example of secondary cyclogenesis on the East Coast as simply the separation of the low level thermal anomaly from the low level vorticity image of the upper PV.

The large amplitude of the upper level feature at the beginning of low level development implies that we must consider prior events to gain some insight into its origin. In figure 3.15 we show the 315K PV over the Eastern Pacific for the 4 synoptic times preceding 00Z 14 December. Since most of these fields are produced from the first guess field of the analysis, we will only concentrate on the gross aspects. The development of the high amplitude upper PV wave pattern over Western North America occurs during the period shown. The sequence of events are quite reminiscent of the downstream development simulated by Simmons

and Hoskins (1979). For reference in these plots, the date line is the left most longitude on which data appears and latitude and longitude lines are 20^0 apart. At 00Z 12 December, we see a high amplitude meridionally elongated trough near 170W. Deformation acts to decrease the zonal scale and the eddy aquires a southwest-northeast tilt. The southwesterly jet ahead of the trough is enhanced and low PV air is advected northeastward. The subsequent downstream ridge and trough developments occur nearly simultaneously. The labelling of these events as "downstream development" only means that the above scenario may be consistent with the concept of group velocity. The important point is that the upper PV pattern was "preexisting" as concerns this case of cyclogenesis.

Another question is whether the eventual wrap up in the upper PV (figure 3.3) was influenced significantly by the circulation associated with the lower anomalies. To address this point, we need to consider the PV on all upper levels at once. For this purpose we introduce the concept of a tropopause map, the distribution of potential temperature on a constant PV surface (1.5 PVU). Inspection of isentropic distributions of PV and winds indicates that upper level waves and vorticies primarily manifest themselves as perturbations in the location of the tropopause. Thus, to first order much of the information on a θ surface is contained in the location of a single PV contour. We can then compact the information of the three dimensional PV structure by plotting the 1.5 PVU contour from each θ surface on the same map.

This θ distribution is conserved following the horizontal wind on the tropopause. As shown by Thorpe (1986), in the limiting case of negligible tropospheric and stratospheric variations of PV, tropopause θ (θ_T) and surface θ determine the balanced flow uniquely. In the limit of infinite stratospheric PV, the tropopause becomes a lid as in the Eady basic state.

Figure 3.16 shows tropopause θ and the winds from the lower perturbations (left) and the rest of the balanced winds (right). Values of θ are calculated by interpolating the potential temperature on mandatory levels linearly onto the q=1.5PVU surface. This method assumes that PV increases monotonically with height, that is, if the tropopause is encountered more than once in any vertical column, only the largest value of θ is selected for display. We have also subtracted out the motion of the cold tropopause anomaly from the winds in the right column figures. It can be seen that the low level anomalies have very weak winds on this surface except where θ is low (note these vectors are scaled up by a factor of three relative to the "upper" flow field). At 12Z the 15th, the flow pattern from lower perturbations is such as to enhance the gradient of θ south of the cold anomaly and weaken it to the north. Under most circumstances, this would result in strengthening and weakening of the jet to the south and north respectively.

It is fairly evident, however, that the wrap up of PV has little to do with the low level PV and θ anomalies. Note especially at 12Z the 15th, the relative westward advection of high θ values

north of the cold anomaly. This suggests that some of the wrap up is advective in nature. However, we will present evidence in the next section that supports an important contribution to this evolution from diabatic heating as well. A final point evident from these analyses is their utility in deducing the occurrence of upper level frontogenesis, as takes place to the northeast of the cold anomaly between 80W and 60W. Since θ is conserved following the "horizontal" motion on a constant PV surface, it reduces the problem to two dimensions.

Diabatic Effects

As we have already mentioned, condensation may have had a significant influence on the vertical redistribution of positive PV anomaly during the development of this case. The difficulties in quantitatively assessing whether the observed PV changes are associated with a particular process such as latent heat release in stable ascent are great. The Lagrangian trajectories of air parcels must be known, as well as the generation rate along those trajectories. The spacing in time of the upper level data we are using probably does not allow the calculation of trajectories sufficiently accurate to determine these. Accuracy is crucial because of the rapid spatial variability of the regions of condensation.

The isentropic analyses of PV (3.3, 3.4) strongly indicate the presence of sources and sinks of that quantity. Our goal here is to

offer some evidence of quantitative consistency between the effects of condensation and the changes of PV observed. We will not attempt to account for convective effects as other authors have done (Tracton 1973, Gyakum 1983, Tsou et al. 1987), though we recognize their potential importance for initiating development. Using the Prognostic Balance System described in Chapter II, we shall calculate the generation rate of PV by condensation in saturated, stably stratified ascent. Figure 3.17 shows the regions of PV generation and destruction so obtained (expressed in units of PVU per 12 hours) along with system relative winds. This calculation accounts for the variation of heating in all three directions as it appears in equation 1.3b. Since the structure is evolving, the system motion is different at the two levels. At 400mb we subtract out the motion of the cold tropopause anomaly (figure 3.16), while at the two lower levels, we subtract out the motion of the lower anomaly circulation center. We see that at 12Z 15 December, the relative winds in the low level generation region are easterly and exceed 30 ms^{-1}. In addition, the vertical velocities diagnosed indicate parcels ascending at nearly 15 cms^{-1}. Thus, the PV created should appear in the generation region at low levels and displaced to the west at slightly higher levels. This is consistent with the PV shown in figure 3.3 at 295K (about 700mb where the anomaly is centered) and the low level maximum of vorticity appearing in figure 3.5b. The magnitude of the calculated instantaneous Lagrangian change is also roughly consistent with the magnitude of the PV anomaly

appearing on the 295K surface.

At 400mb, we see a fairly pronounced region of PV destruction especially at 12Z the 15th. Relative winds in this region are comparatively weak, even near zero in places (of course the air is ascending, perhaps by as much as 20 cm^{-1} based on ω equation results). Hence, parcels may experience this PV destruction for several hours and lose a substantial fraction of the instantaneous values indicated in figure 3.17f (as high as -1.4 PVU/12h). The northern edge of this region is located where we see the low PV air at 315K (and the high tropopause θ). We have also used the approximate method presented in HMR of assessing the diabatic changes of PV following isentropic trajectories and find a similar picture on the 320K surface. We suggest that the wrap up of the upper PV may have involved diabatic processes, to what extent we cannot be certain. This diabatic destruction of PV may have also played a role in enhancing the downstream ridge since we observe the rapid sharpening of this feature to occur on the northeast side of the generation region. Detailed parcel trajectories are likely necessary to address these issues however.

Summary

The cyclone development studied in this chapter was quite dependent on an apparently preexisting tropopause PV anomaly of very large amplitude. The development was a transient process marked by the distinct change of the phase between the lower and

upper anomalies. Growth may be seen as a two stage process. The initial growth of the low level circulation appears consistent with the amplification of a warm perturbation at the lower boundary by the flow associated with the tropopause PV anomaly. Superposition of the newly created thermal anomaly with the upper feature culminates the development. Owing to the strong low level vorticity signature of the tropopause based PV, this superpostion of features is significant, perhaps contributing as much as half to the total development. The overall picture is akin to the non-modal growth scenario recently emphasized in the work of Farrell (1984). This case also emphasizes the importance of tropopause dynamics in the low level development and may represent the original Petterssen development scenario, couched in PV terms.

The evolution of upper PV in the mature system is also of interest. The nonlinear entanglement of the tropoause PV appears not directly related to the circulation associated with the lower PV and θ anomalies. It is interesting to note that the eastward acceleration of only the southern part of the trough implied that the relative motion of PV to the north was westward. The wrap up of the PV may have been aided by diabatic destruction of PV aloft as well. The strongly diffluent nature of the flow in the PV sink region meant that, parcels were decelerating (by definition) and perhaps spending considerable time there. Also, these parcels were exiting into the region later occupied by the arc shaped wedge of low PV (high θ_T) air seen in figure 3.17.

The overall effects of condensation for this case are still

rather uncertain. There was a modest enhancement of the upper PV signature at low levels between 00Z and 12Z the 15th which was probably diabatically produced. There was also the intensification of the downstream ridge and increase of the low level southerly flow in phase with the warm boundary anomaly. We cannot say with certainty how much of this was a product of condensation heating. Linear tendency calculations can only tell us that some diabatic enhancement of the upper level ridge occurred.

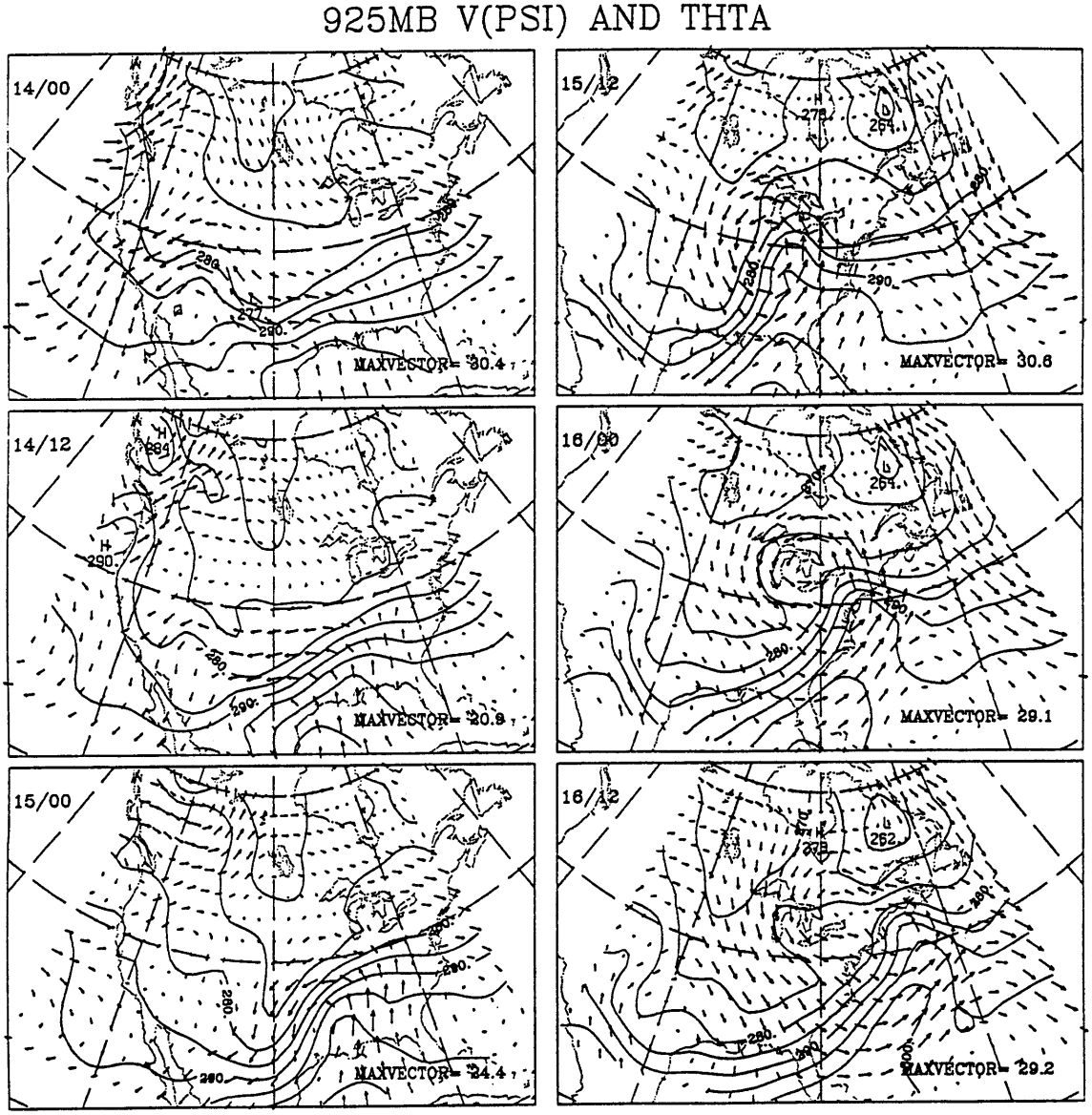
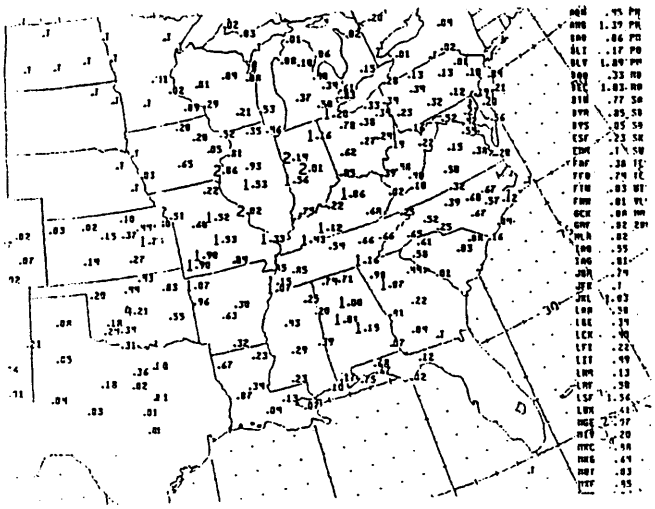


Figure 3.1 Balanced winds and lower boundary θ. Both fields represent averages over the layer from 1000mb to 850mb. The maximum vector length is noted in the bottom right corner of each plot, the time in the upper left corner. Vectors are centered on their respective gridpoint locations. Time convention is DD/HH where DD is the day of the month and HH is the hour (GMT). This convention is used in all plots unless otherwise stated. Contour interval for θ is 5K. The latitude and longitude lines intersecting near the center of the plot are 40N and 100W (left column) and 40N 80W (right column).
(a) 00Z 14; (b) 12Z 14; (c) 00Z 15; (d) 12Z 15; (e) 00Z 16; (f) 12Z 16



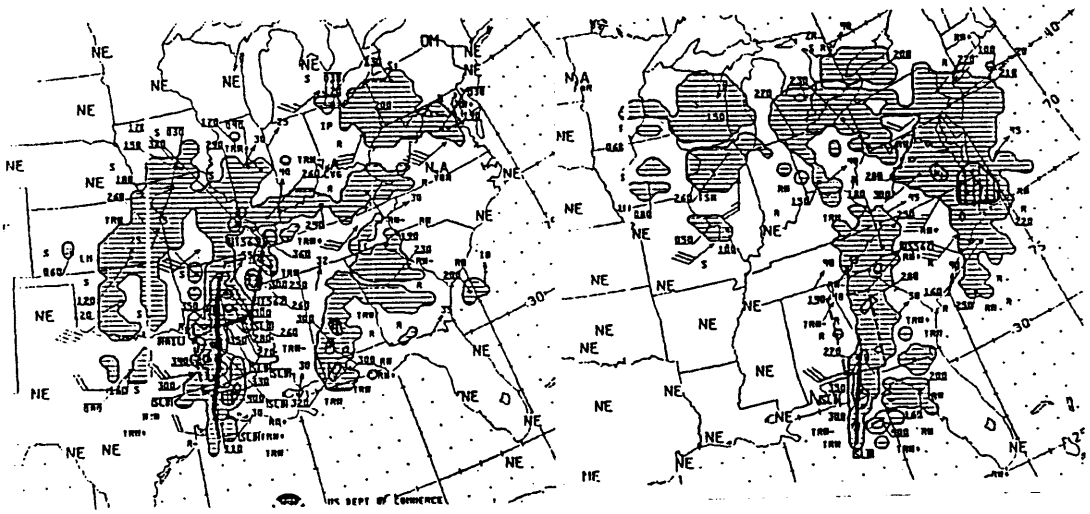


Figure 3.2 (a) 24 hour precipitation totals (inches) between 12Z 14 and 12Z 15 December; (b) Composite radar echo summary valid 0035Z 15 December. Relevant symbols. NE=no echo at radar site; S=snow; R=rain; W suffix means shower; T prefix means thunder; + and - indicate increasing and decreasing intensity. Contours indicate reflectivity levels and related rainfall rates; level 1 is < 0.2" per hour, level 2 is 0.2" to 1.65" per hour, level 3 is > 1.65" per hour. Vectors with numbers indicate movement and speed of cells, pennants denote area motion (convention as with standard wind barbs in knots). Cloud top heights indicated by underlined numbers (lines point to measurement location).

(c) as in (b) but for 1235GMT 15 December. Note that no Canadian data is available.

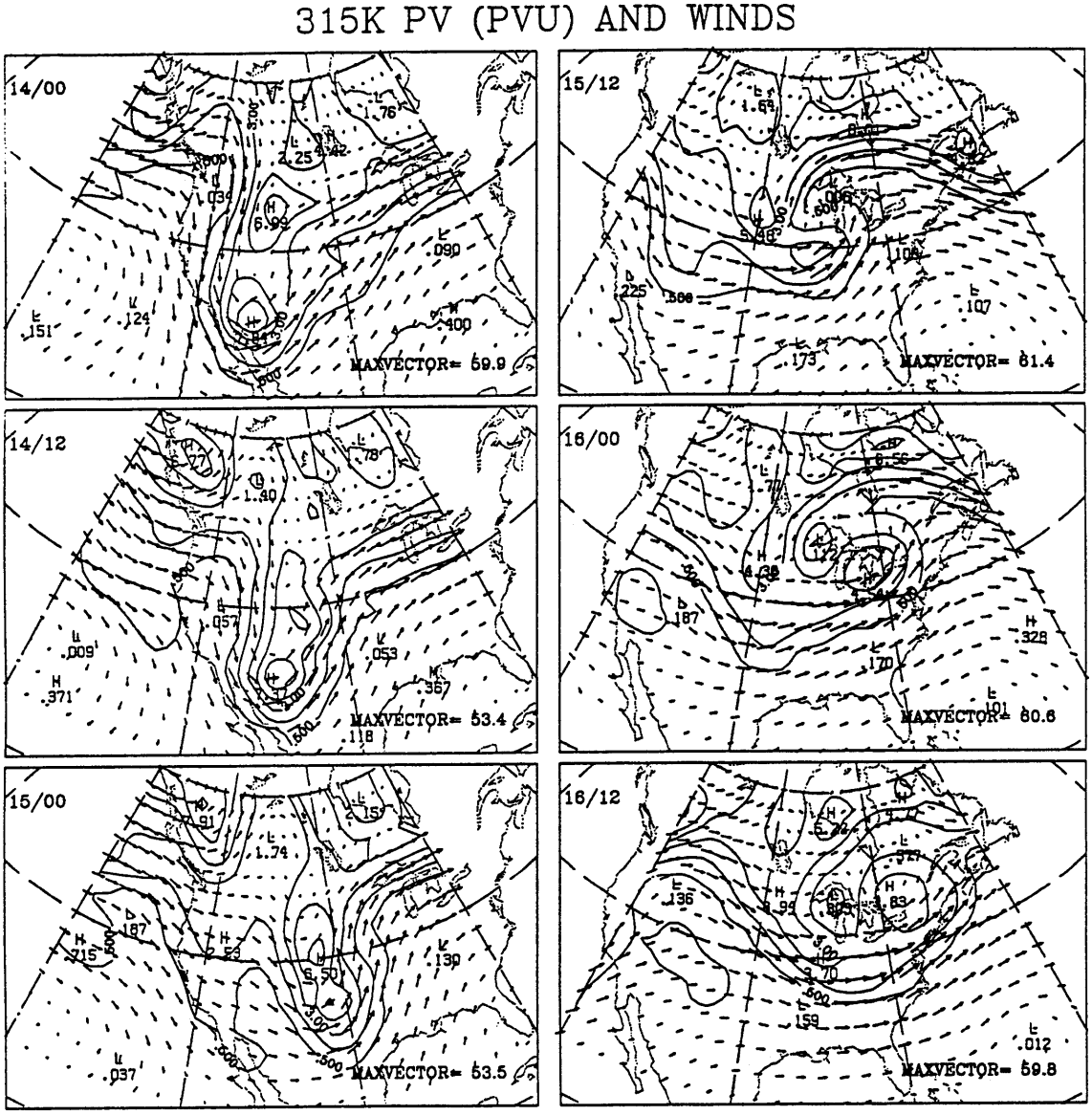


Figure 3.3 315K PV (PVU) and isntropic winds. Conventions as in figure 3.1 except the central longitudes are 110W (left) and 90W (right). The contours of PV appear at 0.5, 1.5 and every 1.5 units thereafter.

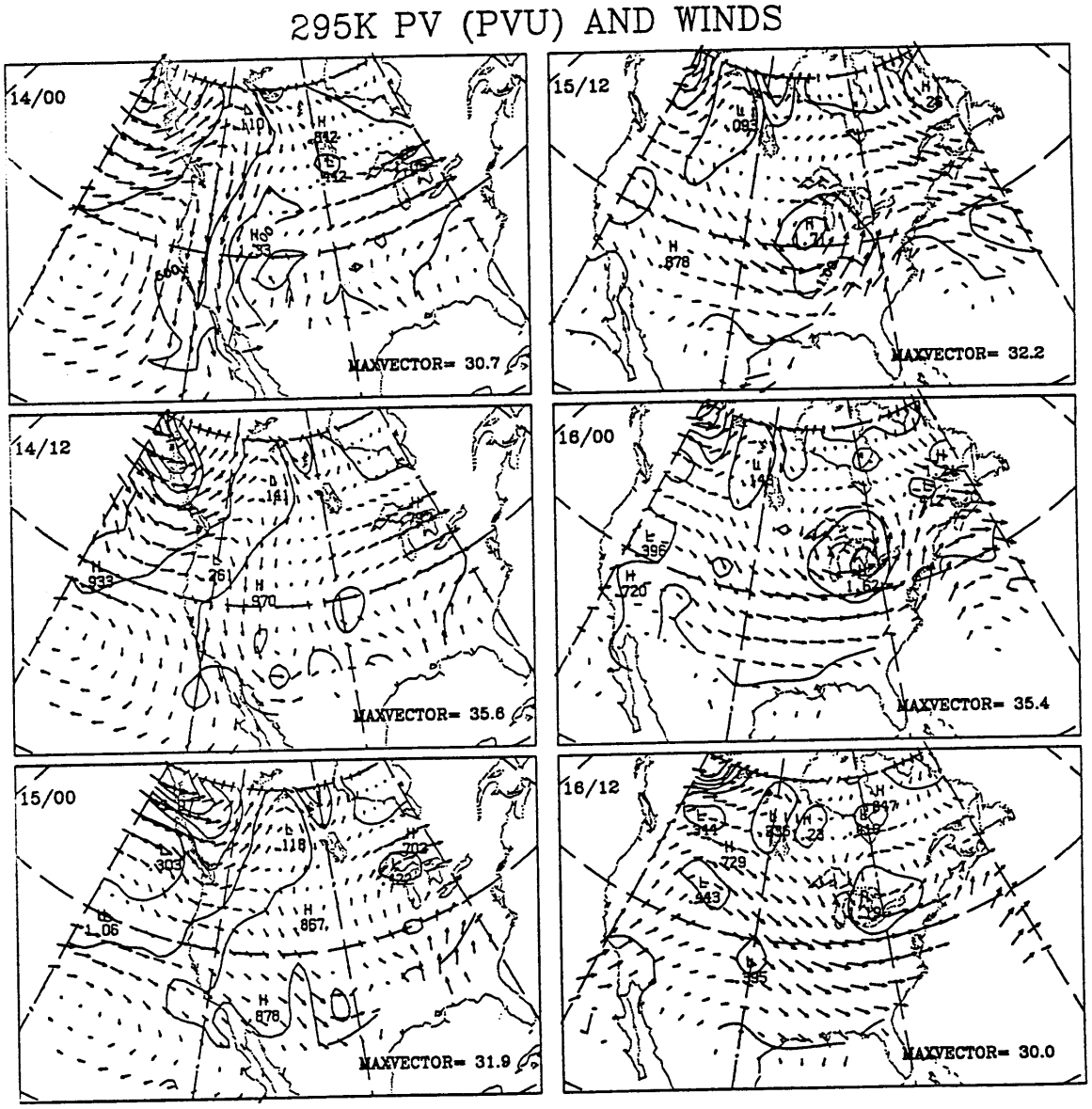


Figure 3.4 As in figure 3.2 but for the 295K surface. Wind vector lengths have been scaled up in length by a factor of 2 relative to those in figure 3.2

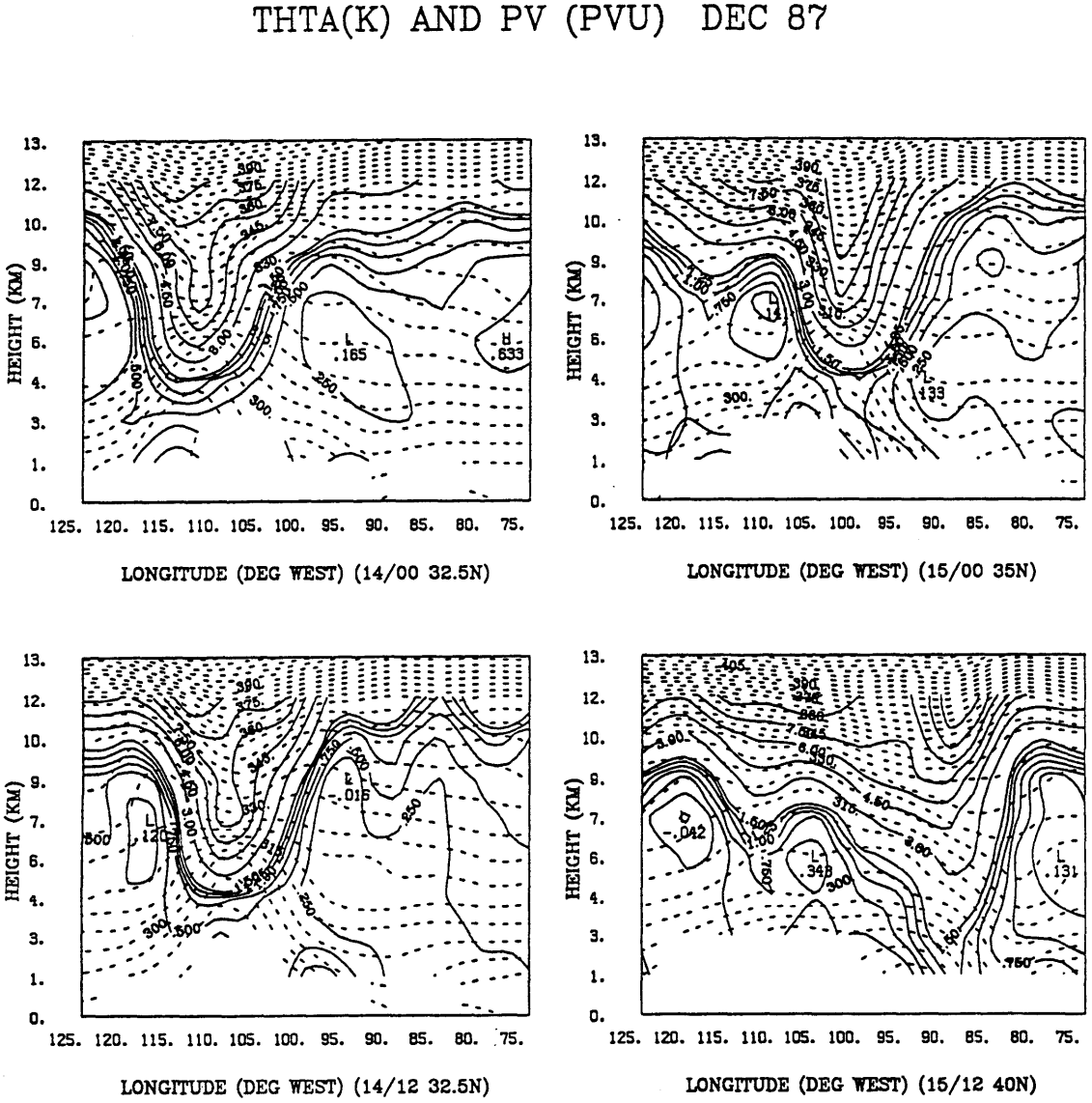


Figure 3.5 Cross sections of PV (PVU, solid) and θ (K, dashed) at constant latitude. Contours for PV are at intervals of 0.25 ($0 < q < 1.5$) and at intervals of 1.5 for higher values; θ is contoured every 5K. Values below ground not plotted; also PV at the top is not calculable. Numerical axis labels described in text; the time and latitude are shown in the abscissa character labels.
(a) 00Z 14, 32.5N; (b) 12Z 14, 32.5N; (c) 00Z 15, 35N; (d) 12Z 15, 40N

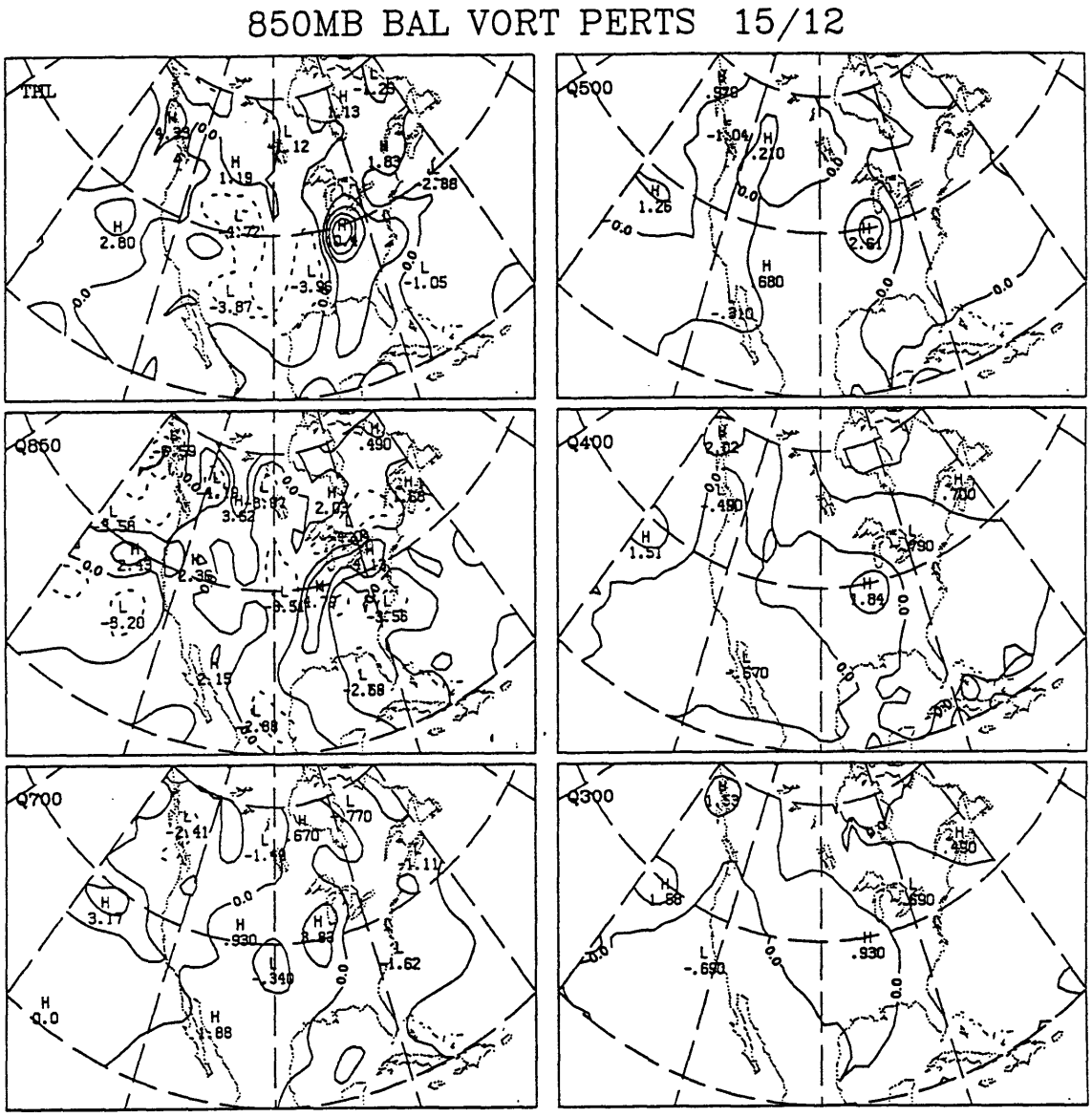


Figure 3.6 Perturbation vorticity at 850mb associated with (a) lower boundary θ (THL); (b) 850mb PV (Q850); (c) Q700; (d) Q500; (e) Q400; (f) Q300. Contour interval is 2×10^{-5} s^{-1} and the central latitude and longitude for all plots are 40N and 100W respectively. All fields were obtained from the inversion of Ertel's PV. Positive values and 0 are solid; negatives are dashed (same for all other plots unless specified).

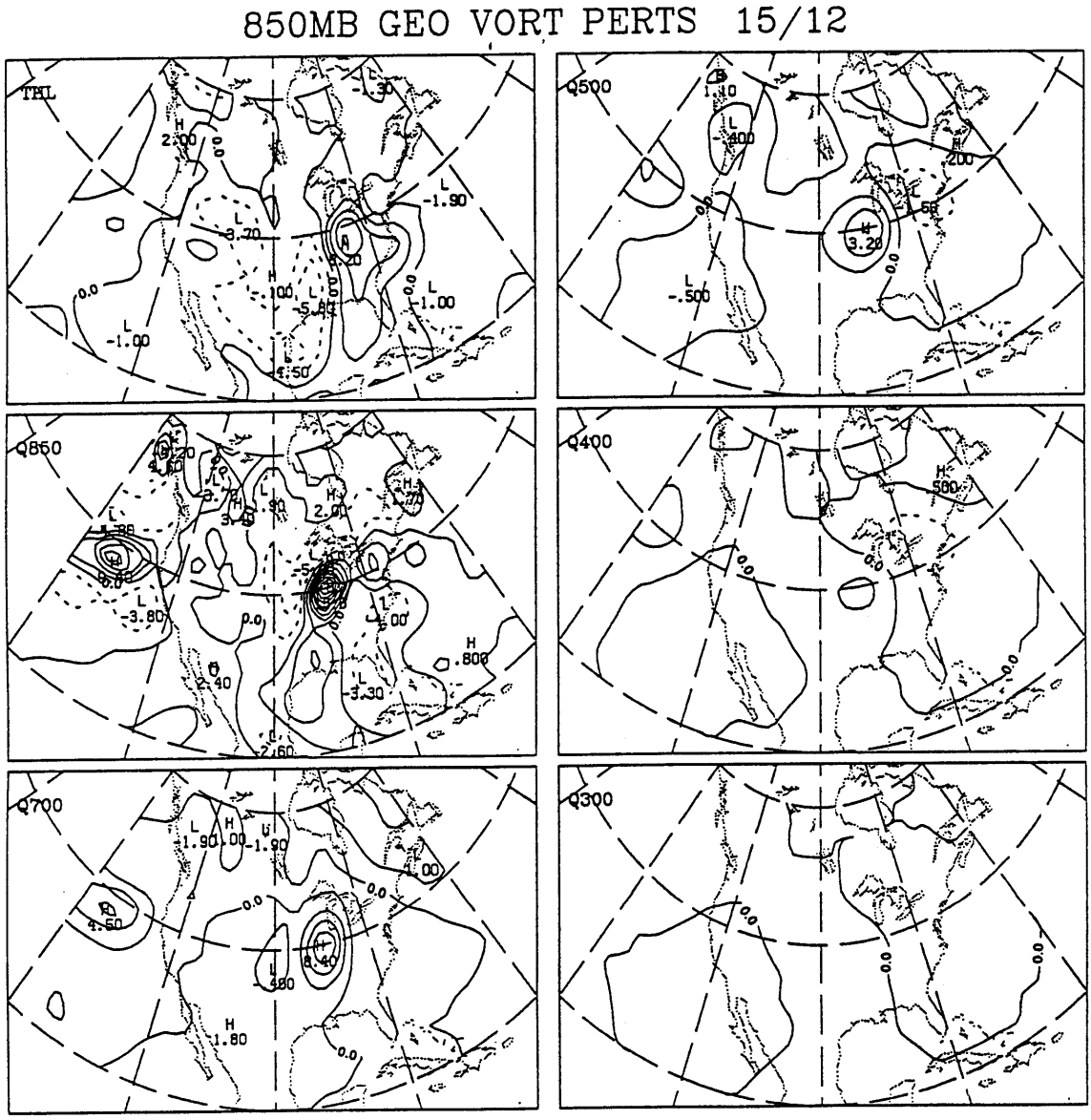


Figure 3.7 As in figure 3.6 except for quasigeostrophic pseudo PV. Plotted is the geostrophic vorticity.

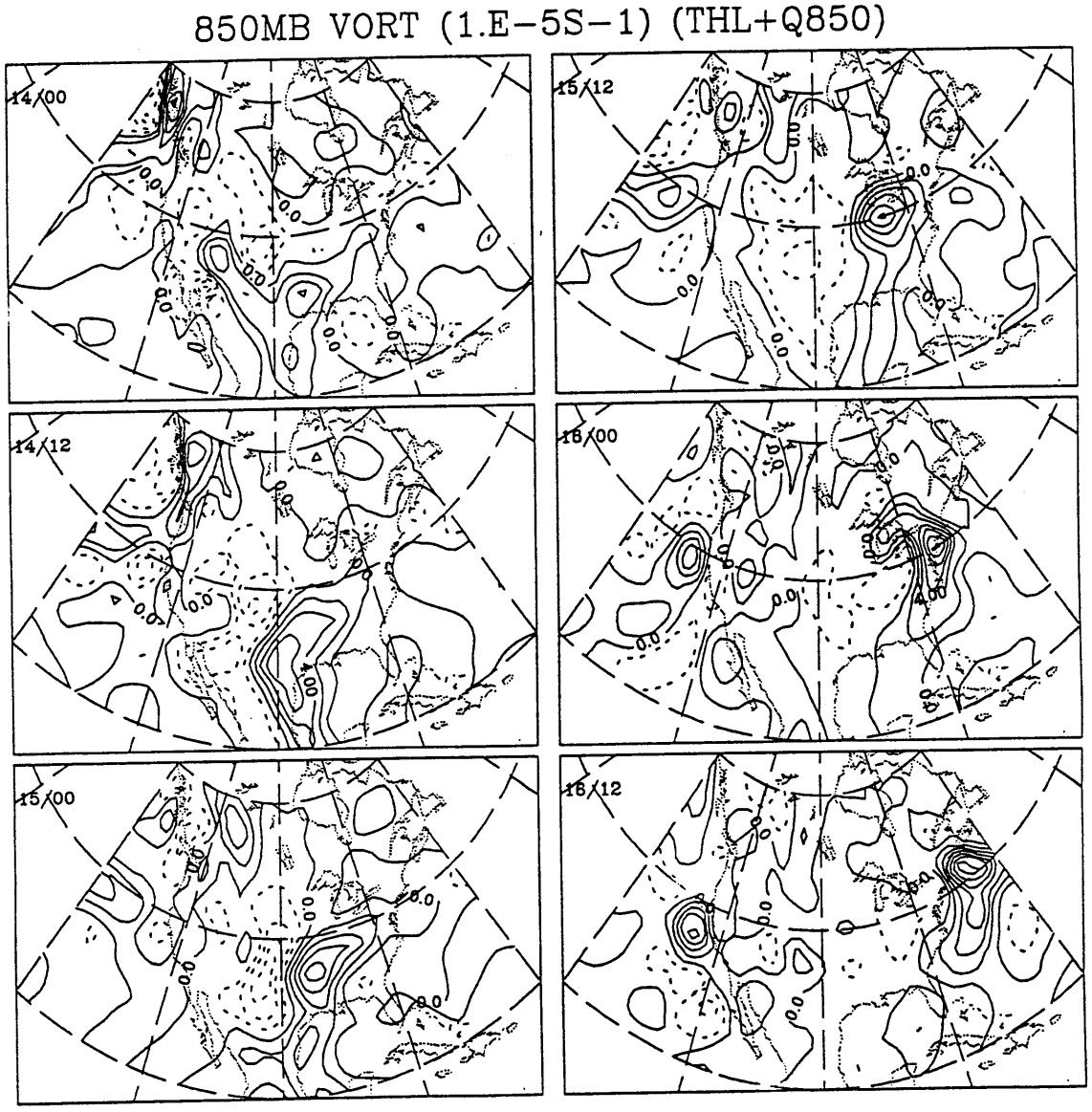


Figure 3.8 850mb perturbation vorticity associated with lower boundary θ and 850mb PV anomalies. Contour interval and map conventions as in figure 3.6 (a) 00Z 14; (b) 12Z 14; (c) 00Z 15; (d) 12Z 15; (e) 00Z 16; (f) 12Z 16

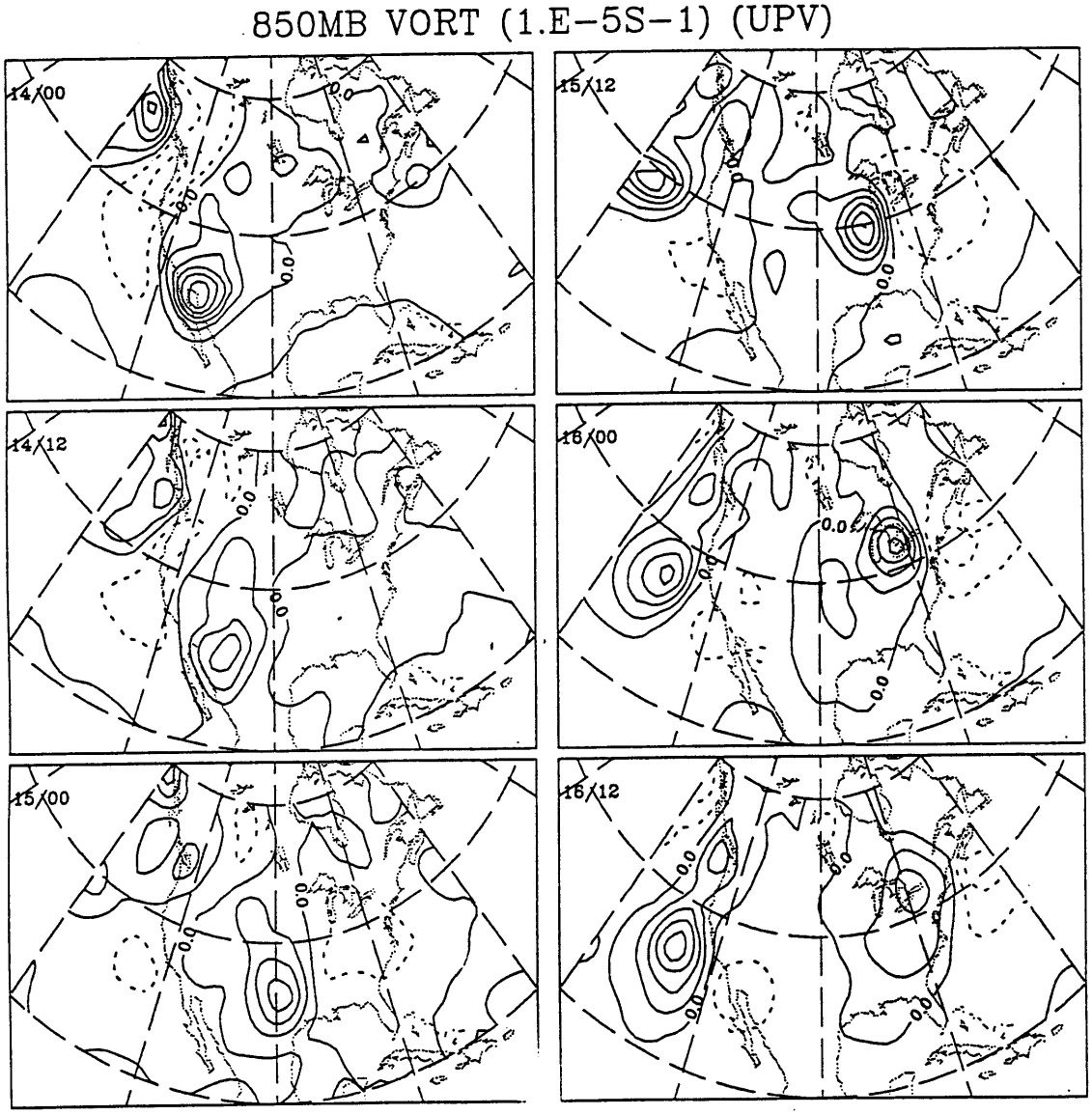


Figure 3.9 As in figure 3.8 but for the contribution from upper level PV.

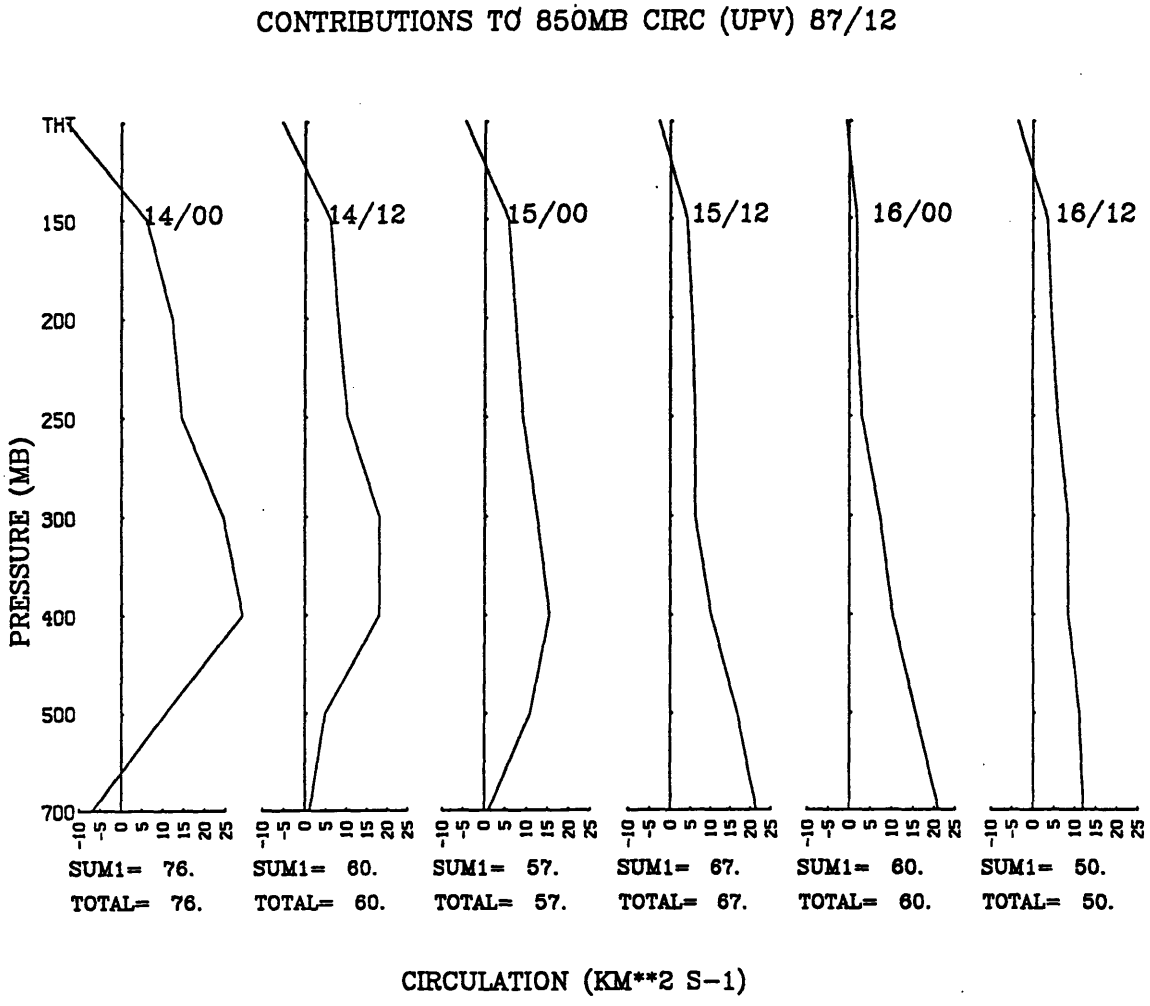


Figure 3.10 Profile of the contributions to the 850mb circulation by PV at each level at and above 700mb. The time is indicated at the upper part of each graph in the standard format. "THT" denotes the contribution from θ at the top boundary (125mb). The total circulation, calculated by a method specified in the text, is indicated at the bottom of each graph (units $km^2\ s^{-1}$).

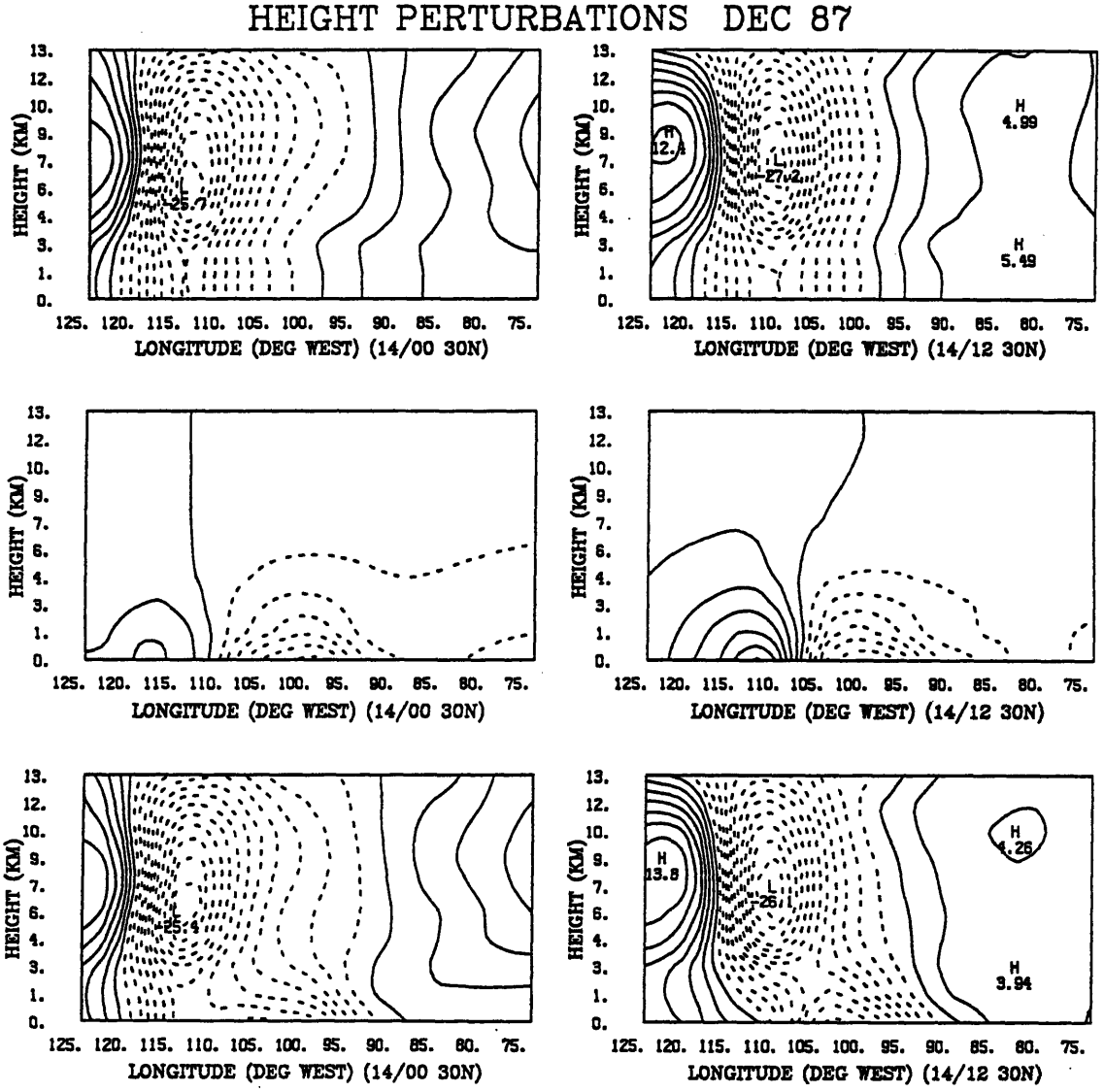


Figure 3.11 Constant latitude cross sections of geopotential height perturbations. The graph labelling convention is that of figure 3.5. Left column: 00Z 14 December; right column: 12Z 14 December. In each column, the top figure is the contribution from the upper PV, the middle is from the lower anomaly and the bottom is the sum (total perturbation). Contour interval is 2 dm.

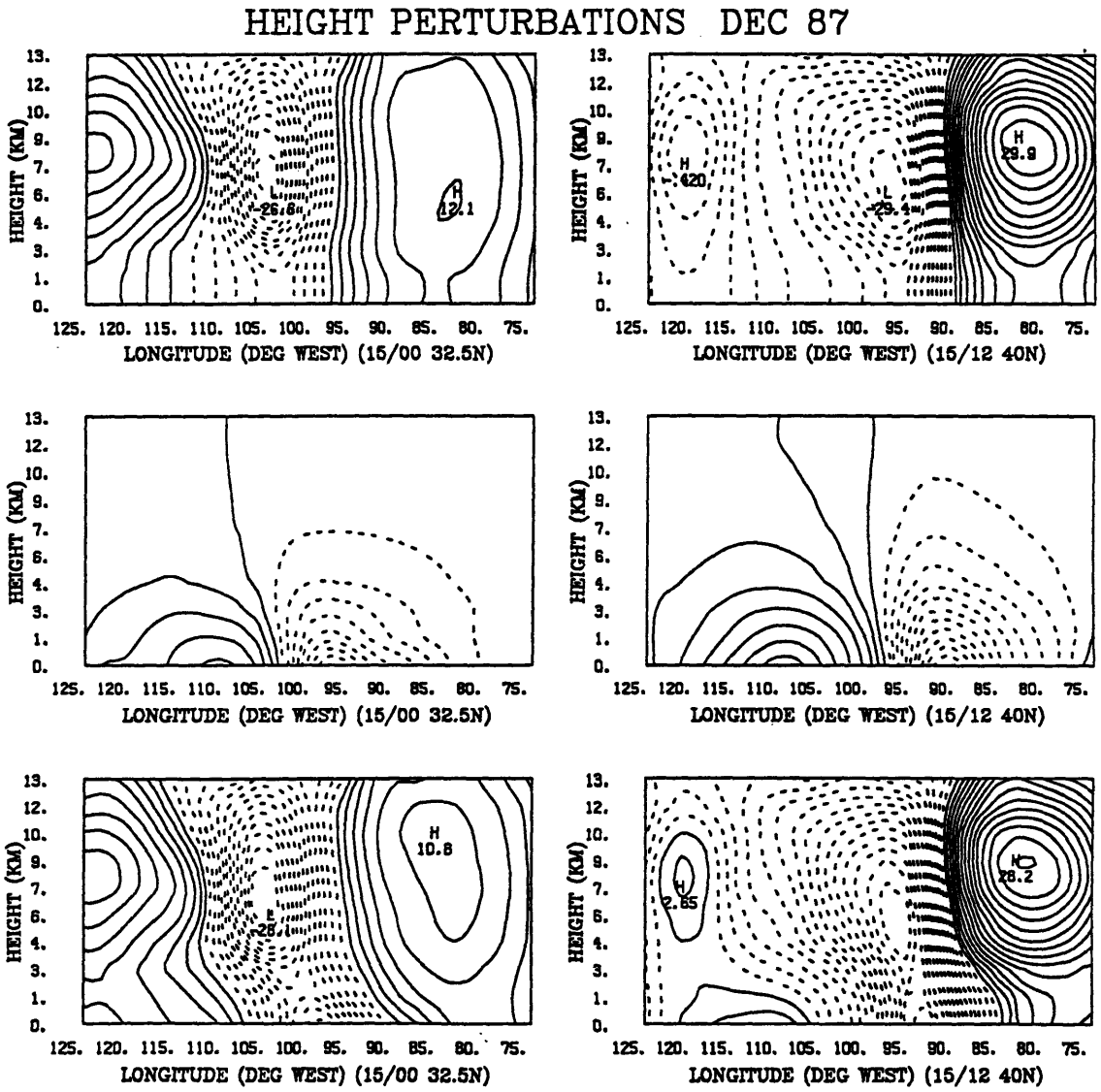


Figure 3.12 Same as in figure 3.11 except left column is for 00Z the 15th and right column for 12Z the 15th.

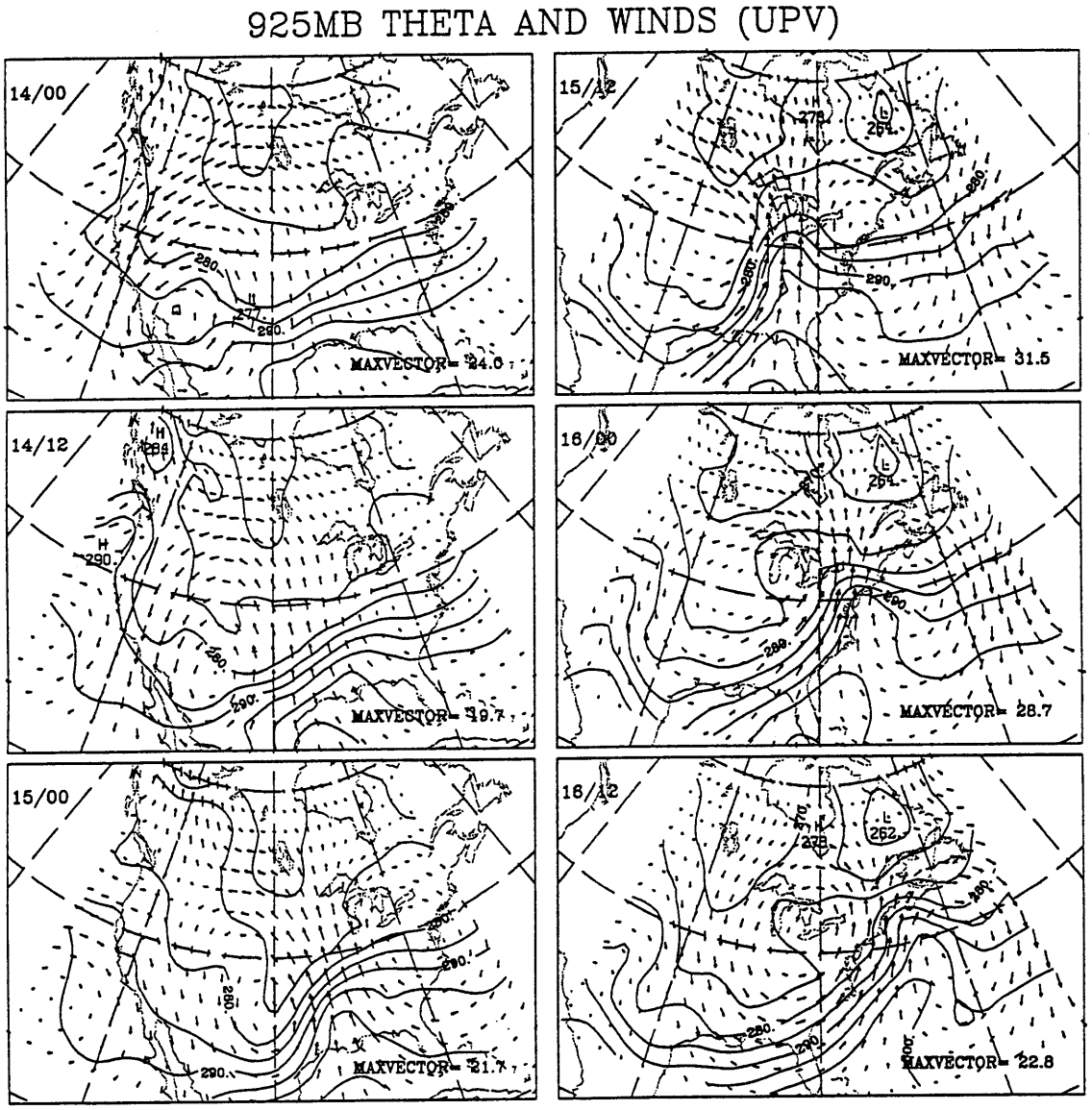


Figure 3.13 As in figure 3.1, except the winds are from the upper level PV perturbation.

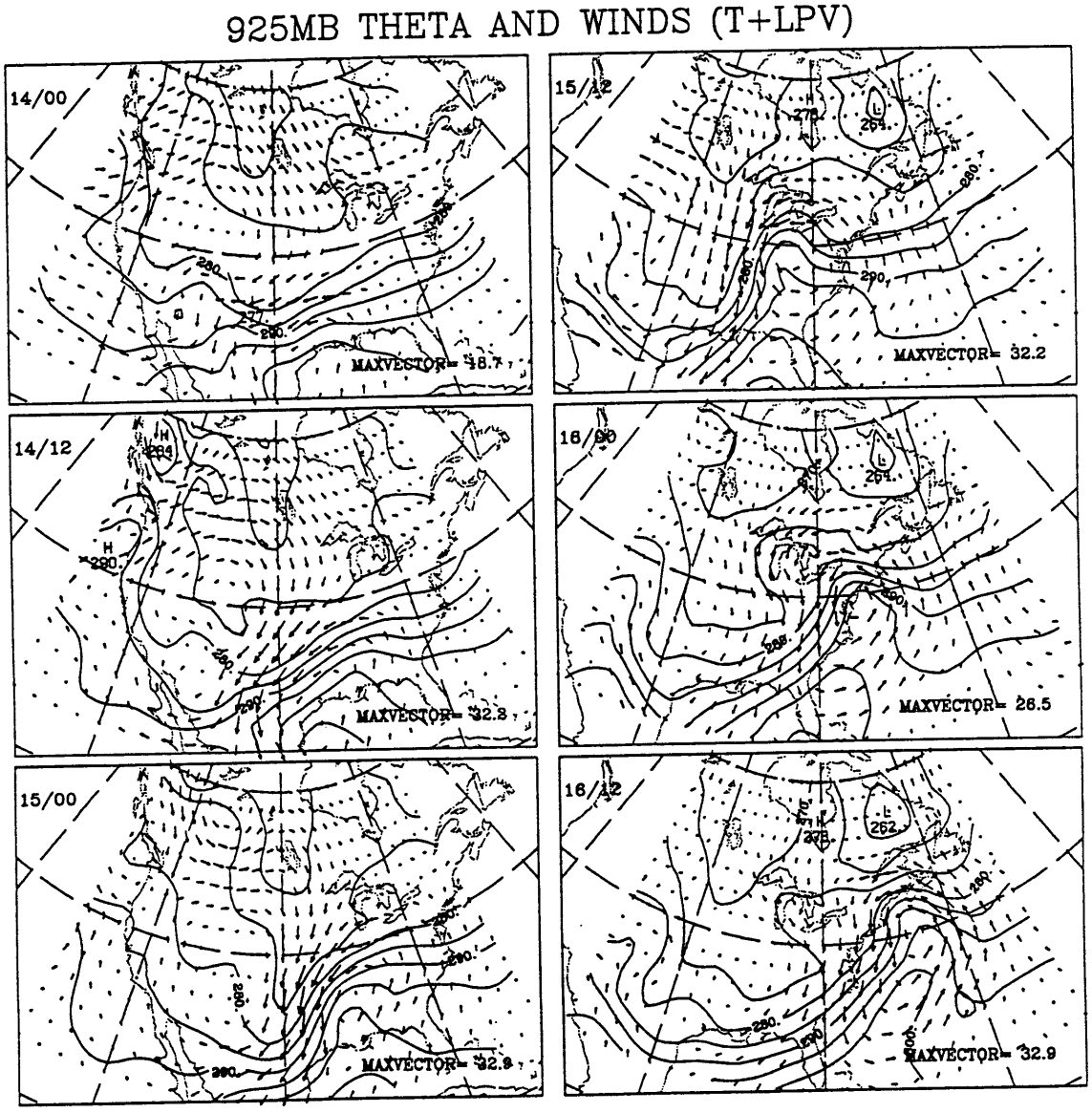


Figure 3.14 As in figure 3.1, except the winds are for the lower anomaly.

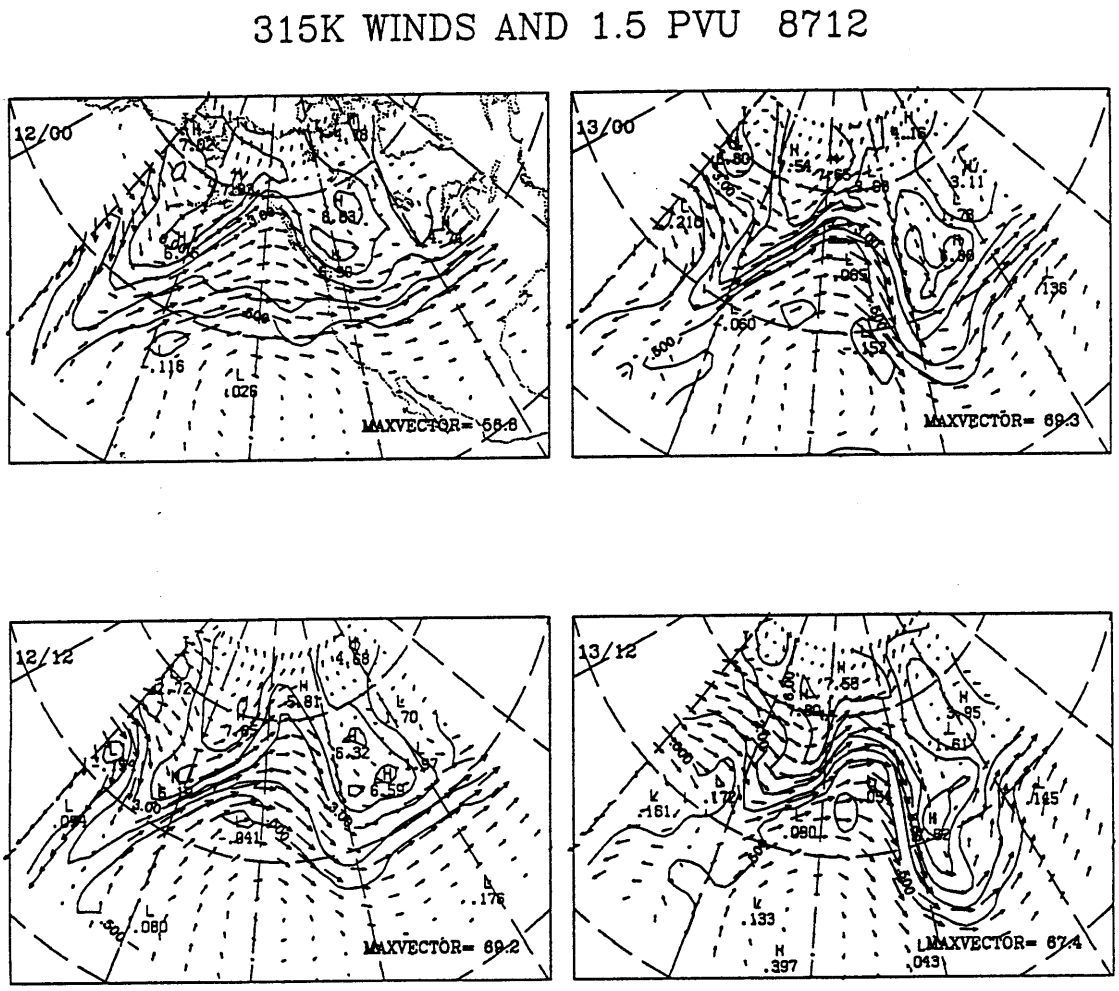


Figure 3.15 315K PV (PVU) and winds. PV contoured as in figure 3.3. (a) 00Z 12; (b) 12Z 12; (c) 00Z 13; (d) 12Z 13. The leftmost longitude line on which data in plotted in 180W in each, the easternmost is 90W (see map at upper left). The longitude line nearest the center is 40N.

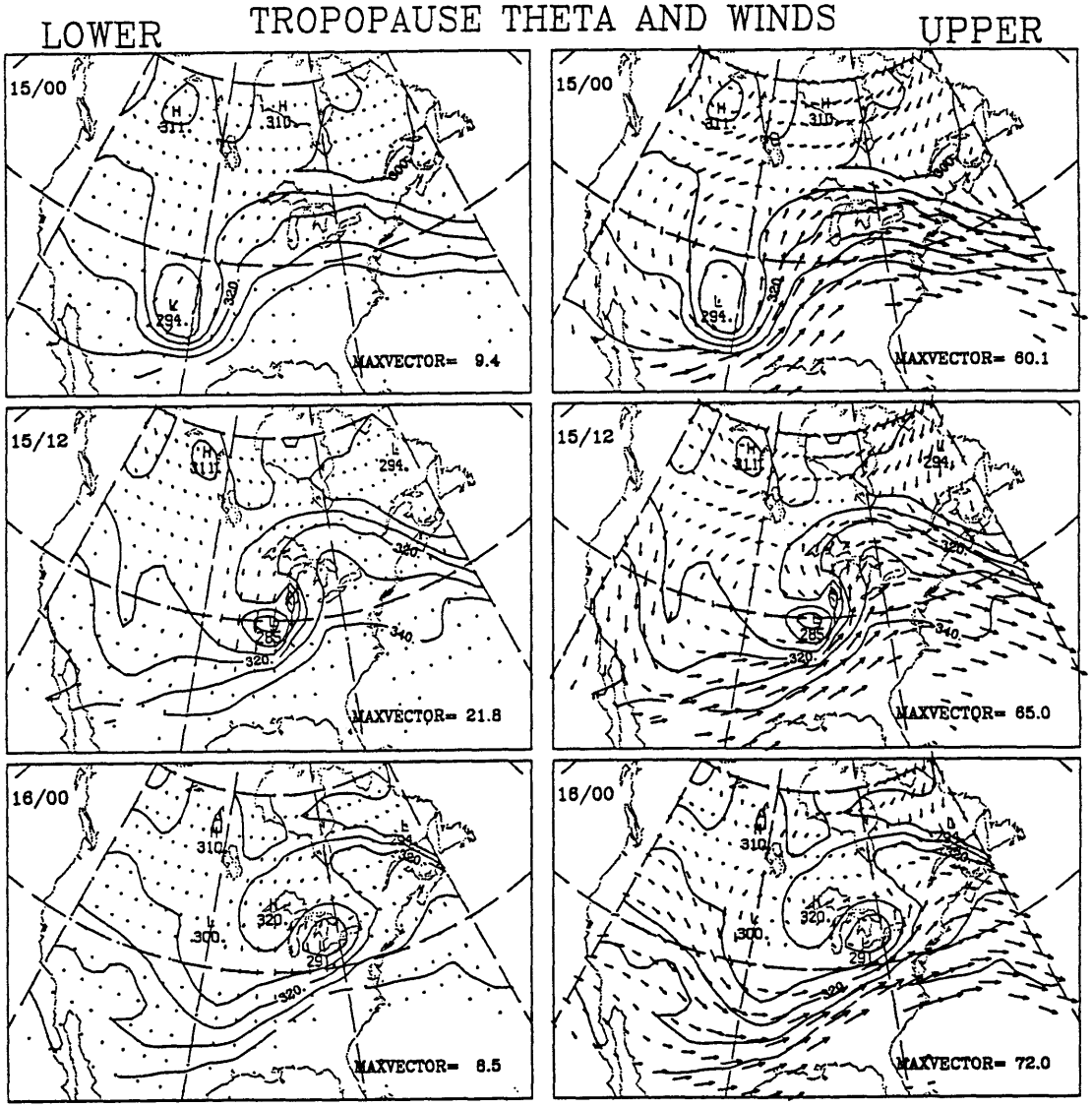


Figure 3.16 Tropopause (q=1.5 PVU) potential temperature (K) and winds. Left column shows winds from the lower anomaly interpolated to the tropopause; right column shows the remainder of the interpolated balanced winds. (a) 00Z 15, LOWER; (b) 12Z 15, LOWER; (c) 00Z 16, LOWER; (d) 00Z 15, UPPER; (e) 12Z 15, UPPER; (f) 00Z 16, UPPER. Wind vector lengths for lower perturbations have been scaled up by a factor of 3. Only the winds in the right column have had the system speed removed. These velocities were ($16ms^{-1}$,$7ms^{-1}$) at 00Z 15; ($17ms^{-1}$,$9ms^{-1}$) at 12Z 15 and ($11ms^{-1}$,$6ms^{-1}$) for 00Z the 16th. These represent the average motion of the cold anomaly over a 24 hour period centered on the indicated time.

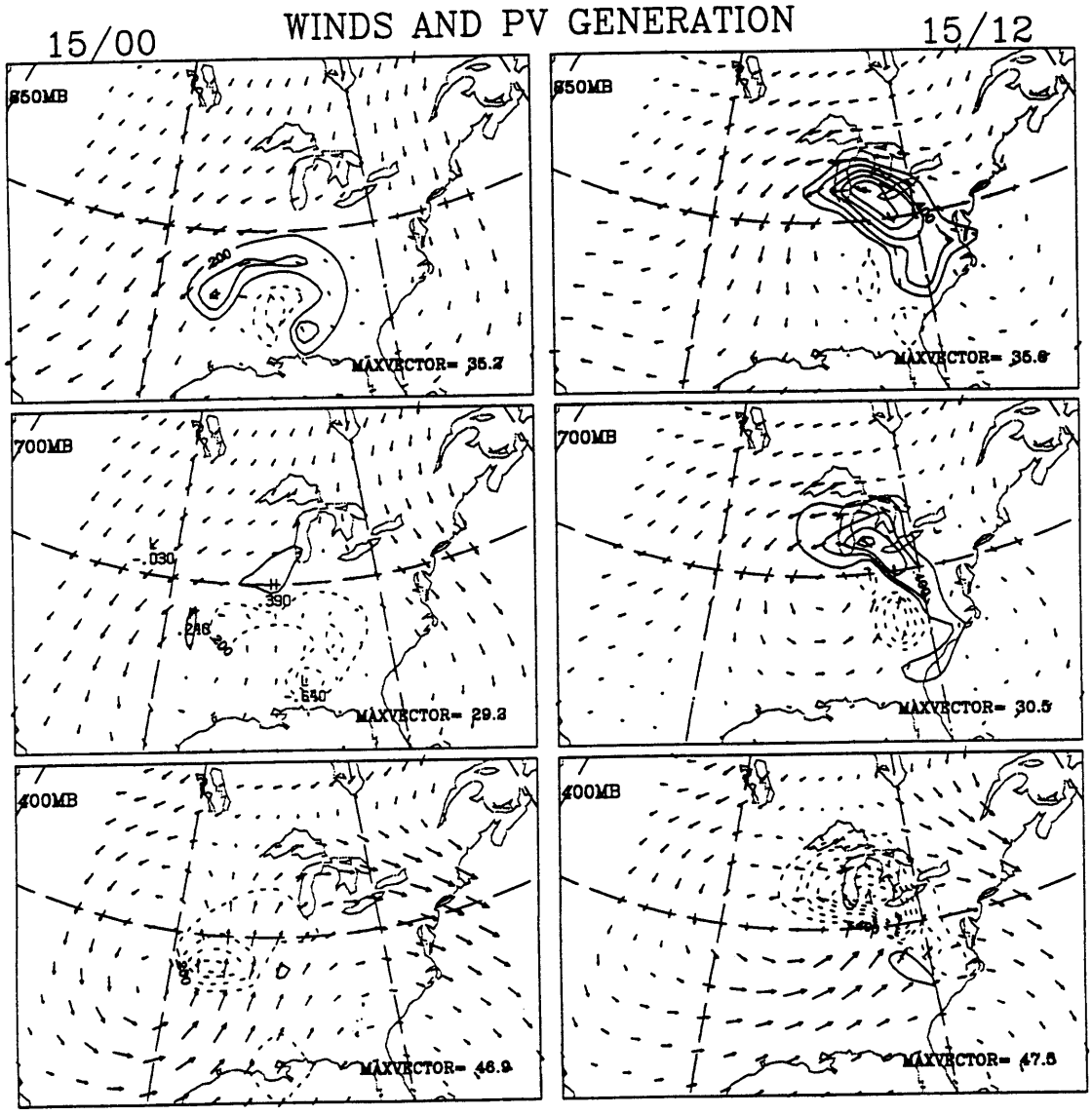


Figure 3.17 PV generation (PVU per 12 hours) and system relative isobaric winds. The contour interval is 0.2 and the zero contour has been omitted. (a) 00Z 15, 850mb; (b) 00Z 15, 700mb; (c) 00Z 15, 400mb; (d) 12Z 15, 850mb (maximum value=1.3); (e) 12Z 15, 700mb; (f) 12Z 15, 400mb (minumum value= -1.5). The relative winds used at 400mb were those in figure 3.17. The relative winds (u,v) for the 850mb and 700mb levels used were ($12ms^{-1}$,$12ms^{-1}$) at 00Z the 15th and ($15ms^{-1}$,$8ms^{-1}$) for 12Z the 15th. These latter vectors indicate the motion of the lower anomaly circulation center (figure 3.14). No scaling of the wind vectors has been used.

Chapter 4: Additional Cases

In this part of the thesis we examine more cases to obtain some perspective of the general character of cyclogenesis in terms of potential vorticity. Three additional cases are considered which will be compared with case I and with each other. Although this sample size is rather small for generalizations to be made, we do find recurring themes among the cases. First is the identification of the primary circulation of the cyclone with the distribution of potential temperature at the lower boundary. Second is the dominance of the tropopause PV perturbations in the process of amplifying the lower boundary thermal anomalies. Third is the generation of low level PV, likely from condensation, nearly in phase with the warm boundary thermal perturbation. The circulation associated with this low level feature makes a significant contribution to the wind and vorticity fields in two of these cyclones. We note that the low level PV is mostly generated in regions of stratiform precipitation and that there appears to be little systematic relation of convection to the formation of these features.

Case II. November, 1988

Beginning at 00Z 09 November, when a low level circulation was first established east of the Rocky Mountains near 40N, we

observe a cyclone that intensifies and moves northeastward toward the Great Lakes (figure 4.1). The circulation center passes near 42N 85W at 12Z on the 10th, then continues along the St. Lawrence River, reaching the Gulf of St. Lawrence shortly after 12Z the 11th. The final amplitude is a bit weaker and overall development slower than in case I. We chose to examine this case because of the relative smallness of features at the initial time of development and because of the marked regularity in the progression of synoptic disturbances during this period. The averaging period used to determine the mean PV was again 5 days, from 00Z 08 to 12Z 12 November.

Unlike case I, no strong low level front is apparent in the θ field displayed in figure 4.2, rather, we see a broad baroclinic zone with horizontal gradients of θ being 10-15K per 1000km. The wind pattern at low levels indicates a meridionally elongated trough near 100W at 00Z and 12Z on the 9th. The structure is quite asymmetric, favoring stronger winds on the east side. The primary organization and amplification of the low level wind and θ fields occurs between 00Z and 12Z on the 10th. The mean translational speed of the surface system averages nearly $15ms^{-1}$, ranging from about $8ms^{-1}$ toward the east on the 9th up to $20ms^{-1}$ in the mature phase on the 11th.

As in case I, there was an upper level PV perturbation, visible in figure 4.2 as an undulation in the tropopause. The structure is similar to that of case I, though the anomalies are much weaker in this example. The main difference is that the whole pattern

undergoes amplification during the time of low level development. Also of interest is the 850mb positive PV perturbation appearing at 12Z the 9th between 90W and 95W. As can be seen from the lowered isentropes in its vicinity, this feature is in phase with relatively warm temperatures near the lower boundary. After this time, the upper trough progresses somewhat relative to the lower PV, such that there is a sloping region of high PV extending from low levels to the tropopause by 12Z 10 November between 80W and 85W. This coincides with a strong, tropospheric deep baroclinic zone, as indicated by the dashed isentropes.

We now break up the PV field into its significant components and calculate their respective contributions to the cyclone circulation. The analyses we have examined indicate a greater importance of growing PV anomalies in the lower troposphere than in the previous case. The cross section indicates the weakest perturbations are near 700mb, but these are more in phase with PV at 850mb than the PV aloft. Hence, in this case, we define three anomalies, upper PV (500mb and higher, denoted q_U), lower PV (850mb and 700mb, denoted q_L) and θ_B.

Figure 4.3 presents the contribution to the 850mb vorticity from the q_L and θ perturbations together (left) as well as from the q_U distribution (right column). It is apparent that the vorticity signature of the upper PV is never an appreciable part of the total and does not superpose on the vorticity associated with the lower anomalies. Superposition, which was important in case I, is absent

here. In figure 4.4, we show the separate vorticities from the q_L and θ anomalies for the last three times in 4.3, 00Z the 10th to 00Z the 11th. The left column reveals a rather disorganized signature from the lower potential temperature anomalies initially. Note that there is positive vorticity from the q_L distribution nearly in phase with the positive vorticity from the thermal perturbations at this time and at 12Z the 10th. It is interesting that these anomalies are systematically in phase near the warm frontal region of the cyclone, but tend to cancel elsewhere.

For another perspective on the development we show height-longitude cross sections of the evolution of the geopotential perturbations in figure 4.5. For simplicity, we have grouped the lower boundary θ with the lower PV since the significant features of each are basically in phase. For brevity, we only plot the fields at 00GMT beginning on 09 November and ending on the 11th. There are several important points to be made here. First, growth occurs simultaneously at upper and lower levels. There is no time lag as in case I where growth at upper levels preceeded low level development. The growth at low levels does not appear to lead the upper level development either, as it does in the life cycle experiments of Simmons and Hoskins (1978). Second, the upper perturbation has a maximum amplitude around the tropopause and is, to some extent, a weaker version of the case I upper feature with a more wavelike appearance. Note, however, there is substantial growth of the whole wave with time, not just the anticyclonic portion of it. Third, the phase difference between

the upper and lower disturbances decreases from a bit less than 180° to roughly 90° in the first 24 hours, then remains nearly fixed. The structure of the perturbation at 00Z the 9th and its location just east of the Rocky Mountains is strongly suggestive of a lee cyclogenesis. It is possible that this initial development of a lee side warm boundary perturbation made the troposphere structural evolution over the first 24 hours appear more transient than it would have been in the absense of such an event. For example, if one concentrates on the phase relation between the cold lower anomaly (initially barely visible near 125W) and the upper PV, the structure changes little. Thus, in contrast to case I, much of this cyclogenesis occurs with a nearly constant phase shift between the upper and lower level perturbations.

At this point, we examine the origin of the prominent features involved in this development. In figure 4.6, we present the low level flow associated with the upper PV anomaly pattern overlayed on lower boundary potential temperature. It is apparent that the meridional flow is in phase with the thermal wave and acting to amplify it. One can also see a tightening of the isotherms by 00Z the 10th near 40N 95W. This frontogenesis is a product of the circulation from the lower tropospheric PV and θ_B anomalies (figure 4.7). The same winds in figure 4.7 are also acting to propagate the thermal wave eastward along the baroclinic zone, most noticably after 00Z the 10th.

We can take advantage of the near periodicity of this

development and quantify the relative importance of each of the anomalies in amplifying the boundary thermal wave. In figure 4.8, we show the correlation of meridional wind with perturbation θ_B averaged over a wavelength. The short dashed line corresponds to the heat flux from the upper PV whereas the long dashed and solid lines refer to the heat flux from the lower PV and boundary θ anomalies respectively. We note that for this calculation, the perturbations reflect departures from both the time and zonal means, although in practice the same results are obtained using just perturbations from the time mean. The averaging is done over 40^0 of longitude at each time; 120W to 80W at 12Z the 9th; 110W to 70W at 00Z the 10th and 100W to 60W at 12Z the 10th.

At first, there are contributions from both the lower and upper PV. The influence of the q_L perturbations can be traced to a juxtaposed positive - negative anomaly couplet centered near 40N, 95W at 12Z the 9th. This couplet is also evident near the Great Lakes at 00Z the 10th (figure 4.4d). However, by far the largest contribution on average comes from the upper PV especially at 12Z on the 10th. The upper PV anomalies also contribute most to the meridional derivative of the heat flux, which is equal to the local tendency of the zonally averaged potential temperature. Thus, it appears that the same mechanism is operating here to amplify the thermal wave as in case I, but the lower PV perturbations may have been influential in the early stages of growth as well.

As already pointed out, the upper wave is intensifying during

the low level development. We examine the possible role of the lower PV and θ_B perturbations in this process by plotting their associated winds on a tropopause map (introduced in Chapter 3) in figure 4.9. Although wind velocities never exceed $6ms^{-1}$, they are properly phased as to imply amplification of the wave. The large gradient of potential temperature (note the 5K contour interval) may allow this weak flow to have an important role in the tropopause evolution. Clearly, however, the remainder of the flow (not shown) is responsible for the rapid frontogenesis that occurs on the upshear side of the trough by 00Z the 10th.

In addition, we calculate the heat flux at the tropopause associated with both the upper and lower level anomalies. The details of the calculation are the same as that for the flux of lower boundary potential temperature, except for a 10^0 westward shift in the averaging region at each time. From figure 4.10, it is apparent that the flux associated with the upper PV dominates on average except between 40N and 45N. This latitude band corresponds to the region in figure 4.9 where the flow from the lower PV and θ anomalies is advecting "cold" air southward. The large fluxes between 45 and 50N associated with the upper PV seem to correspond to amplification of the ridge downstream.

Attention must also be given to the low level PV perturbations that develop and contribute substantially to the cyclone circulation. The chief part of the low level q field is the positive anomaly seen in figure 4.4, since that undergoes significant intensification. The proximity of this feature to a region of

precipitation as well as being a localized maximum on a θ surface (not shown) suggests a diabatic origin. Further support for this comes from figure 4.11 on which we plot 850 mb PV (dashed) and PV generation obtained from two sources. The solid contours (and corresponding values printed at grid points) were obtained from the PBE's, as we did in Chapter 3. The letters each refer to a station whose precipitation reports were used to estimate PV generation in a technique described as follows.

To estimate the PV generation at a given time t_o, we first selected stations reporting falling precipitation. We then computed the average rate of precipitation by dividing the 6 hour total precipitation centered on t_o by the interval over which the precipitation fell. If precipitation fell for less than 6 hours, the duration could still be assessed because the times for beginning and end are noted in hourly reports. Since 3 hourly precipitation totals were not available for Canadian stations, we used surface synoptic reports which indicate 6 hourly totals. Rather than average over two six hour periods for these stations, we chose to use only the report valid at t_o. Thus estimates from synoptic (Canadian) stations were most representative of conditions somewhat before t_o. If synoptic reports were unavailable, we used the 24 hour NMC precipitation summaries (as in fig. 3.2), provided that some estimate of the precipitation onset and cessation time was available. Next, we assumed the column above the station was saturated and stably stratified. Then we required the mass

weighted vertically integrated condensation rate (the change of specific humidity with time) to be consistent with the precipitation rate. This means that we are neglecting the effects of evaporation. The condensation rate is directly proportional to the diabatic heating rate which allows us to relate the integrated diabatic heating to the precipitation rate as

$$L_v P = \int_{\pi_s}^{0} d\pi \left(\frac{p_0}{Rg}\omega * \theta\gamma\left(\frac{\pi}{C_p}\right)^{2.5}\right) \qquad (4.1)$$

where $\omega^* = D\pi/Dt$, $p_0 = 10^5$PA and R=287 J kg $K^{-1}$and

$$\gamma = \frac{\left(1 - \frac{C_p R_v T}{L_v R_d}\right)}{\left(1 + \frac{C_p R_v T^2}{q_s L_v^2}\right)}$$

is between 0 and 1, but does not exceed 0.5 in practice. Note that $\theta\gamma/\pi$ is the lapse rate of potential temperature on a moist adiabat.

The profile of ω was assumed piecewise linear, with the level of the maximum determined from the ω equation solution. Given the precipitation rate, the observed values of θ and γ and the level of maximum vertical velocity in a piecewise linear profile, we could calculate a consistent heating distribution. From this, we estimated the generation of PV using the observed absolute vorticity and the vertical variation of the heating. Horizontal gradients of heating, included in the tendency calculations, were ignored here. The generation rate of PV was not sensitive to the imposed level of maximum vertical velocity. More important was

the sharp reduction of γ with height, as implied by the exponential dependence of water vapor with temperature at saturation.

From figure 4.11, we see that the two methods of estimating generation agree reasonably well. The resolution of our grid data is apparently insufficient to define the gap in precipitation between location B and the others on the 10th at 00Z over the Great Lakes. At both times there was deep convection occurring a few hundred kilometers to the southwest of the stratiform precipitation region. We tried to avoid the inclusion of stations reporting deep convection since the validity of our heating estimates would be suspect in these regions. Station SBN, however did report occasional lightning shortly after 00Z the 10th, but in the presence of only light precipitation. The rates shown in figure 4.11 are more than sufficient to account for the observed PV increase (maximum of 0.9PVU at 00Z to 1.2 PVU at 12Z). The location of the generation just downshear from the low level anomaly is consistent with the simulations of Emanuel et al. (1987) and Montgomery (1990) for moist two dimensional baroclinic waves. The location is also what one would expect given that the maximum generation of PV is occurring below the steering level (near 700mb) of the wave. At 00Z the 11th, the low level PV anomaly is located to the northeast of its position at 12Z the 10th, an anticipated result from figure 4.11b. In view of this analysis, we favor diabatic generation in stable precipitation as the principle source of the low level positive PV anomaly observed.

To summarize case II, we find a development characterized by

the simultaneous amplification of a tropopause based PV anomaly along with a potential temperature wave at the lower boundary. In addition, there is a development of a positive potential vorticity feature near 850 mb that moves in phase with the positive θ_B anomaly. Our analysis indicates this feature to be the result of condensation in stably stratified ascent. The upper PV again seems to play a key role in amplifying the lower boundary potential temperature wave. In turn, the tropopause perturbation is influenced somewhat by the circulation from the lower anomalies, but other processes are likely going on to amplify the upper wave.

In many ways, the structure reminds one of an Eady type development, provided we identify the upper boundary as a flexible tropopause (a surface of constant PV) and view the evolution of potential temperature on that surface as the Eady upper boundary condition. We do not wish to imply that the Eady *model* provides an accurate description of the events observed. Rather, we are referring to a conceptual picture of development which emphasizes a dominance of potential temperature perturbations at the tropopause and at the lower boundary. The interior PV anomalies that do grow appear to result from the effects of condensation rather than advection. The picture of the development of moist Eady waves presented by Emanuel et al. (1987) and Montgomery and Farrell (1990) may be a useful way to summarize this cyclogenesis. The complete details of the amplification of the tropopause potential temperature perturbation remain somewhat unclear however.

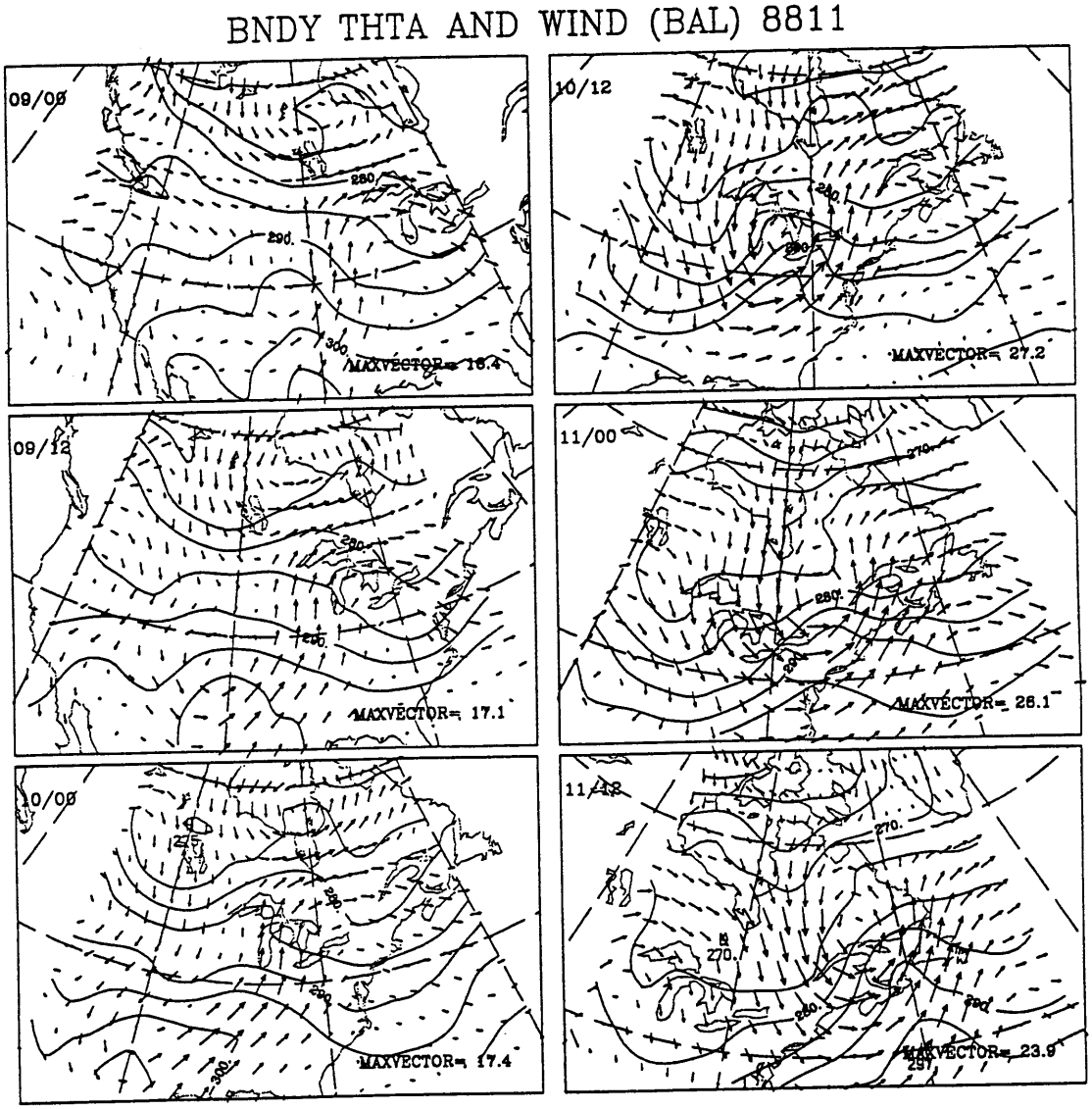


Figure 4.1 Low level balanced flow and lower boundary potential temperature (conventions as in figure 3.1). (a) 00Z 09; (b) 12Z 09; (c) 00Z 10; (d) 12Z 10; (e) 00Z 11 and (f) 12Z 11. In (a) and (b) central longitude is 100W, central latitude line is 40N. In (c) and (d), 90W and 40N and in (e) and (f) 80W and 40N.

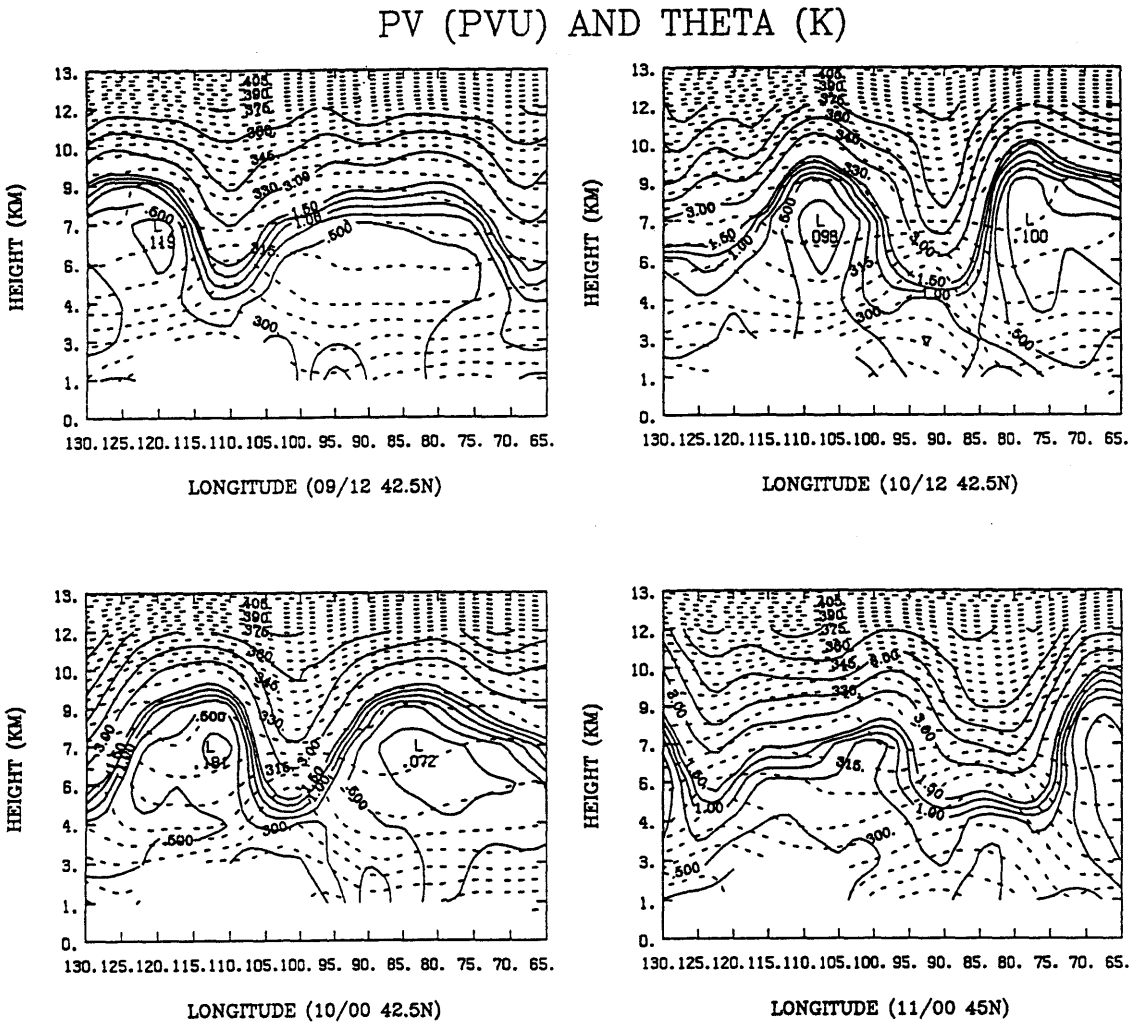


Figure 4.2 Cross sections of PV and potential temperature (format as in figure 3.5) (a) 12Z 09, 42.5N; (b) 00Z 10, 42.5N; (c) 12Z 10, 42.5N; (d) 00Z 11, 45N. Ordinate is pseudoheight (proportional to $1-\pi(p)/\pi(p_0)$); abscissa is longitude (degrees west).

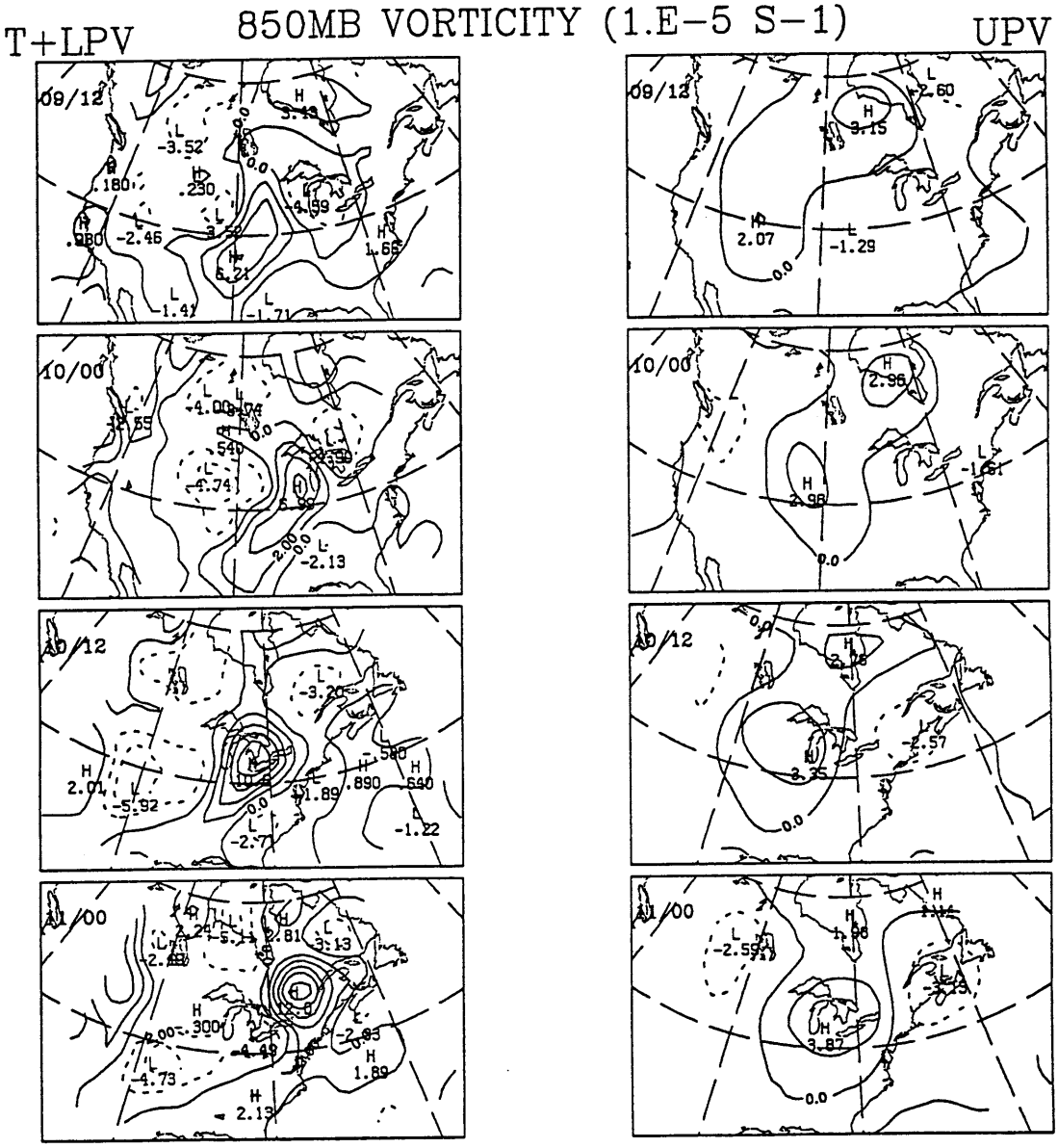


Figure 4.3 Perturbation vorticity at 850mb. Left column shows vorticity associated with the lower boundary θ and PV perturbations at 850mb and 700mb. (a) 12Z 09; (b) 00Z 10; (c) 12Z 10; (d) 00Z 11. Right column is vorticity from upper PV distribution (perturbations at and above 500mb). (e) 12Z 09; (f) 00Z 10; (g) 12Z 10; (h) 00Z 11. Contour interval is $2 \times 10^{-5} s^{-1}$. Zero contour is solid, negative values dashed. Central longitude line in (a),(b),(e) and (f) is 100W, in (c), (d),(g) and (h) it is 80W.

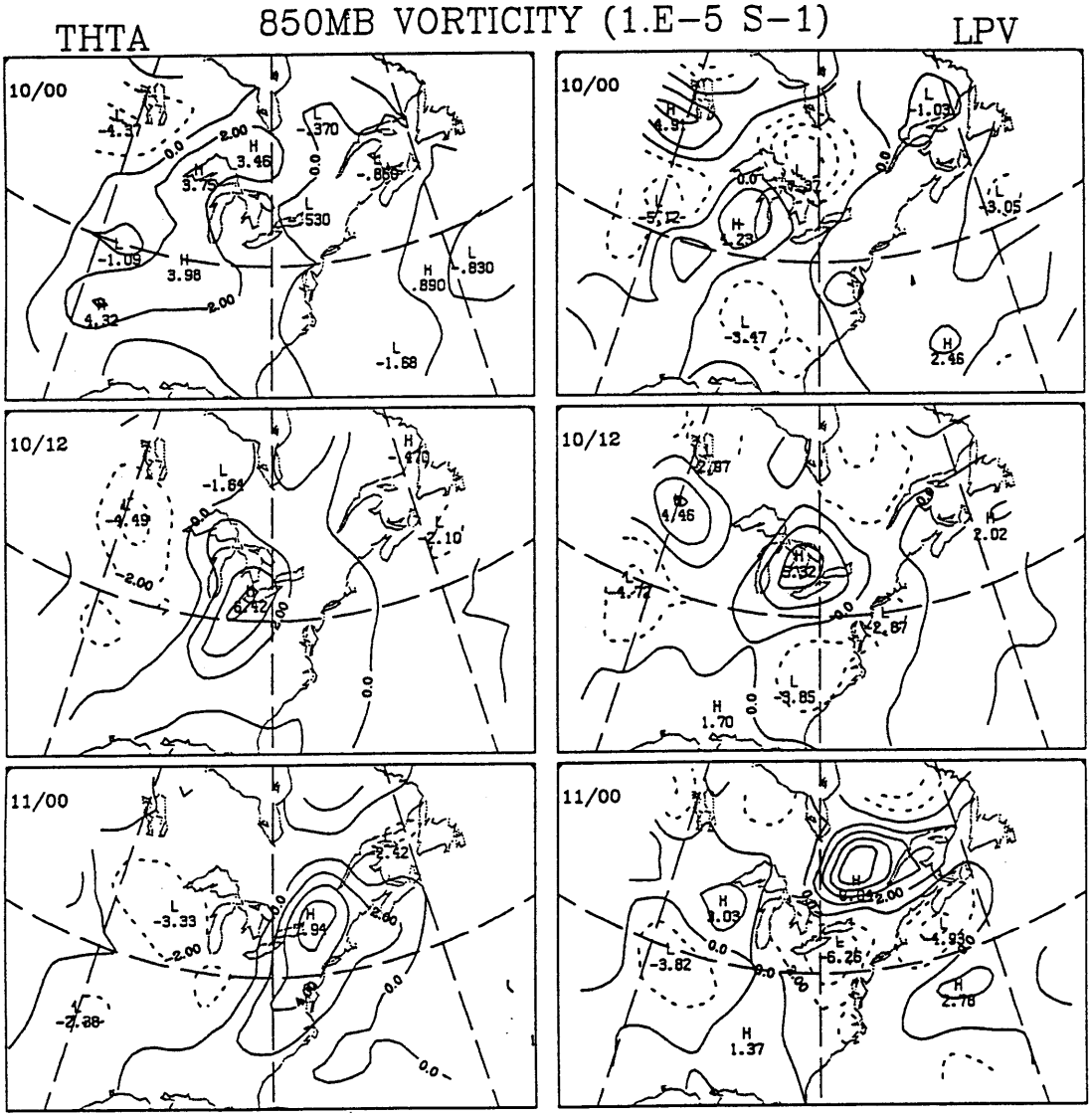


Figure 4.4 Perturbation vorticity at 850mb. Left column shows vorticity associated with the lower boundary θ, right column is for lower tropospheric PV. (a) 00Z 10; (b) 12Z 10; (c) 00Z 11; (d) 00Z 10; (e) 12Z 10; (f) 00Z 11. Central longitude line is 80W in all plots.

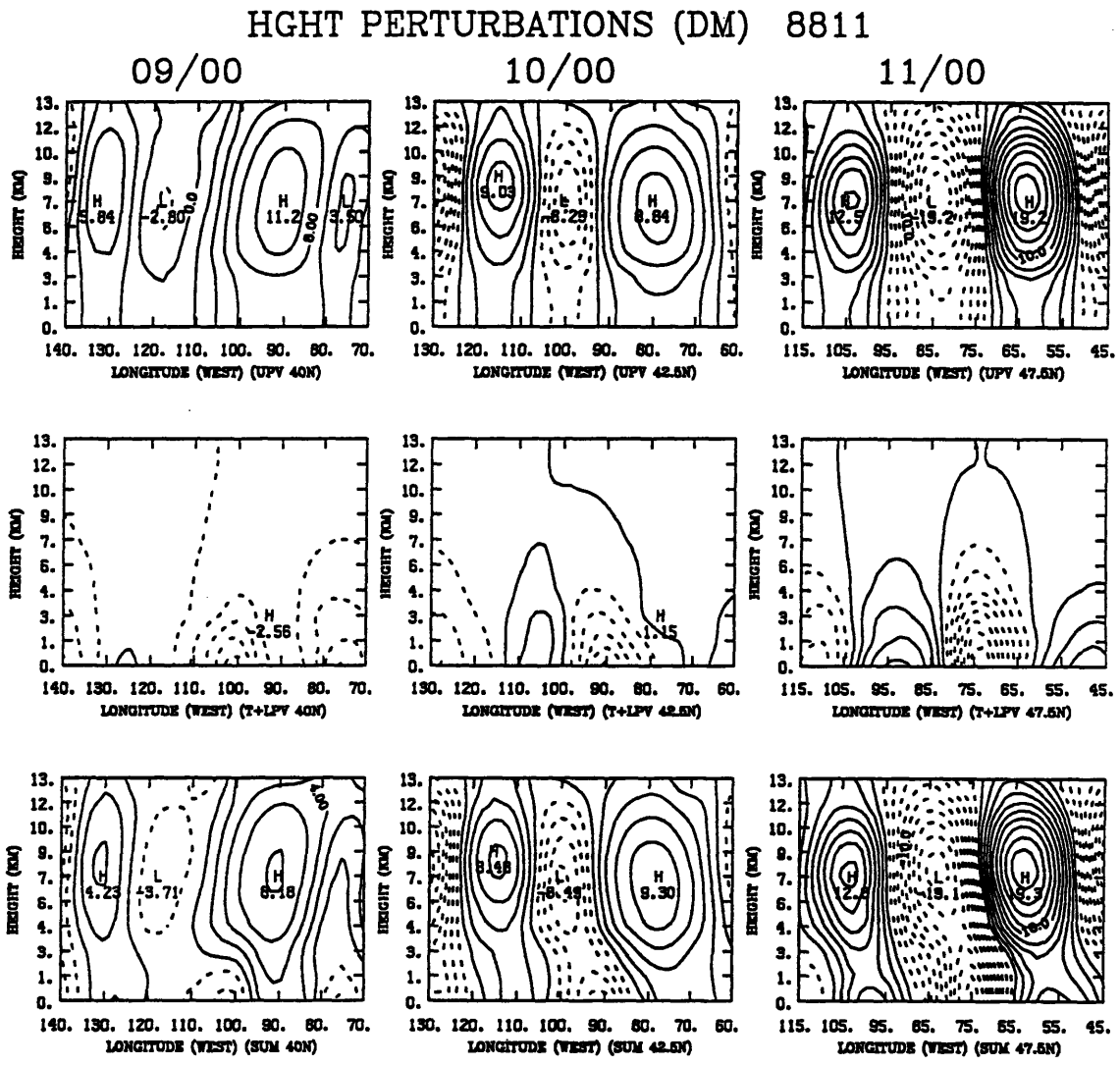


Figure 4.5 Cross sections of geopotential height perturbations at constant latitude (plotting conventions as in figures 3.11 and 3.12). Left column: 00Z 09; middle column 00Z 10; right column 00Z 11. Figures (a), (d) and (g) show heights from upper PV anomalies; (b), (e) and (h) from lower PV and θ_B; (c), (f) and (i) show the total perturbations.

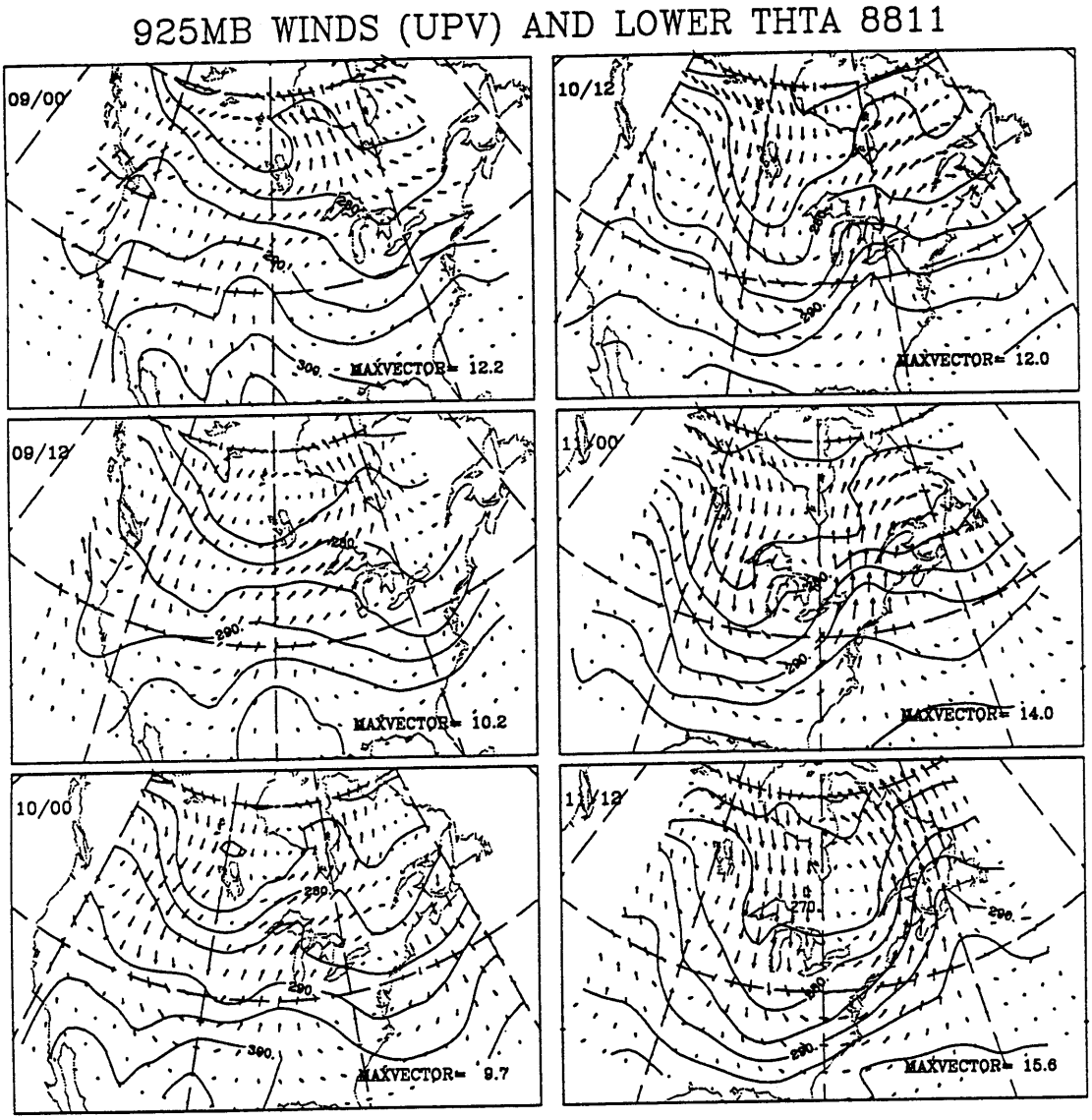


Figure 4.6 As in figure 4.1 but the winds are associated with the upper PV only.

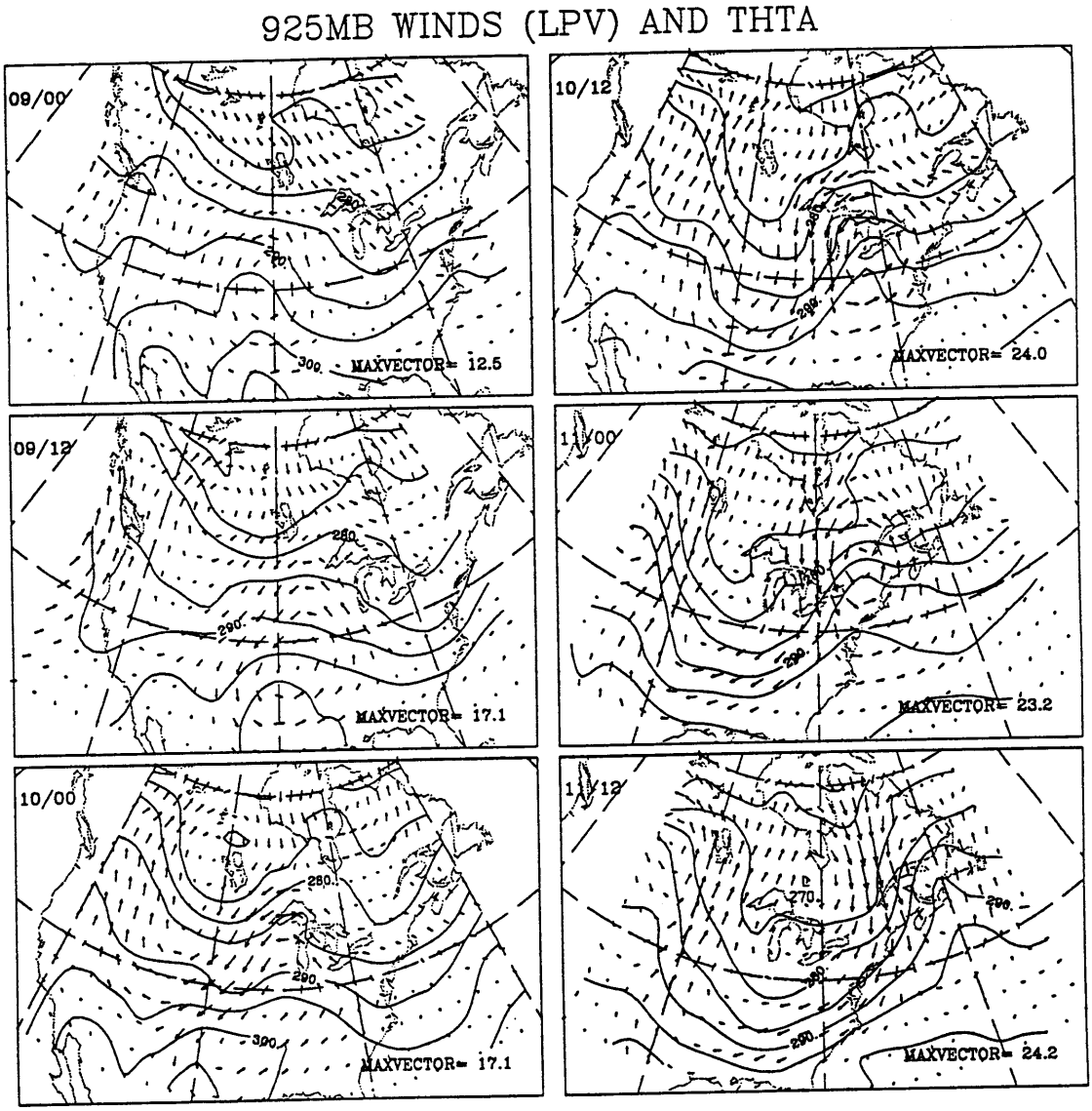


Figure 4.7 As in figure 4.1 but with winds from the lower PV and boundary potential temperature perturbations.

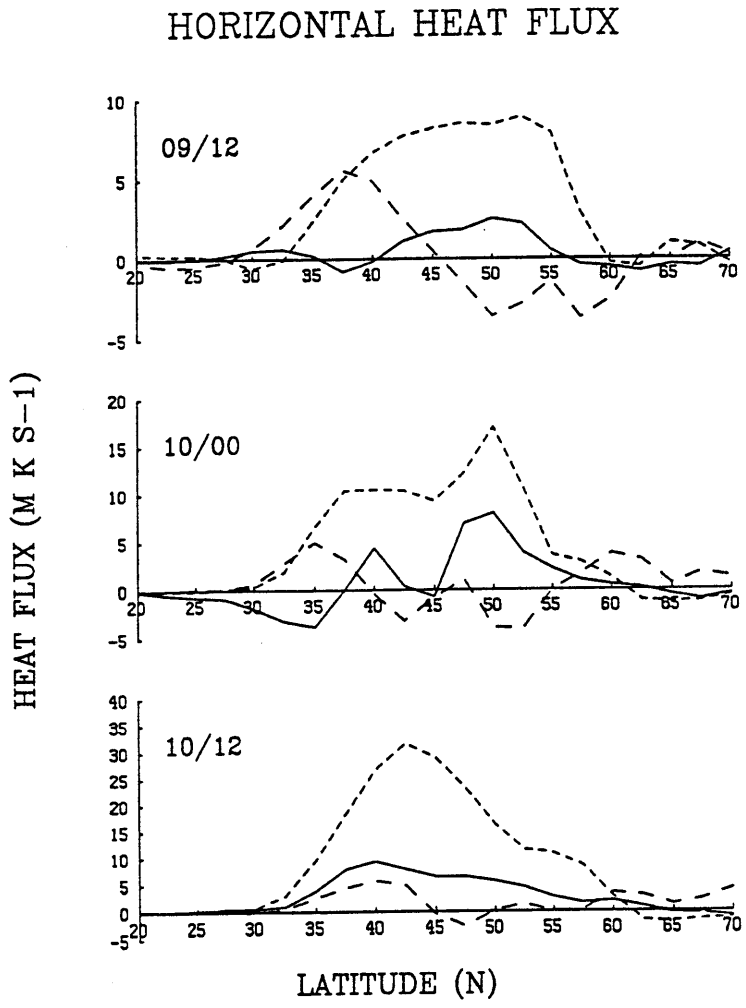


Figure 4.8 Heat flux at the lower boundary averaged zonally over a wavelength (40 degrees longitude as 40N). Contribution from the upper PV appears with short dashed lines, that from lower PV is drawn with longer dashes and the flux from the lower boundary temperature anomalies appears as a solid line. (a) 12Z 09 (120W-80w); (b) 00Z 10 (110W-70W); (c) 12Z 10 (100W-60W). Note scale change on ordinate.

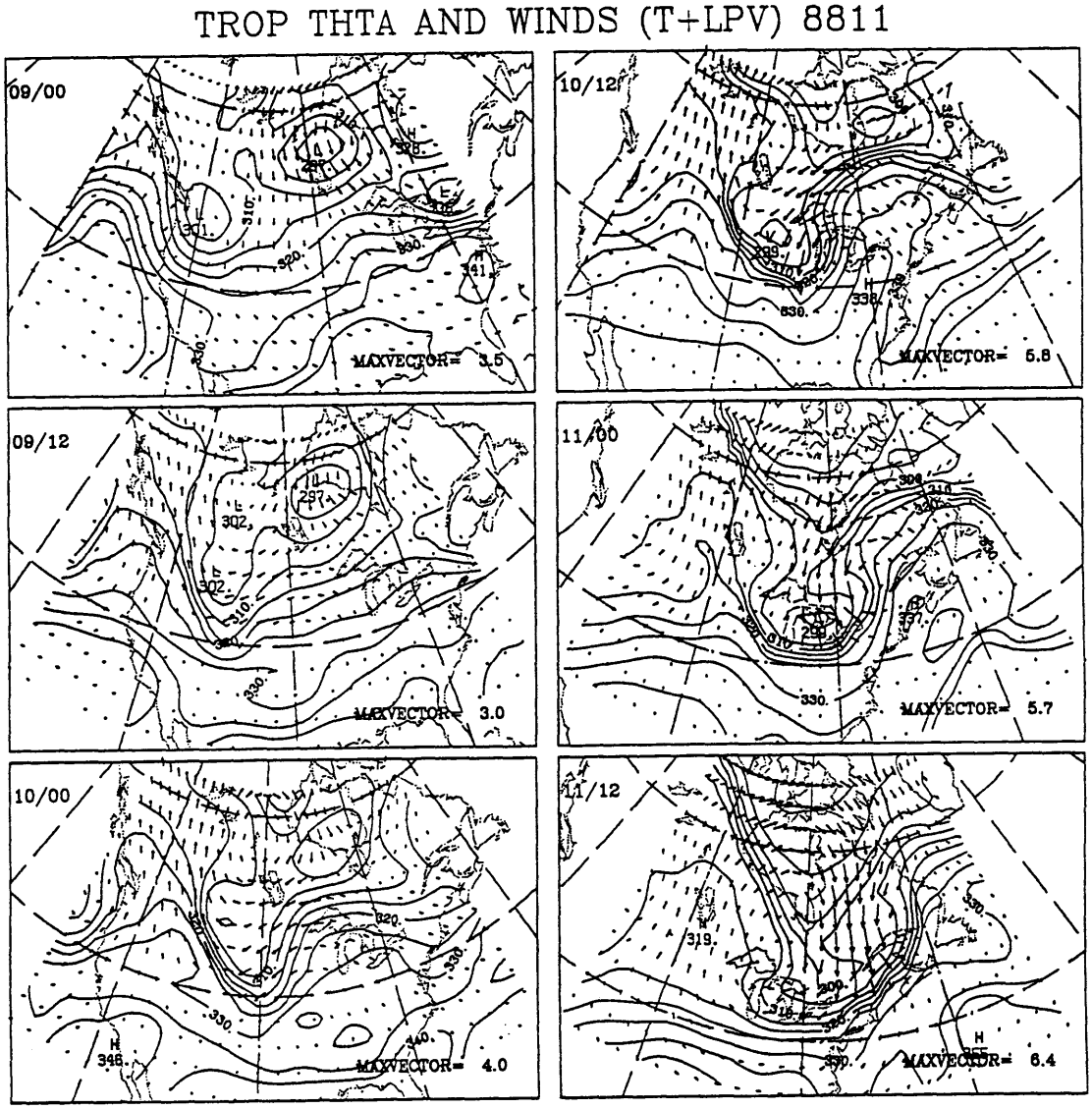


Figure 4.9 Tropopause winds from lower PV and boundary θ perturbations overlayed on tropopause potential temperature (q=1.5PVU). (a) 00Z 09; (b) 12Z 09; (c) 00Z 10; (d) 12Z 10; (e) 00Z 11; (f) 12Z 11. Contour interval for θ is 5K. Vector lengths exaggerated relative to other plots for clarity (see maximum magnitudes at lower right).

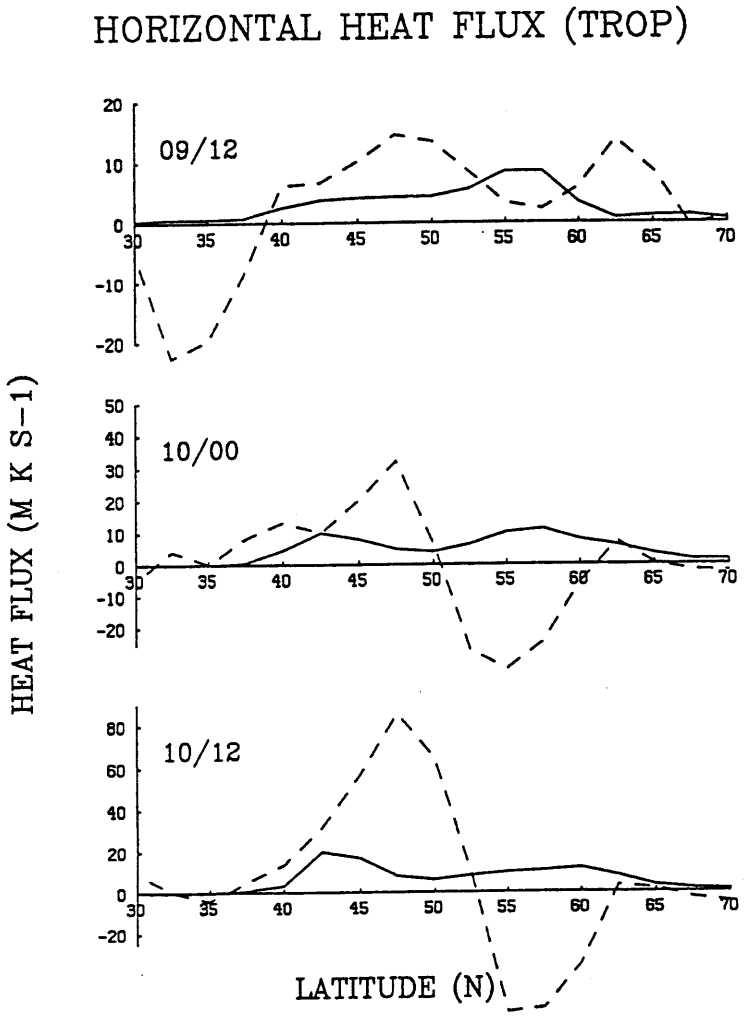


Figure 4.10 Heat fluxes at the tropopause. Conventions as in 4.8 except solid line refers to flux from lower PV and potential temperature anomalies, dashed to upper PV perturbations plus the mean flow.

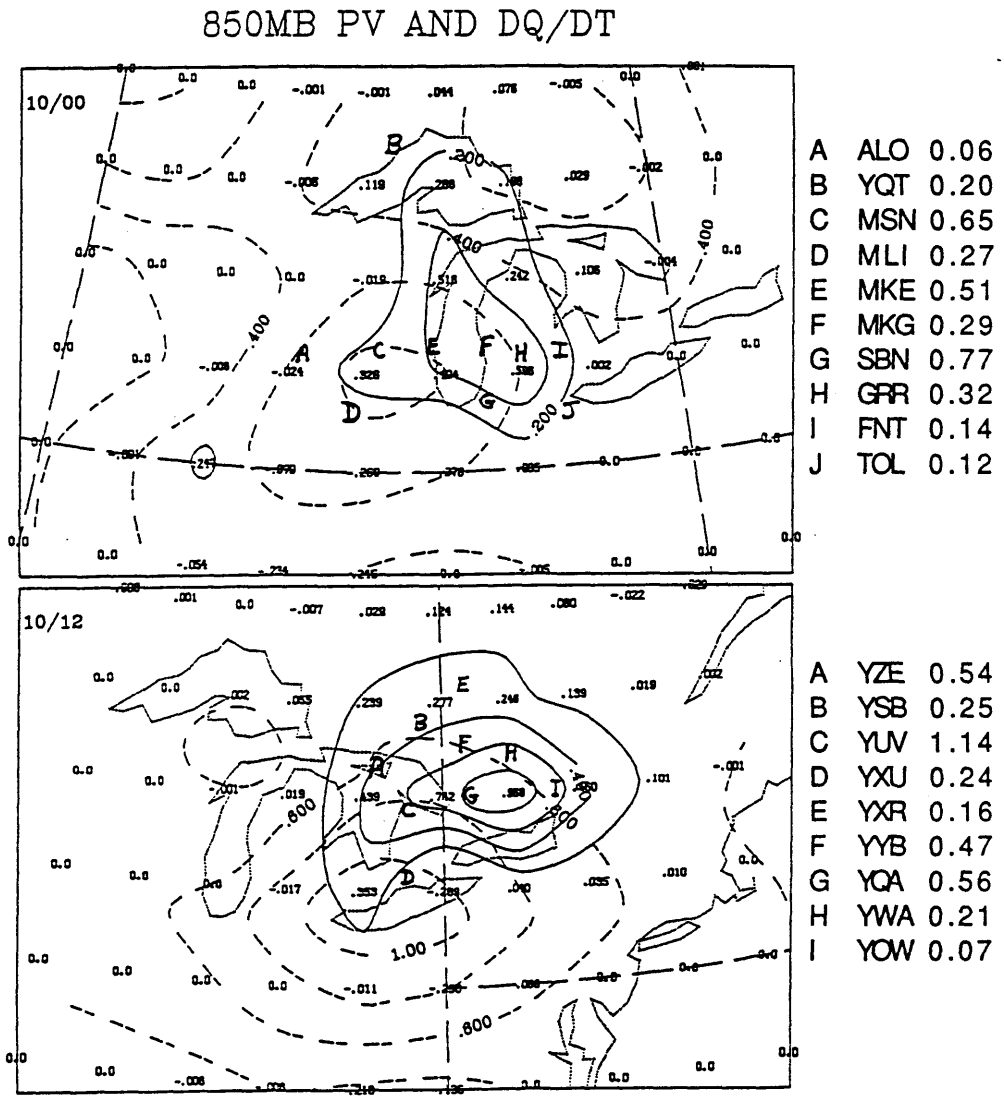


Figure 4.11 PV and PV generation. (a) for 00Z 10 November; dashed, PV (PVU) contour interval 0.2PVU; solid, PV generation from PBE calculation, contour interval 0.2 PVU per 12 hours. Only positive values are plotted. Numerical values are plotted at grid points. The generation values computed from station precipitation (indicated by letters on plots) appear in legend to the right of each plot. Values of PV generation are in the same units as the contoured field. Also given is the three letter station identification code. (b) as in (a) but for 12Z 10 November.

Case III. February, 1988

The cases examined to this point have emphasized the importance of potential vorticity features in the upper troposphere (or potential temperature anomalies on the dynamic tropopause). The present case is a robust cyclogenesis event in which upper level features are initially quite weak. In figure 4.12 we present the low level nondivergent winds and boundary potential temperature (as in figures 3.1 and 4.1). A weak wave in the thermal field is seen over the Great Lakes at 12Z 03 February. The baroclinic zone in this region is about twice as strong as that in case II (note 10K contour interval). No sharp fronts are evident as in case I; the region of temperature gradients larger than 3K per 1000km is more than 1000km wide. The main development occurs between 00Z on the 4th and 12Z on the 5th, with maximum low level winds exceeding the strongest of our other two cases by that time. The translational speed of the cyclonic circulation center over the last 24 hours of this development period averages about $20ms^{-1}$.

The evolution of potential vorticity is shown in figure 4.13 in cross section plots for times during the development period. The main feature is seen as a tropopause undulation with a trough centered near 100W at 00Z the 4th. The wavelength of this perturbation is about 3000km and between 00Z and 12Z the 4th, its eastward progression averages between 15 and $20ms^{-1}$. The

overall structure at these times is very similar to the trough in case I, though initally much weaker. By 12Z the 4th, there are hints of high potential vorticity air extending downward along the isentropes (dashed) both to the east and west of the trough. Also evident is a low level maximum of PV near 77W at 12Z the 4th with a maximum value exceeding 1 PVU.

The subsequent potential vorticity behavior is more complicated than in case II. There is significant deepening of the large scale polar vortex during the time of this development. This is evident in figure 4.13d, as the broad region of low tropopause between 110W and 55W, however, note that this section is taken further north than the others. It is perhaps more evident in figure 4.14 which shows the evolution of the (balanced) 300mb stream function field during this time. The section in 4.13d also passes through a prominent low level PV anomaly near 60W. Such a structure was also seen by Hoskins and Berrisford (1988) in an eastern Atlantic storm and bears some resemblance to the structure at 12Z 15 December (case I, figure 3.4, 90W).

Because of the large scale behavior during this period, we have modified the way in which the perturbations are calculated. Our main goal here was to remove the trend in the large scale from our perturbation fields. Thus we decomposed the time series of PV (and boundary θ) into a Fourier sequence at each gridpoint and removed the part that varied as $\cos(\pi t/T)$ where T is 5 days. This implies that the mean flow variations have a period of 10 days by definition. As a result, we compute a "mean" field for each day and

subtract this from the total to get the perturbation. This was the only one of the three cases where the coefficients of the lowest frequency of variation were larger than the rest.

The total perturbation field is broken into the same three parts as in the last case, upper PV (q at 500mb and above), lower PV (850 and 700mb) and boundary potential temperature. We present the contribution from each of these parts to the 850mb perturbation vorticity in figure 4.15. As in case II, the low level PV perturbation is associated with large vorticity values, exceeding $1.2X10^{-4}$ s^{-1} at 12Z the 5th. This feature is located slightly upshear of the warm thermal anomaly at early times, but is basically colocated with it by 12Z the 5th. There is also a negative perturbation of vorticity related to the lower PV to the east of the positive extremum at the first two times shown. As we shall see, this vorticity gradient is associated with southerly winds in phase with the warm thermal anomaly. The low level reflection of the upper PV is hardly noticable until 12Z the 15th and even then, it does not contribute much to the cyclone vorticity directly. However, there is still important growth of potential vorticity features aloft, manifested at low levels primarily in terms of anticyclonic vorticity to the northeast of the surface cyclone.

The intense low level PV feature is again suggestive of the importance of nonconservative processes, and from previous experience, we anticipate latent heat release as a key factor. In figure 4.16, we present PV and PV generation rates in a format

very similar to that in figure 4.11. For Canadian stations, we have used the 6 hour precipitation totals for stations at 12Z the 5th and estimated the duration of the precipitation from the surface hourly reports. The calculation from the ω equation shows a maximum in generation slighly downshear of the lower PV anomaly (see figure 4.15), whereas the station reports indicate more generation at the location of the anomaly. The difference at 12Z the 4th may be attributable to orographically induced precipitation on the western slope of the Appalachians. Our PBE calculations would not necessarily capture this because of its mesoscale nature. At 12Z the 5th, the position difference can be attributed to the time interval over which the precipitation is measured. The station data is more indicative of the precipitation rate a few hours before 12Z which is equivalent to perhaps 200km upshear given the speed of the system.

To show additional support for the calculations in figure 4.16b, we present output from NMC's Nested Grid Model (NGM), a 16 layer, hydrostatic primitive equation model run in operational mode twice daily (Hoke et al. 1989). We have reproduced the output from the 12 hour forecasts valid for 12Z the 4th and 12Z the 5th. Figure 4.17 shows 700mb vertical velocities ($-\omega=-Dp/Dt$) from the NGM along with the same quantity from the PBE calculation. There is quite good agreement between the two fields, certainly the weaker values of the extrema in our PBE calculation are expected in light of the NGM's superior resolution (90km in the horizontal at 60N). Twelve hour precipitation totals from the NGM are as large

as one inch just upshear of the maximum ascent at 12Z the 5th which is supported by the observed precipitation totals. This consistency between the observed precipitation, the model forecast and our calculation makes our estimate of the PV generation more plausible. Our interpretation of the origin of the lower PV anomaly once again centers on the generation by latent heat released in a region of stable precipitation. Of course, what we label as "stable" can include precipitation generated in very intense frontal circulations where the stability to slantwise displacements is vanishingly small. The main point is that since no intense showers were reported, nor were thunder or lightning noted by any of the observing stations, deep upright convection was likely not important.

The development of the lower boundary potential temperature perturbation seems to involve advection by both the winds associated with the lower PV (early stages) and the winds from the upper PV (later stages). Figure 4.18 shows these low level wind fields overlayed on lower boundary θ. The upper PV distribution is clearly not influencing the thermal field development until after 12Z on the 4th. At 12Z the 4th and 00Z the 5th, a substantial contribution from the lower PV anomaly is evident. These can be quantified as in figure 4.19 which shows the potential temperature tendencies at these two times. The left column is for 12Z the 4th, the right column for 00Z the 5th. To calculate the tendencies from only part of the flow, we need to address the question of how one finds the appropriate vertical (and

irrotational) velocity fields. Though the differential operator in the omega equation is linear, the right hand side is not a linear function of the flow variables. The principle concern is how to treat the advection terms. We do this the same way as for the advection of PV, namely, the quantity doing the advecting is the perturbation; the quantity being advected is calculated from the total field. In the case of the tendency of θ_B, the horizontal advection by the nondivergent part of the flow dominates and the results are insensitive to the means by which we calculate the vertical velocities.

The results of this calculation show that, especially at 00Z the 5th, the potential temperature tendencies due to both flow fields are in mostly phase with the lower boundary thermal wave. In the presence of the observed basic gradient of potential temperature, this implies an amplification of the θ_B field. The θ tendency due to the flow associated with lower boundary thermal anomalies is not shown explicitly, but can be inferred from the plotted fields. Its effect is to simply propagate the thermal wave eastward along the baroclinic zone.

To investigate the behavior at upper levels, we again display the upper PV disturbance using tropopause maps. Figure 4.20 presents the winds from the lower PV and boundary θ features added together, figure 4.21 shows the total winds. The magnitude of the winds in figure 4.20 is considerably greater than for case II (figure 4.9), reaching $15ms^{-1}$ by 00Z the 6th. This figure is strongly suggestive that much of the amplification of the upper PV

is tied directly to that circulation. Note that, especially at 12Z the 5th, the scale (along the isentropes) of the advecting flow matches the scale of the amplifying anomaly. We thus appear to have a case where the coupling of the tropopause and lower tropospheric features is central to the development process.

A couple of additional points seem worth mentioning. First, there is rapid growth of a positive θ_T anomaly near 50N and 40W by 12Z the 5th. This feature is associated with a column of very low PV air, with negative values. We have low confidence in this feature, however, as it shows a lack of temporal continuity and occurs in a region with little data. There also does not seem to be a plausible mechanism for its generation. Second, because of the variation in the height of the tropopause between positive and negative potential temperature pertubations ("cold" signifies a low tropopause while a high tropopause is "warm"), a circularly symmetric flow from the low level anomalies has an asymmetric distribution when interpolated to the tropopause. Thus the amplification of a tropopause wave will tend to be faster in the cold phase than in the warm phase (at least linearly speaking). Second, there was some growth of the upper wave before the tropopause winds from the lower anomalies became significant. However, it was not until the amplification associated with the lower perturbations began that the low level circulation from the upper PV had any influence on the low level development.

As an overview of this case, we present figure 4.22, which shows cross sections of geopotential perturbation fields for 12Z

04 and 12Z 05 February. In this case, the mean flow is not really zonal as it was in case II (see figure 4.23 for a comparison). These sections were therefore computed along the mean tropospheric thermal wind (1000mb to 400mb layer), hence the abscissa represents the distance from southwest to northeast in that direction. Although we allow our "mean" to vary slowly in this case, the differences in the mean thermal wind direction between these two times were slight. At 12Z the 4th, the left edge of the cross section corresponds to 35N, 100W, the right edge to 45N, 55W. At 12Z the 5th, the borders are at 37N, 85W and 50N, 40W. Interpolation from the grid fields onto this section was done by performing a weighted average of the four grid points nearest the desired point in the plane of the cross section. The weighting factor was the reciprocal of the distance between the cross section point and the grid point from which data was being interpolated.

For each time, we have shown the heights associated with each of the three perturbations as well as the total perturbation. The main phase shift is found between the tropopause and low level anomalies, but at 12Z the 4th, there is a detectable shift between the low level PV and boundary θ features. This tilt apparently disappears by 12Z on the 5th, although there is still some evidence of it in figure 4.18c.

At first, the upper PV has little or no signature at the surface. In fact, it is nearly 180° out of phase with the lower thermal field. There is definitely a reduction of this phase shift over the next 24

hours, but, as in the last case, this slows down as the perturbations approach a relative displacement of 1/4 of a wavelength. Continued growth is implied by the favorable tilt in figure 4.22d, but aloft (figure 4.20f) the tropopause anomaly is beginning to deform in a similar fashion to case I, though to a lesser extent. By 00Z the 6th, the upper and lower anomalies are nearly superposed and growth ceases. This superposition process does not add much to the intensity of the cyclone however.

Though there was a transient period in the early stages, the bulk of this development occurred during a period of relatively little phase structure variation. The low level PV appeared to be involved in the amplification of the boundary thermal wave initially, but rapid growth began when that circulation became reinforced by the circulation from the tropopause anomaly. The structure in the early stages of growth was not like the classical Charney solution since the phase shift between the PV and potential temperature perturbations was quite small (see Snyder 1989 for shortwave PV structure of dry modes). It is not known if the addition of condensation from stratiform precipitation in that problem could have resulted in something closer to the observed structure.

The role of moisture in this case was profound, primarily manifested in a positive low level PV maximum. First, the low level PV was found to aid in the amplification of the thermal wave in the early stages of development. Second, this anomaly (if we may speak of the same one) grew in phase with the warm

temperature perturbation at the boundary and contributed directly to the cyclone circulation later in the cyclogenesis. The winds from this feature alone approached $15ms^{-1}$ by 12Z the 5th with a maximum vorticity exceeding $10^{-4}\ s^{-1}$. Third, the circulation from this feature reinforced that from the θ_B anomalies in advecting tropopause potential temperature.

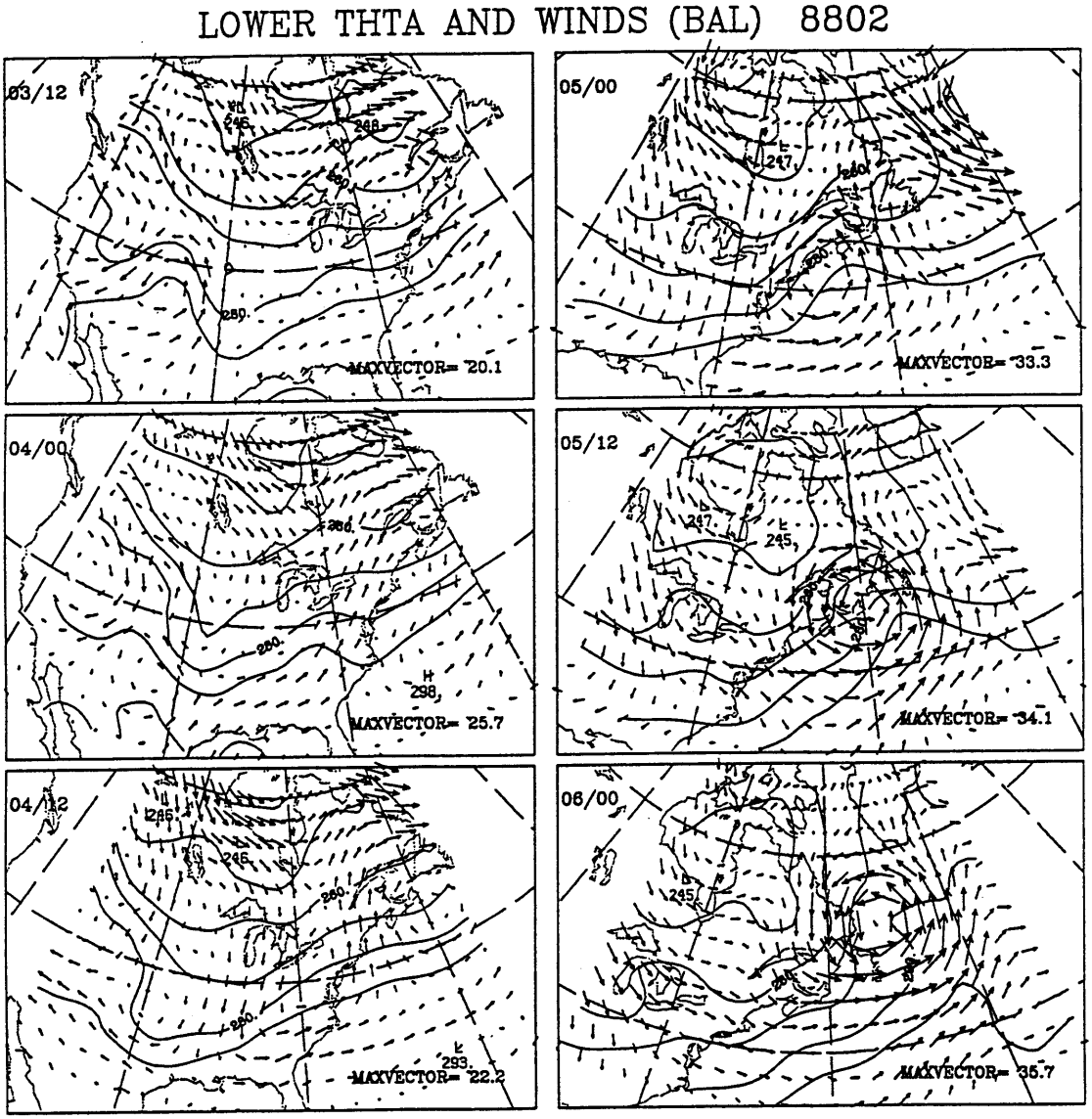


Figure 4.12 Balanced nondivergent winds (925mb) and lower boundary potential temperature. Contour interval for θ is 10K. (a) 12Z 03; (b) 00Z 04; (c) 12Z 04; (d) 00Z 05; (e) 12Z 05; (f) 00Z 06. For reference 40N latitude line passes through the middle of the first three plots and near the bottom of the last three. Central longitudes are (a) 95W (b) 87W (c) 80W (d) 70W (e) 65W (f) 60W.

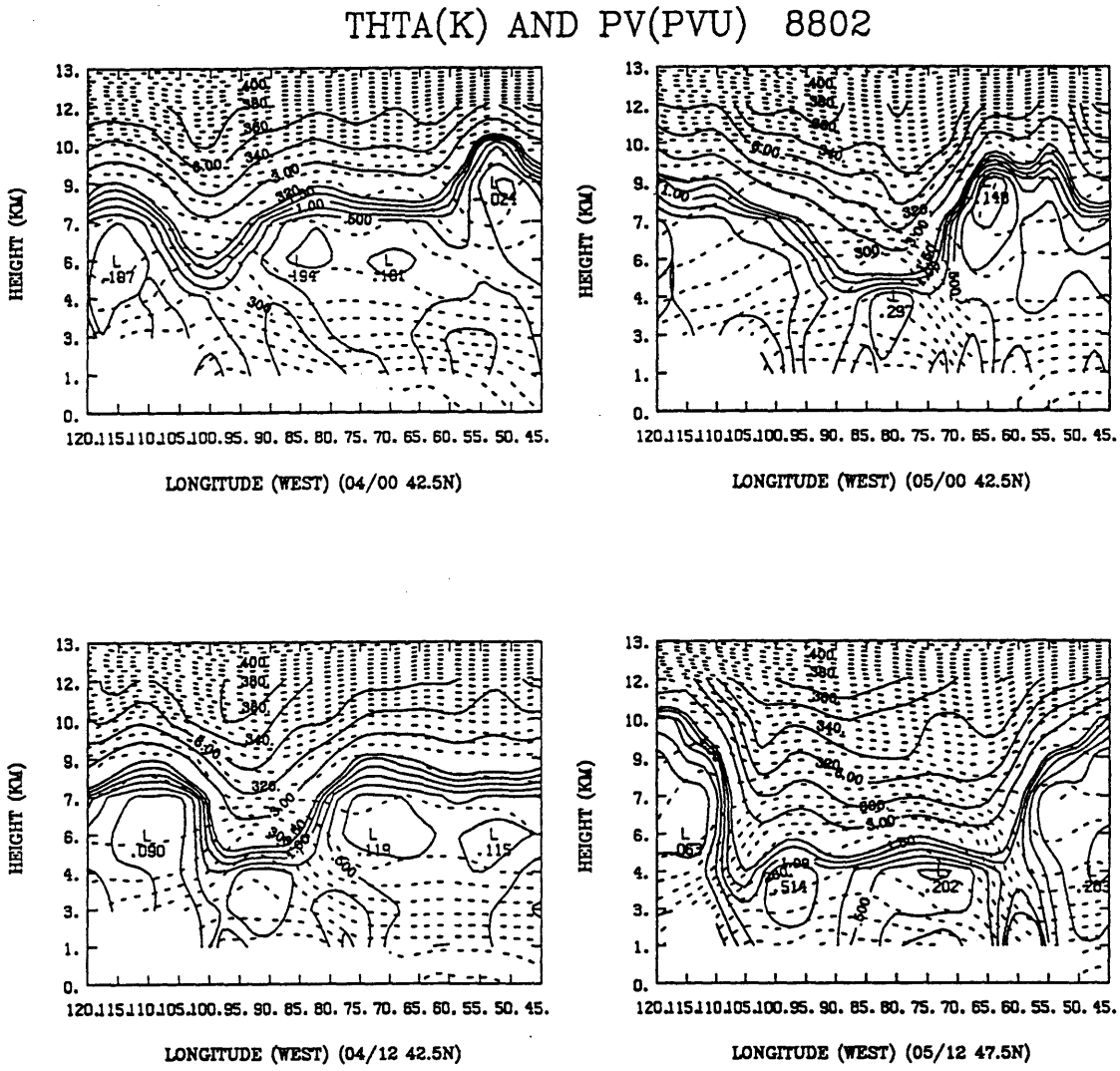


Figure 4.13 Potential vorticity and potential temperature. Format as in figures 3.5 and 4.2. (a) 00Z 04, 42.5N; (b) 12Z 04, 42.5N; (c) 00Z 05, 42.5N; (d) 12Z 05, 47.5N.

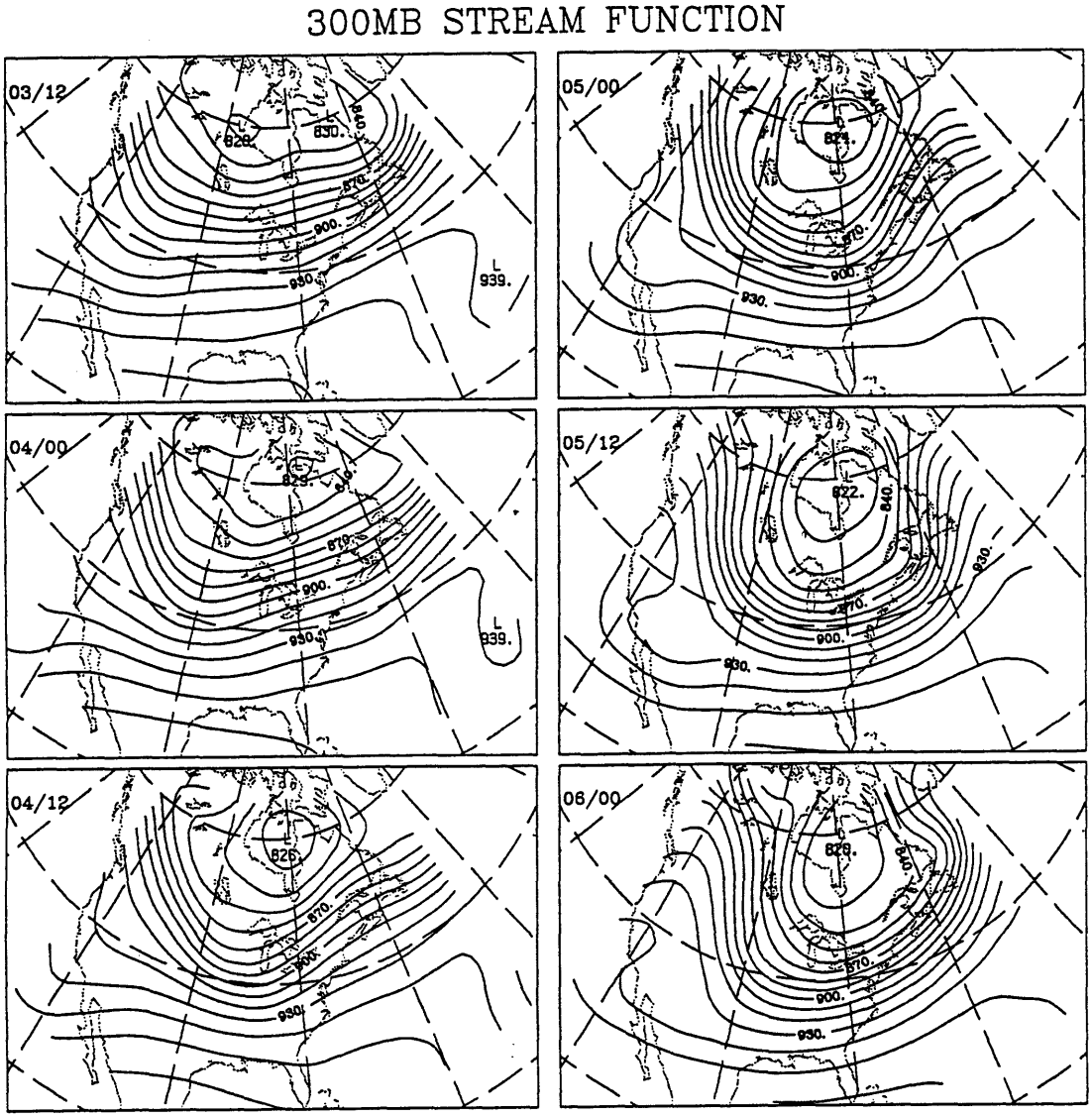


Figure 4.14 Stream function at 300mb. Contour interval is 10dm (a) 12Z 03; (b) 00Z 04; (c) 12Z 04; (d) 00Z 05; (e) 12Z 05; (f) 00Z 06. For each plot, the latitude line near the center is 40N, the longitude line is 80W.

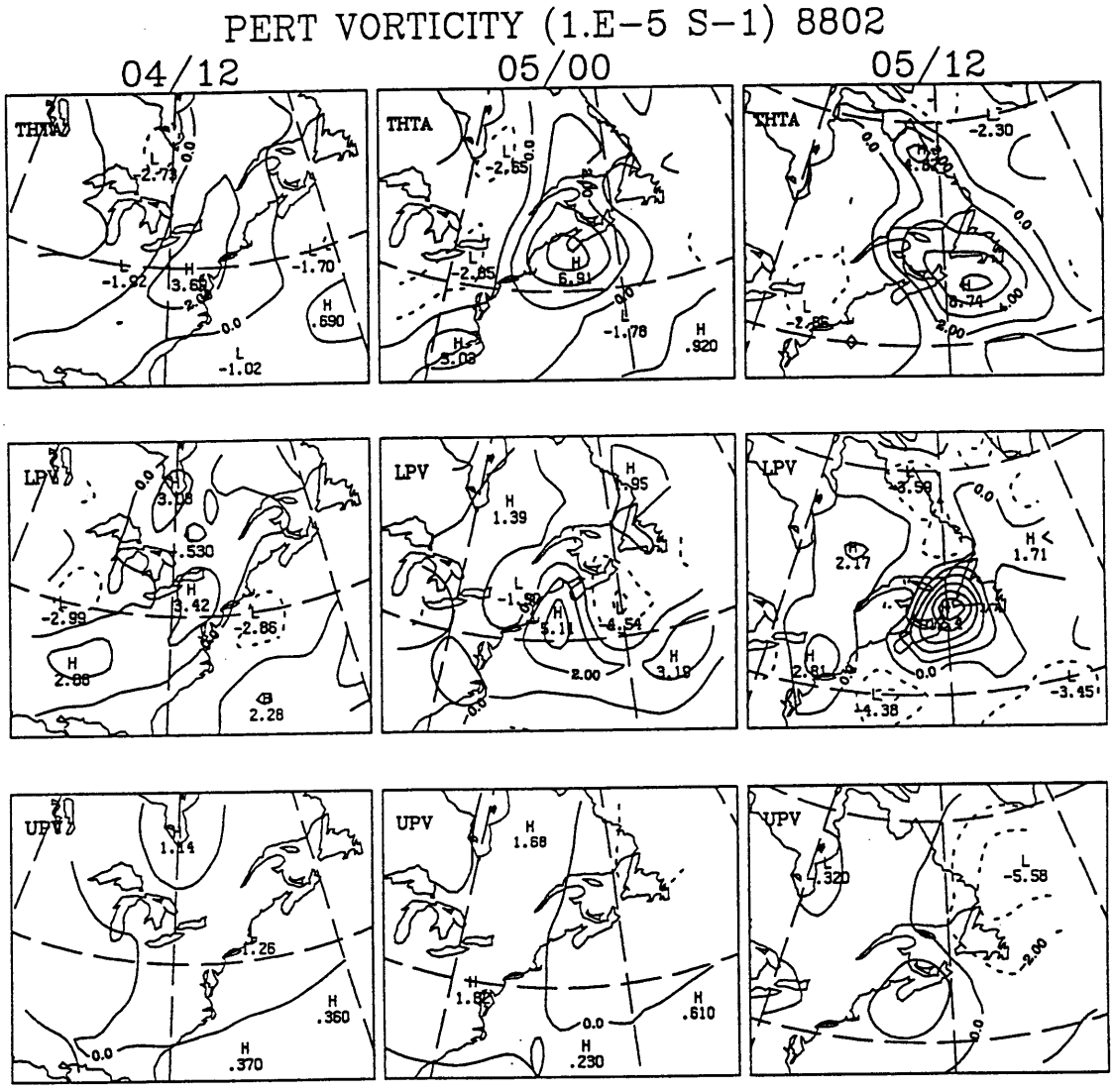


Figure 4.15 Perturbation vorticity at 850mb. Contour interval is $2x10^{-5}$ s^{-1} and negative contours appear dashed. Left column is for 12Z 04, vorticity associated with (a) lower boundary θ (b) PV at 850 and 700mb (c) PV at and above 500mb. Middle column and right column are the same as at left, except for 00Z and 12Z the 5th respectively.

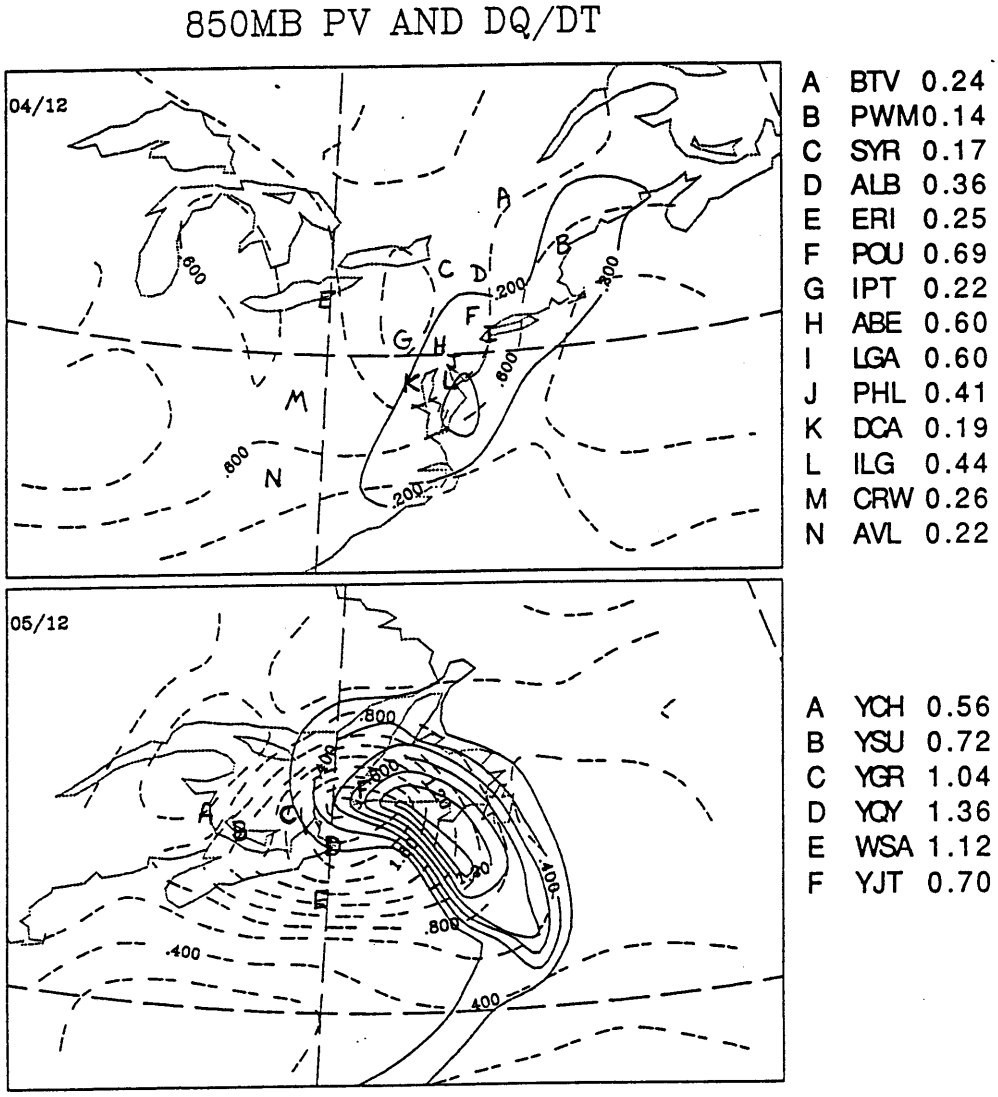


Figure 4.16 PV (PVU) and PV generation (PVU per 12 hours). Format as in figure 4.11 for (a) 12Z 04 and (b) 12Z 05.

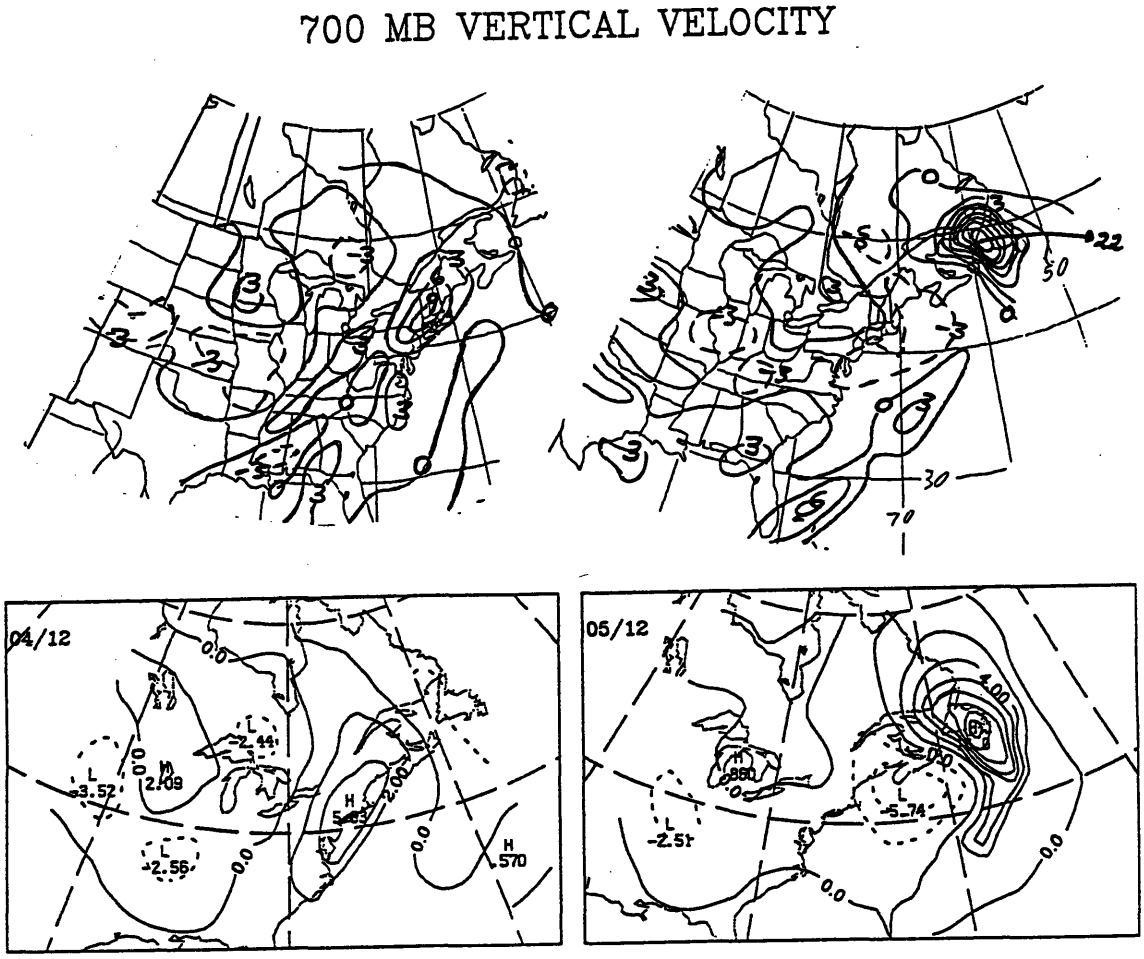


Figure 4.17 700mb vertical velocities (-ω). (a) 12hr NGM forecast valid for 12Z 04, contour interval is 3 μbar/sec; (b) calculated omega's from the prognostic balance equations at 12Z 04, contour interval is 2 μbar/sec; (c) as in a but for 12Z 05; (d) as in (b) but for 12Z 05.

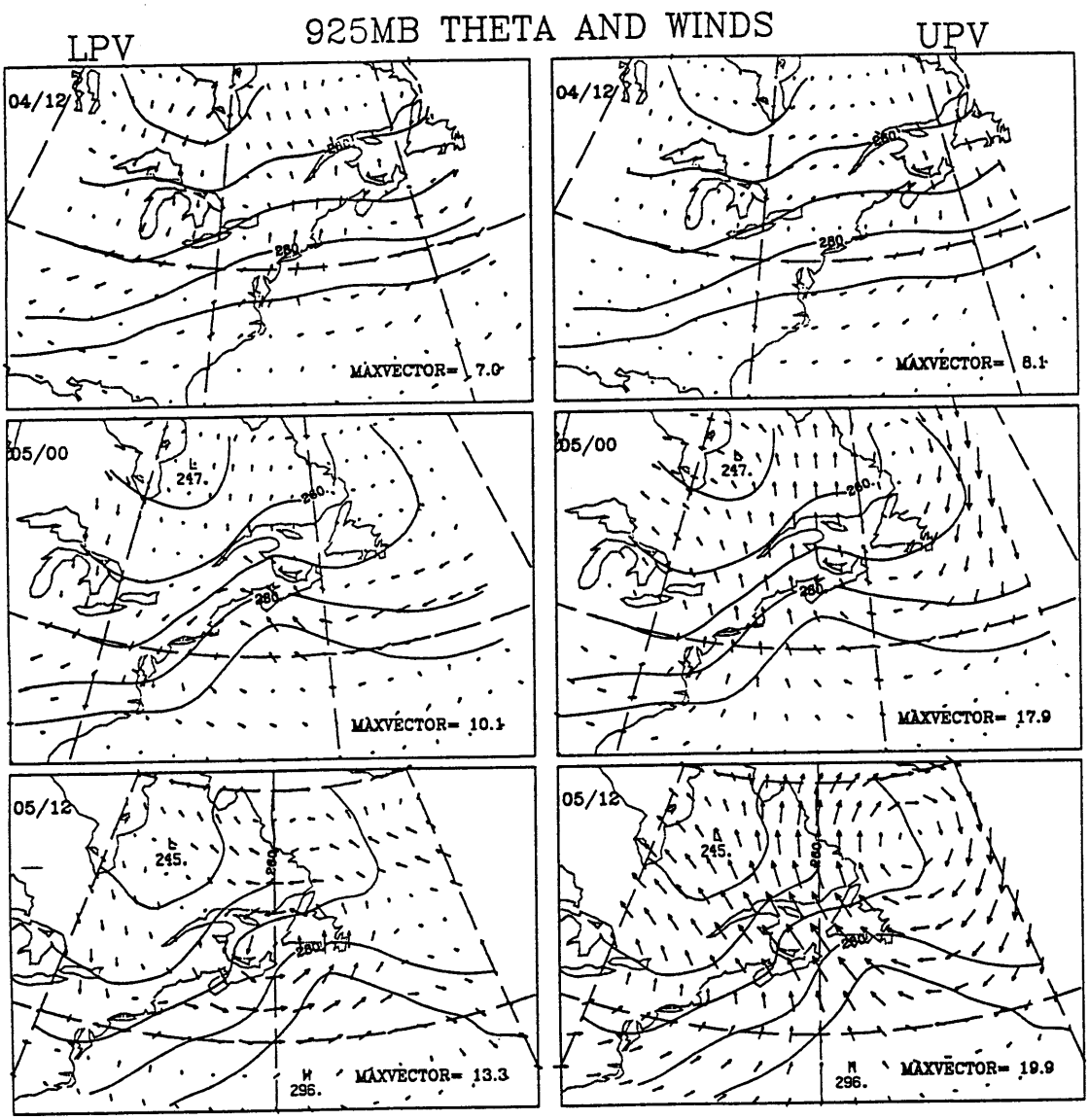


Figure 4.18 925mb winds and lower boundary potential temperature (contour interval 10K). Left column shows winds associated with the lower PV anomalies for (a) 12Z 04; (b) 00Z 05; (c) 12Z 05. Right column is as left column but for the upper PV perturbations.

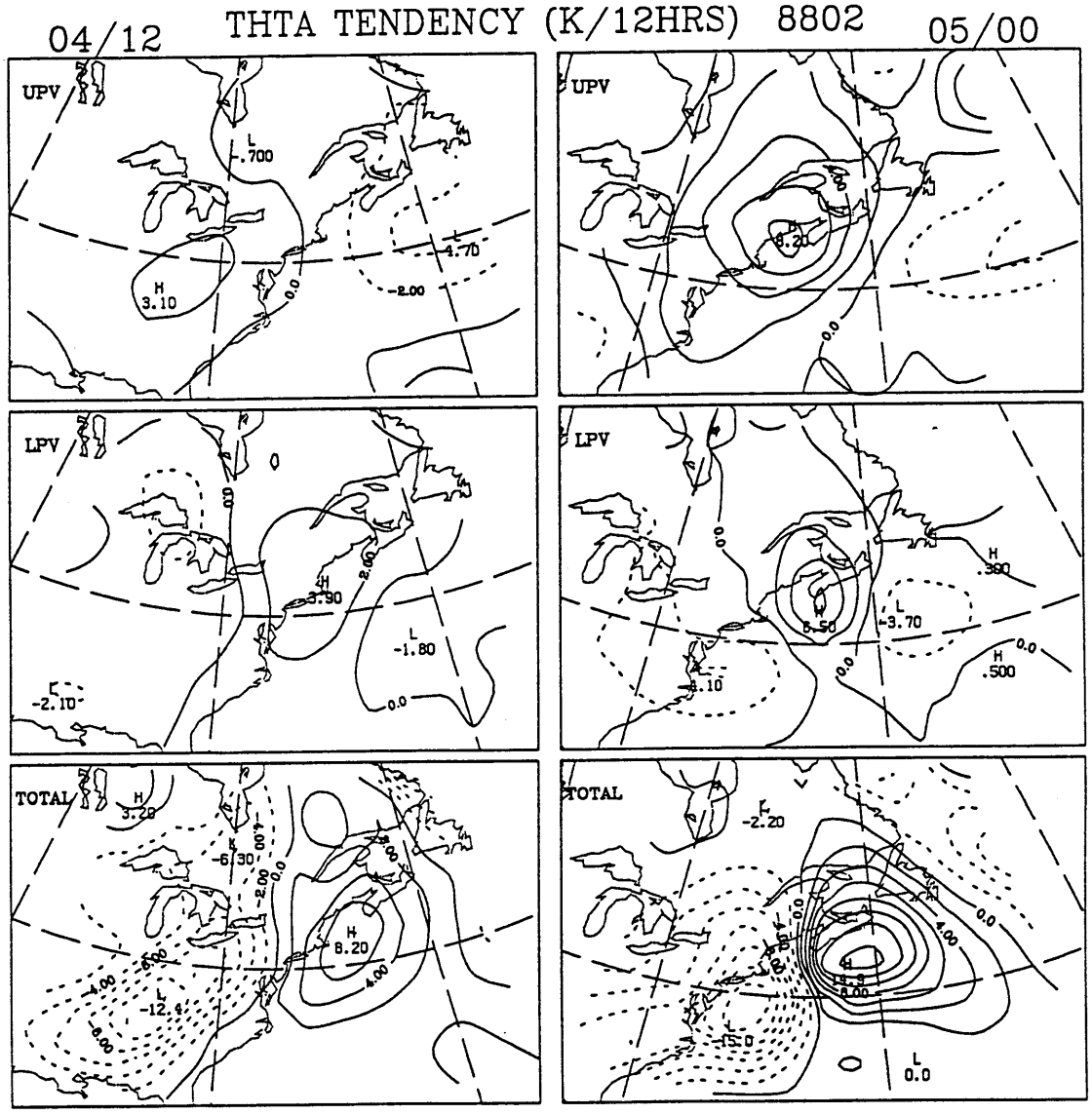


Figure 4.19 Tendency of lower boundary potential temperature (contour interval is 2K per 12hrs). Left column is for 12Z 04; tendencies are for (a) flow from upper PV perturbations (b) lower PV (c) total flow. Right column is as left column except for 00Z the 5th.

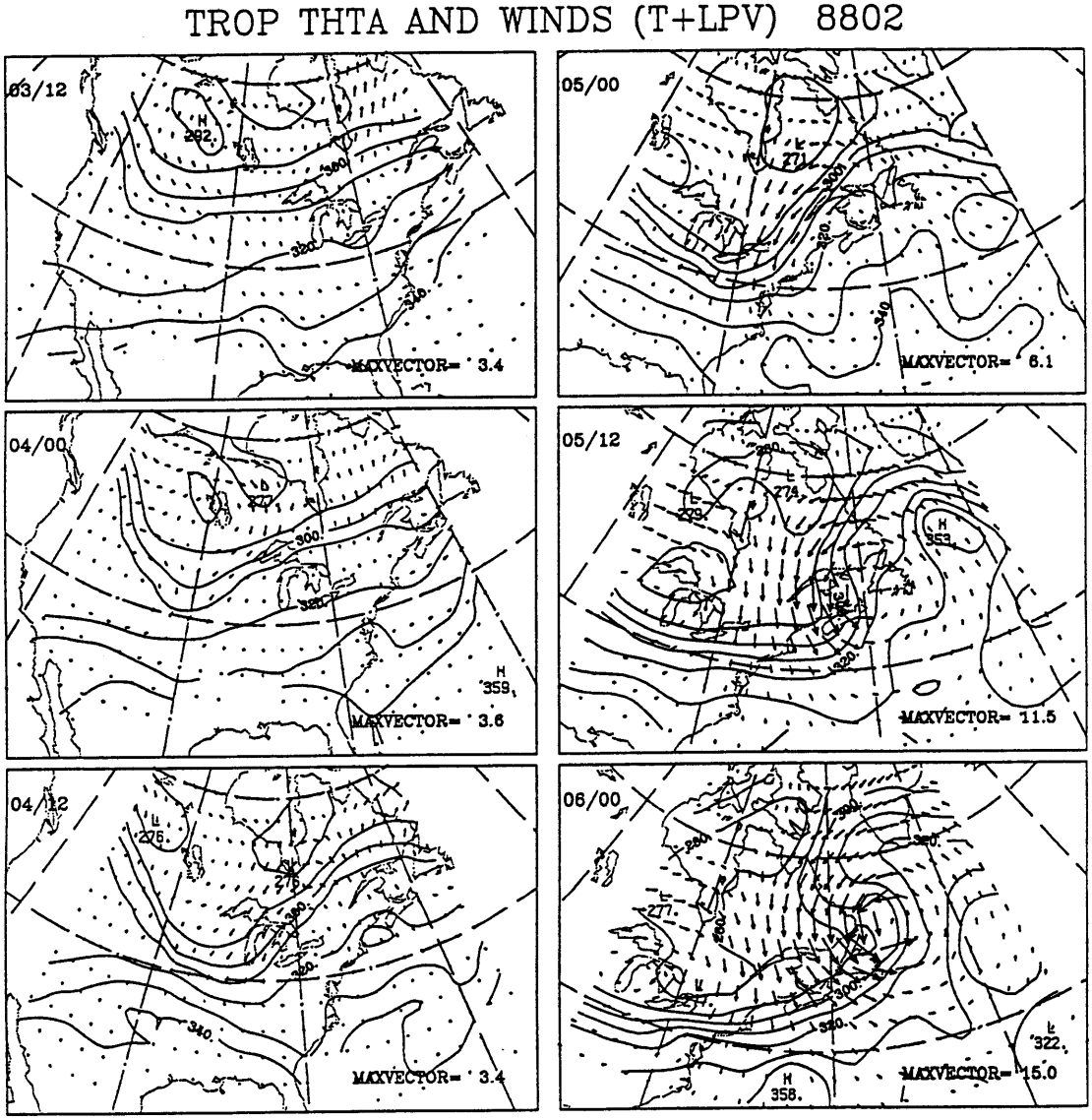


Figure 4.20 Tropopause potential temperature (10K contour interval, highest contour is 340K) and tropopause winds from the lower PV and boundary θ perturbations added together. (a) 12Z 03; (b) 00Z 04; (c) 12Z 04; (d) 00Z 05; (e) 12Z 05; (f) 00Z 06.

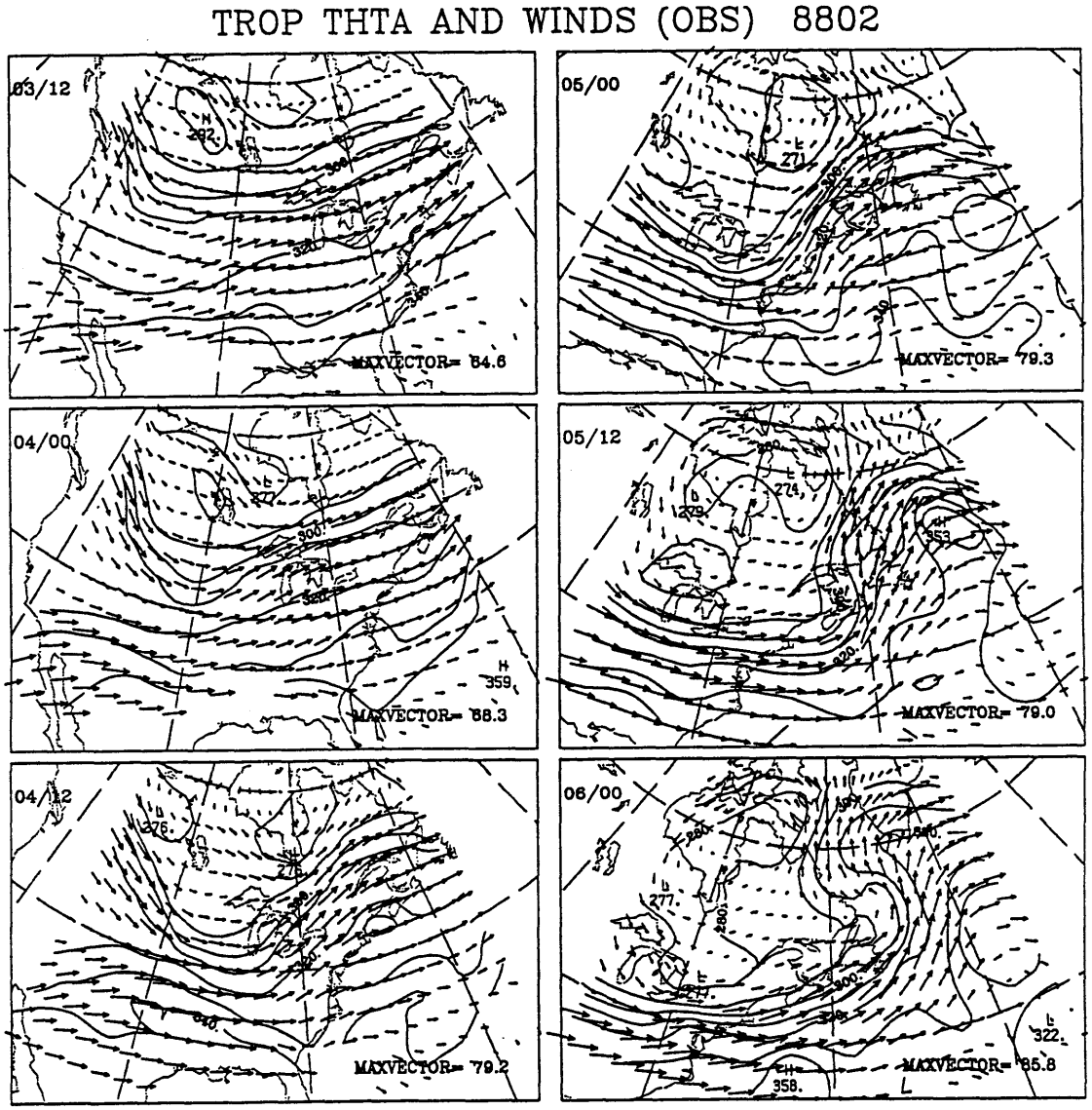


Figure 4.21 As in 4.20 except wind vector lengths have been scaled down by a factor of six.

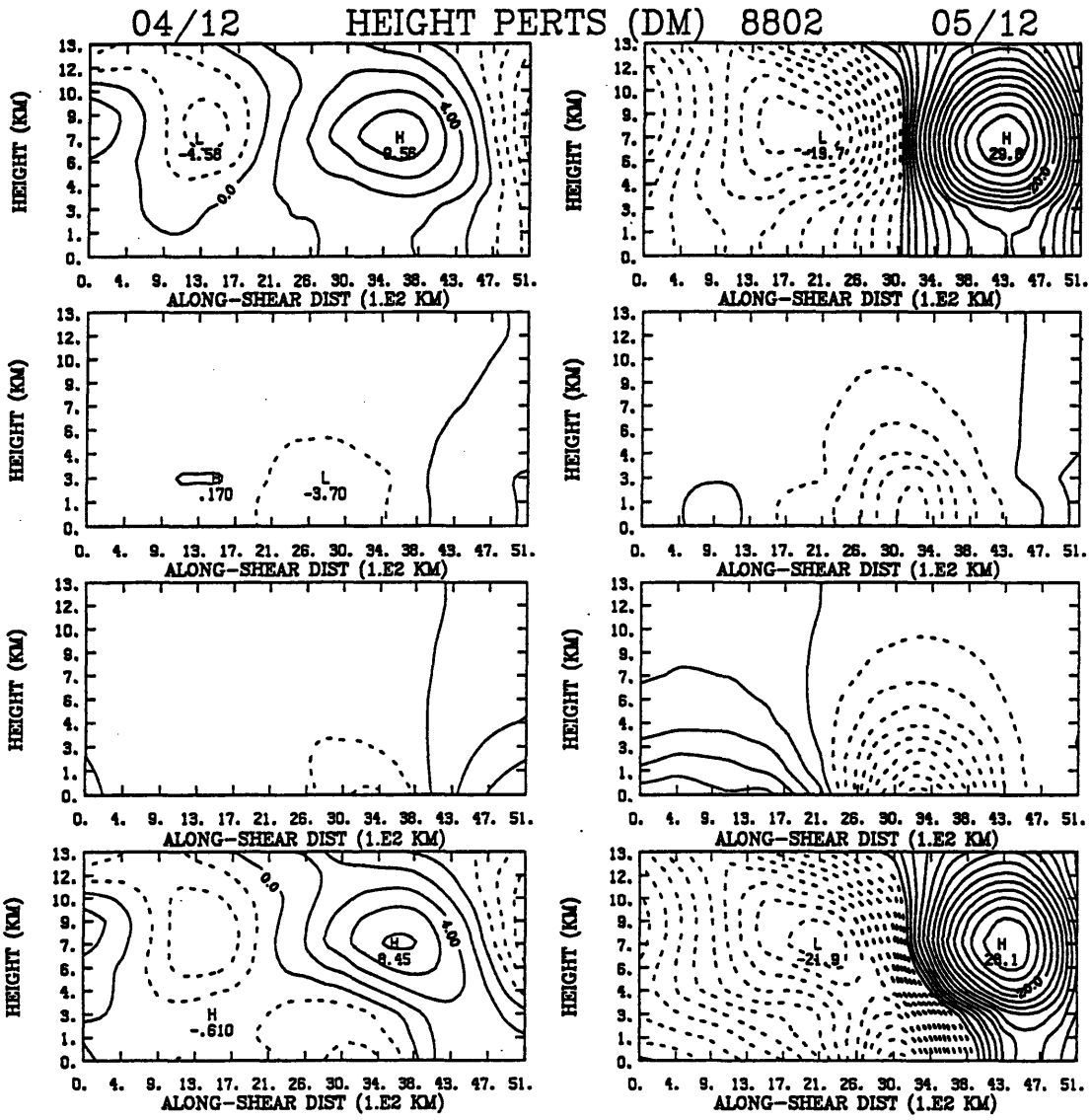


Figure 4.22 Vertical cross sections of geopotential height perturbations (contour interval 2dm, negative values dashed). The abscissa scale is distance along the section in hundreds of km, orientation of section described in text. Left column is for 12Z 04; perturbations are from (a) upper PV; (b) lower PV; (c) θ_B; (d) total perturbation. Right column is as left column but for 12Z 05.

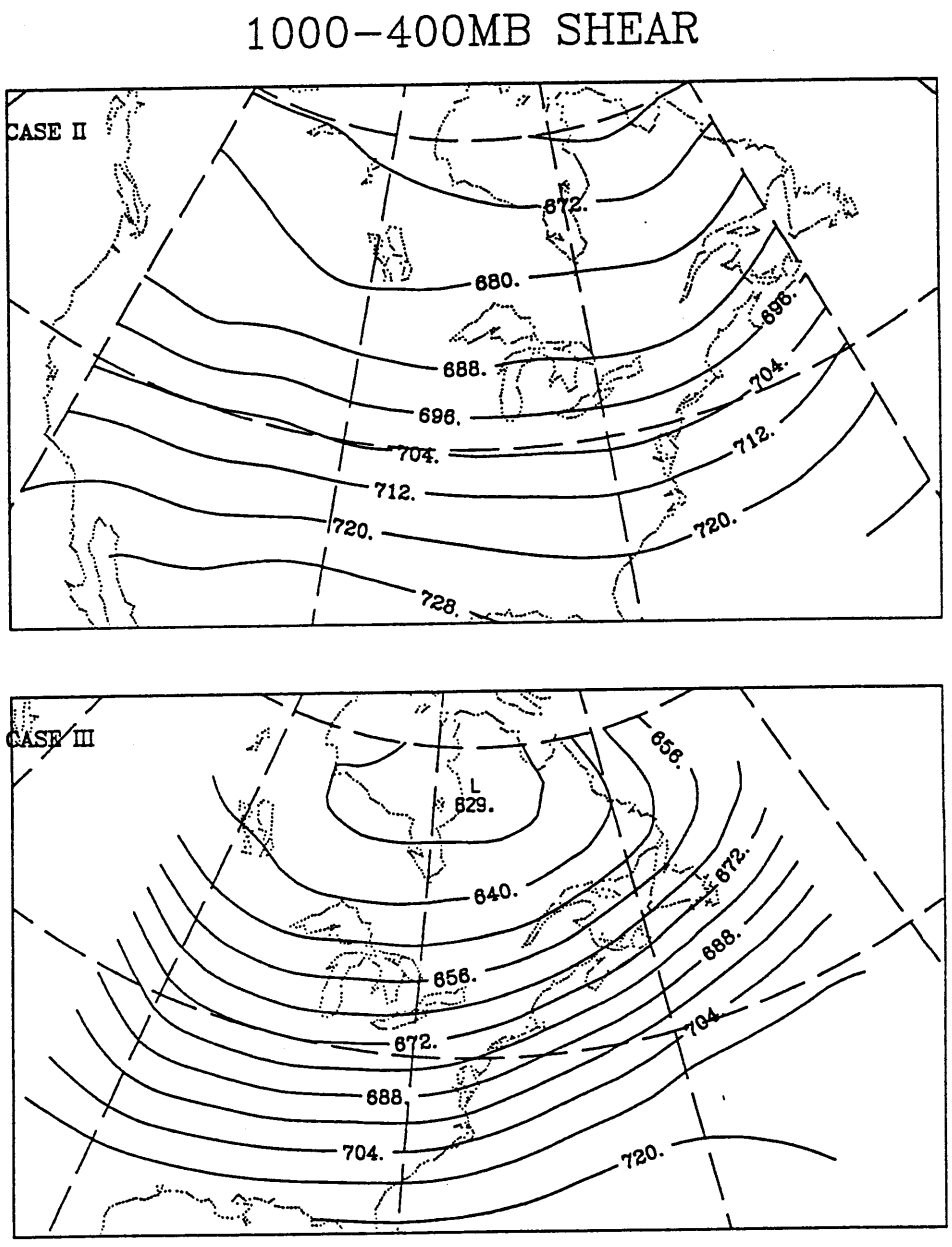


Figure 4.23 Difference between mean stream functions at 1000 and 400mb for (a) Case II, November, 1988; (b) Case III, February, 1988, defined at 12Z the 5th. Contour interval is 8, units have been scaled to appear as dm.

Case IV: December, 1987(b)

The final case we shall examine in this thesis occurred roughly two weeks after case I. Cases I and IV were very similar in the initial stages but in the latter event, strong cyclogenesis did not happen over the central United States. We will examine the possible reasons for this using the diagnostics already introduced. There was a rapid cyclogenesis event in connection with this case, but it took place off the East Coast of the United States. Both the lack of development over the continent and the explosive development offshore seem dependent on the phase relationship between perturbations at the same level but different latitudes that are initially isolated from each other. This case is more complicated than the others in that it is not adequately described in a quasi two-dimensional context and the disturbances are not as periodic in time.

We begin with figure 4.24 which shows the low level nondivergent winds and potential temperature for selected times during this event. At 00Z 26 December, there is a strong baroclinic zone over the southern United States which resembles the setting at 00Z 14 December (figure 3.1). In this case, the gradients of the lowest layer mean potential temperature are somewhat larger. We compare the surface conditions at 12Z the 14th (case I) and 12Z the 26th (case IV) in figure 4.25. Since the air at the surface is nearly saturated almost everywhere, we have plotted and analyzed values of θ_e^* at each station, which should be conserved following

the horizontal motion at the ground in the absense of radiative effects. As can be seen from the analysis at 12Z the 26th, cold advection in the lee of the Rockies is more extensive than in case I. In addition, there is cold advection to the east behind a front moving southeastward. Following this time in figure 4.24, we note a pronounced distortion of the thermal field, but there is little apparent increase of cyclonic circulation at low levels until the system moves offshore after 00Z the 29th.

At the tropopause, there are two major events to discuss. Figure 4.26 shows tropopause potential temperature and winds for the same times as in figure 4.24. We see a very high amplitude pattern initially, with a cutoff anomaly near 32N, 110W and a massive ridge covering most of western Canada. At least in this analysis, the feature to the south becomes progressively more cutoff from the flow. At low levels in the previous cases, the formation of such a cutoff was said to be the result of nonconservative (diabatic) processes. Here, however, the extent to which the feature is a "cutoff" may be partly a function of the data resolution. In high resolution numerical experiments (Juckes and McIntyre 1987), such vortex rollups are commonplace, and further, they are connected to the main polar vortex by thin filaments of high PV air. The implicit averaging imposed by examination with a coarser grid would make these features appear as distinct cutoffs, however. This could be true of low level isolated PV anomalies as well, but advection can usually be ruled out there given the isentropic winds, the surrounding PV, the time scale for the PV

anomaly to form and a plausible generation mechanism.

Between 00Z the 26th and 00Z the 28th, one sees the transformation of a shear line structure analogous to the one described by Holopanien and Rontu (1981) into an isolated vortex with a pronounced cyclonic circulation. Given the interpolations involved in producing isentropic and tropopause maps, we examine the cutoff formation using an alternative method for calculating PV. This method, described by Nielsen (1989), has the advantage of minimizing the interpolation of the raw data by mapping the winds and pressures to isentropic coordinates at each sounding location. This allows one to use data at all reported levels, not just the standard levels. For each sounding station, the "triangle" method of calculating PV proceeds by selecting the six nearest stations and forming six triangles from the total of seven soundings. The average PV for each triangle is the product of the average isentropic vorticity (integrating the circulation around the edge and dividing by the triangle area) and the average static stability (mean of the three stations). A constant layer thickness is used for the stability estimate (10K here). Since winds are assumed to vary linearly along the triangle edges, we placed an upper bound on the length of a single side at 2000km. To prevent overemphasis of a single observation, all angles were required to be larger than 15^0.

We present isentropic distributions of PV in figure 4.27 from both the triangle method and the interpolation method used previously in this work. At 00Z the 26th, the triangle method brings out the shear line structure somewhat better than the

interpolated PV. We have plotted the triangulated PV values at each centroid location, hence there are many more values than sounding stations (soundings located by +'s at the end of each wind barb). By 00Z the 27th, there is no sign of the high PV filament in either analysis. Although this doesn't prove its absence at some unresolvable scale, the integrated effect of such a feature is negligible. Note the east-west band of low PV air over the Great Lakes at 00Z the 27th. Values here are indistinguishable from those in the ridge to the west. Holopainen and Rontu point to dissipative processes as the demise of the shear line in their case, but we point out that this is not necessarily the true fate. The deformation that is acting to create the shear line is not independent of the shear line itself. In this case, as the scale of the PV ribbon decreases, its integrated effect on the flow becomes smaller relative to the effect of the main gradient to the north. Because the tropopause to the north in figure 4.27 is oriented nearly orthogonal to the shear line, this implies an increase of northwesterly flow with time acting to advect the line downstream.

The issue of whether the upper feature is cutoff or attached by an infinitesimal filament to the main gradient may be a rather moot point by 00Z the 27th, since the motion of the "cutoff" appears relatively uncorrelated to the behavior of disturbances in the northwesterly jet to the north. This situation is only temporary, however, as summarized by figures in the right column of figure 4.26. The trough has moved far enough eastward that a

new wave feature in the jet to the north has a substantially different interaction with it than preceding waves (figure 4.26c for instance). The amplitude of the northern wave is likely of considerable importance as well. The cutoff becomes elongated zonally as it encounters stronger westerlies on its leading edge. On the northwest side of the cutoff, large PV advection becomes apparent and the bulk of the feature moves rapidly southeastward. As we saw with case I, variations of the PV on scales much less than a deformation radius are not reflected by the balanced winds. The effect is particularly acute on the northwest side of the cutoff because the flow is also constrained to some extent by inertial stability. Isentropic absolute vorticities were found to be very nearly zero in this region. Thus the balanced winds flow at a considerable angle to the PV contours, which implies rapid advection of the back side of the cutoff downstream. As we shall see, the fact that these two initially isolated disturbances came into phase with each other had profound consequences at low levels.

A major difference, then, between the two December 1987 cases is that the large trough over the southwestern United States became a slow moving cutoff in this case, detached from the main PV gradient. In case I, the major upper disturbance was still embedded within the main gradient, implying that further amplification was possible. In case IV, the development over the Pacific was much stronger and on a larger zonal scale than that in figure 3.15. The difference in the amplitude of the ridge over

western Canada is quite evident and, once the enormous ridge is established in case IV, upstream waves are less likely to move onto the western coast of the United States. As we saw in case I, such upstream waves may have been significant for the downstream progression of the major upper feature.

For completeness, we present cross sections of the cutoff PV anomaly and potential temperature for selected times in figure 4.28. The amplitude of the tropopause undulation is comparable to that in case I, with stratospheric values of PV reaching down to 700mb by 00Z on the 29th. The eastward progression of the pattern is very slow, however, averaging less than $5ms^{-1}$ between 00Z the 26th and 00Z the 28th. Between 00Z the 29th and 30th, the period of "phasing" of the cutoff with the the trough in the westerlies, the eastward progression of this major trough has increased to about $15ms^{-1}$.

The question we wish to address now is why low level development of appreciable intensity did not occur over the central United States as in case I. Given the scenario of development in the earlier December case, we might expect the creation of a low level circulation in the frontal zone associated with a warm boundary anomaly. Yet from figure 4.24, we see only a weak low level cyclonic circulation until the system was off the East Coast.

The attempt to answer these questions is complicated by the probable inappropriateness of our working definition of a perturbation. However, there are three important issues that we can address without dealing with this problem explicitly. First is

the relative strength of the upper PV anomalies. In figure 4.29, we present cross sections of the meridional winds at 12Z the 14th and 12Z the 26th. At the tropopause, the momentum contributions from the low level PV and θ_B anomalies are typically small (figure 3.16 for example). Thus, given the remarkable similarity between the two fields presented and the similarities in the PV and θ cross sections, we would have to say that the positive upper PV anomalies have comparable strengths.

There are obvious differences in the velocity field at low levels however. This brings up the second issue, discussed briefly in Chapter 3, as to whether there are important differences in the penetration depths of these disturbances that account for the low level flow differences. One way to examine this possibility is to use the same PV perturbations as in case I, but with the environmental parameters (the coefficients in equation 2.6, Ψ^* and Φ^*) taken from the total fields of case IV. For the upper PV perturbations of 12Z the 14th, we compare (figure 4.30) the low level stream function whose winds are shown in figure 3.13 with that calculated using Ψ^* and Φ^* obtained from the total Ψ and Φ fields at 12Z the 26th. The same is done for the upper PV of 00Z 15 December where we compare the original field with the one using coefficients calculated from the balanced fields at 00Z the 28th. The upshot is that little difference is found in the low level flows, much less than if we had replaced the real coefficients by their layer averages for instance.

A third possibility is simply that the possible warm advection

at the lower boundary is being cancelled by other perturbations. Tendency calculations are useful here. Figures 4.31 and 4.32 were obtained from inverting the tendencies of θ_B, PV at 850mb and PV aloft separately. The tendencies were obtained as before from the PBE's with the effects of condensation included. In figure 4.31, we see that the height falls implied by the potential temperature tendency at 12Z 14 December far exceed those at 12Z the 26th. The significant difference appears associated with a system moving through the northeastern U.S. Other items to note are (a) the partial cancellation of the θ_B tendency from the tendency of low level PV and (b) the signature of upper PV advection at 12Z the 26th which roughly cancels the tendencies from the potential temperature field. A similar story is made evident by comparing the tendencies at 00Z the 15th and 00Z the 28th (figure 4.32), although it is a different system passing through the northeast at this time. There is a net low level cooling over the northeastern U.S. after 00Z the 26th as represented by these tendency plots and figure 4.24. Hence, there is an inhibiting factor for the development of a surface warm anomaly ahead of the upper level PV maximum.

In contrast, the explosive development off the East Coast is an example of reinforcement rather than cancellation. To examine this in more detail, we wish to calculate how the low level circulation associated with the upper PV behaved as this reinforcement occurred. The perturbation will be taken as the difference between two times. For a wavelike feature the interval

(Δt) most appropriate would correspond to the the time it takes the wave to travel 1/4 of a wavelength. Then the amplitude of the perturbation defined this way would match the true amplitude (although the spatial pattern would be somewhat different). However, the features discussed here do not appear to have much of a wavelike quality. In the case of a disturbance developing from a very small initial perturbation, the time scale for the development suggests itself as one choice for an appropriate time interval. Then the perturbation is approximately the total development.

In the present case, we have large amplitude features that develop into larger ones, so that the latter definition is not ideal. The definition we will use for Δt is the time it takes for a feature to move a distance comparable to its "scale" in the direction of motion. For a circular cutoff on an isentropic surface, this would be its radius. In general, Δt will vary from one time to the next as perturbations change their speed or shape. For the present example, we take Δt=24 hours to define perturbations at 00Z the 29th and Δt =12 hours for 12Z the 29th and 00Z 30 December.

The amplification of the PV features aloft (figure 4.26) was not influenced to any degree by low level perturbations of PV or θ. If we subtract the winds associated with these lower anomalies from the total flow, the results (not shown) are almost indistinguishable from the figures in the right column of figure 4.26. However, the signature of the amplifying upper level trough is quite evident at low levels in figure 4.33, with southerly winds in phase with the growing warm anomaly. This pattern has been

seen in each case examined so far. The present development shares a qualitative similarity with the cyclogenesis over the U.S. in case I in that amplification at upper levels was relatively independent of the lower tropospheric anomalies.

The flow associated with the lower PV and potential temperature perturbations is quite strong as well. Relative vorticities near the warm anomaly approach twice the Coriolis parameter at this level. The detailed structure of this cyclone is, of course uncertain owing to the lack of observations in this region. The analyses used here are mostly a product of the first guess field (i.e. the 12 hour NMC spectral model forecasts, see Chapter 2). Thus many of the important features evident in the analyses at 00Z the 30th were themselves the product of a previous model forecast. We are somewhat fortunate that the westward tilt with height of the system allows part of the crucial upper level features to be captured by the rawinsonde data. However, further investigation of the possible importance of low level interior PV anomalies as well as the role of boundary layer processes will not be undertaken here.

To summarize, the major differences between cases I and IV appeared to hinge on whether the large amplitude PV pattern over the western United States became cutoff from the basic gradient of potential vorticity. The utility of potential vorticity was shown here, because it allowed us to assess whether systems were "cutoff" in a meaningful way. It also gave a clearer picture of the process by which the upper vortex formed as well as how two

initially separate PV features could reinforce each other. The latter was likely crucial to the rapid low level development off the East Coast of the United States.

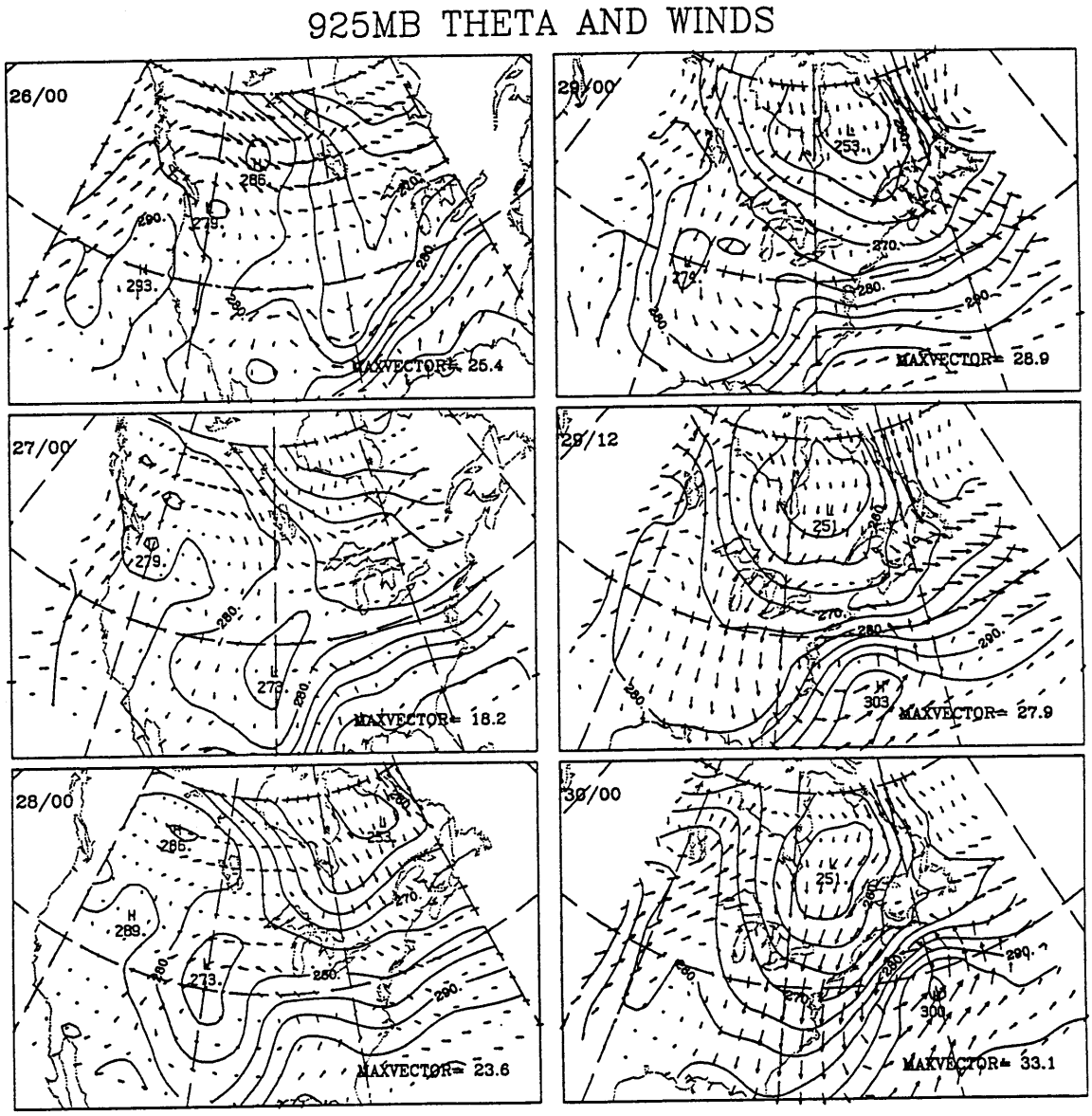


Figure 4.24 Balanced nondivergent winds at 925mb and lower boundary potential temperature (contour interval 5K). (a) 00Z 26; (b) 00Z 27; (c) 00Z 28; (d) 00Z 29; (e) 12Z 29; (f) 00Z 30. Latitude line nearest center of all plots is 40N. Central longitudes are (a) 110W (b) 100W (c) 90W (d) 80W (e) 75W (f) 75W.

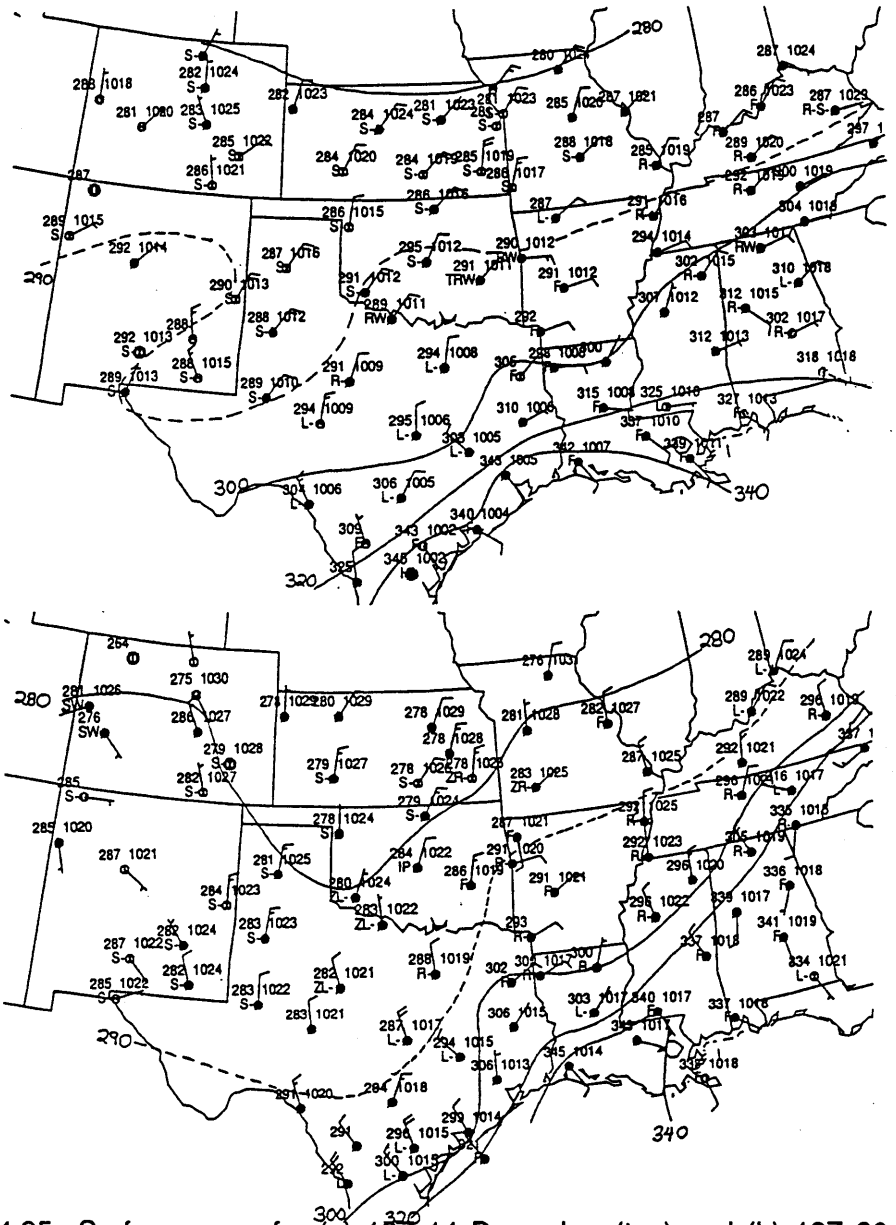


Figure 4.25 Surface maps for (a) 12Z 14 December (top) and (b) 12Z 26 December (bottom). Each station location is marked by a circle. Blackened circle indicates overcast conditions; 'x' means sky is obscured. At each station, number at upper left is saturation θ_e (K), at upper right is sea level pressure and middle left character denotes weather type; F=fog, R=rain, S=snow, L=drizzle; T prefix signifies thunder; W suffix denotes shower; + indicates heavy intensity, - is light intensity and no sign implies moderate. Wind barbs in knots (long barb=10 knots, short barb=5 knots). Contour interval for θ_e^* is 20K; dashed contour is 290K.

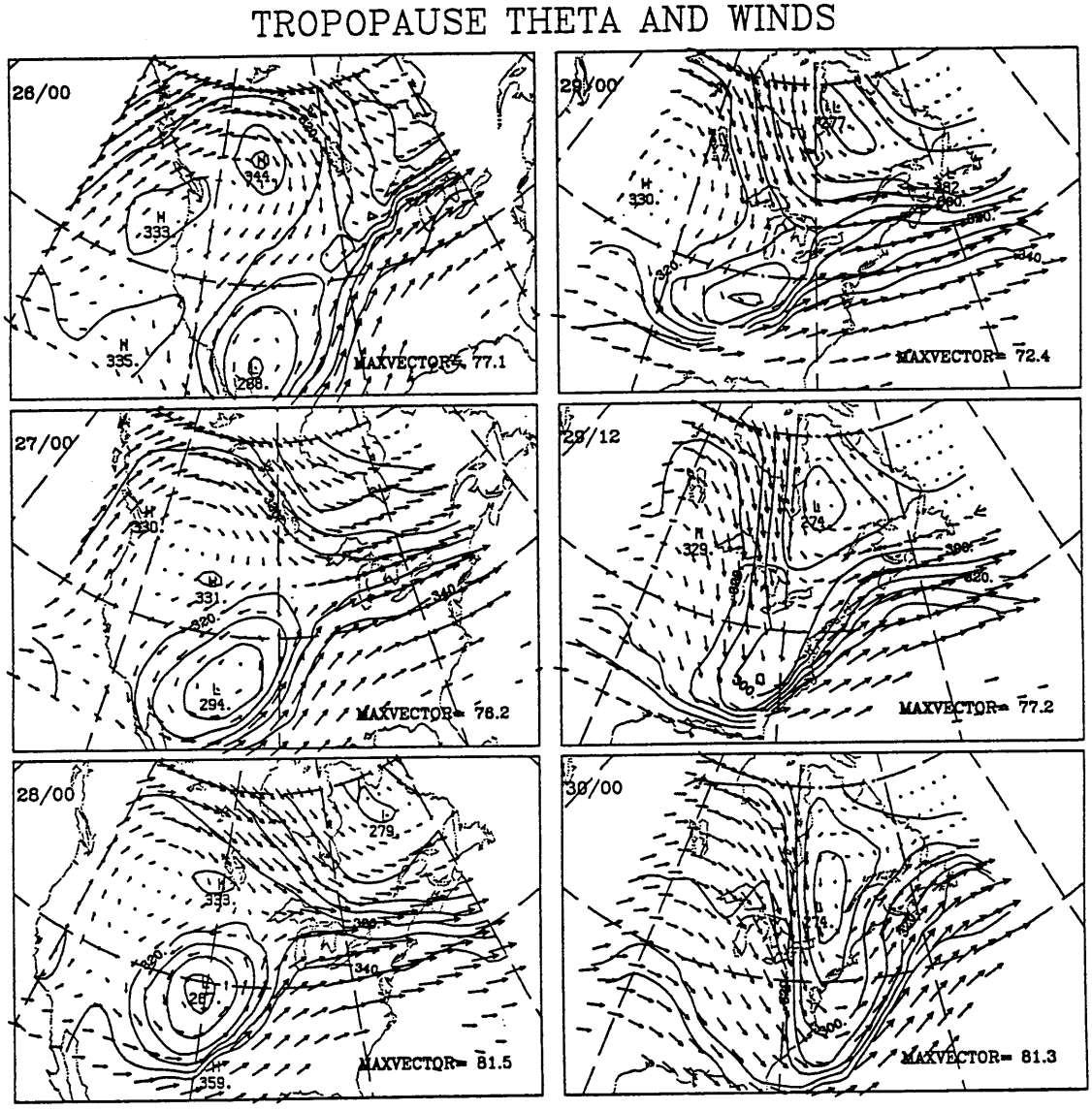


Figure 4.26 Tropopause winds and potential temperature (contour interval is 10K, max contour at 340K). Times and map orientations as in figure 4.24. Wind vector lengths scaled down by a factor of two relative to figure 4.24.

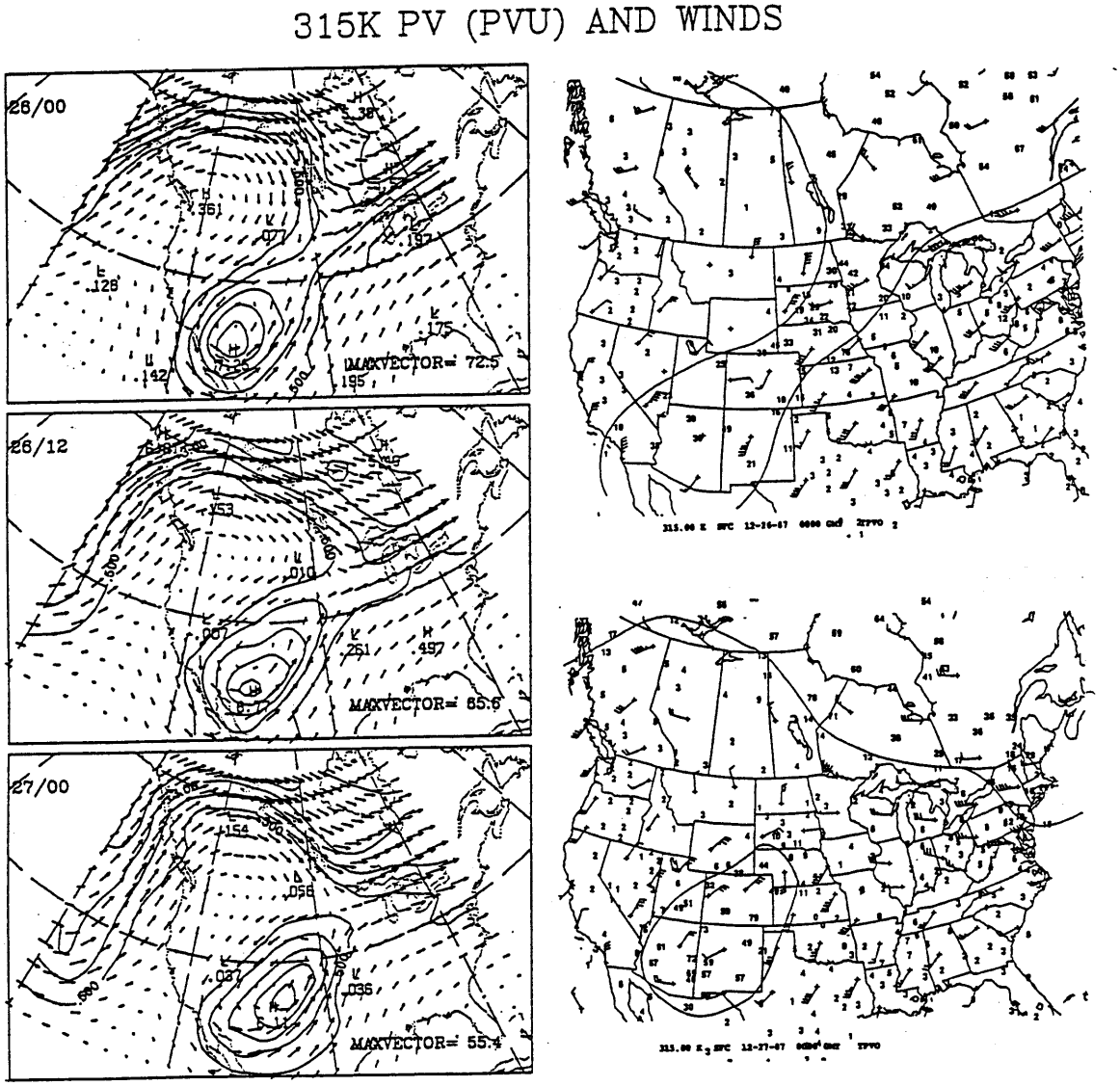


Figure 4.27 315K PV and winds. Left column. (a) 00Z 26; (b) 12Z 26; (c) 00Z 27. PV contours at 0.5PVU and at intervals of 1.5 PVU for values of 1.5 PVU and larger. Right column; triangulated potential vorticity (see text for details) (d) 00Z 26 and (e) 00Z 27. Plotted numbers are values of PV (tenths of PVU) at triangle centroid locations. Winds are station winds interpolated to the 315 surface (station locations marked by the '+'); barbs in ms^{-1} (pennant is 50, long barb is 10, short barb is 5). In (d) and (e) the tropopause (1.5PVU) appears as a solid line.

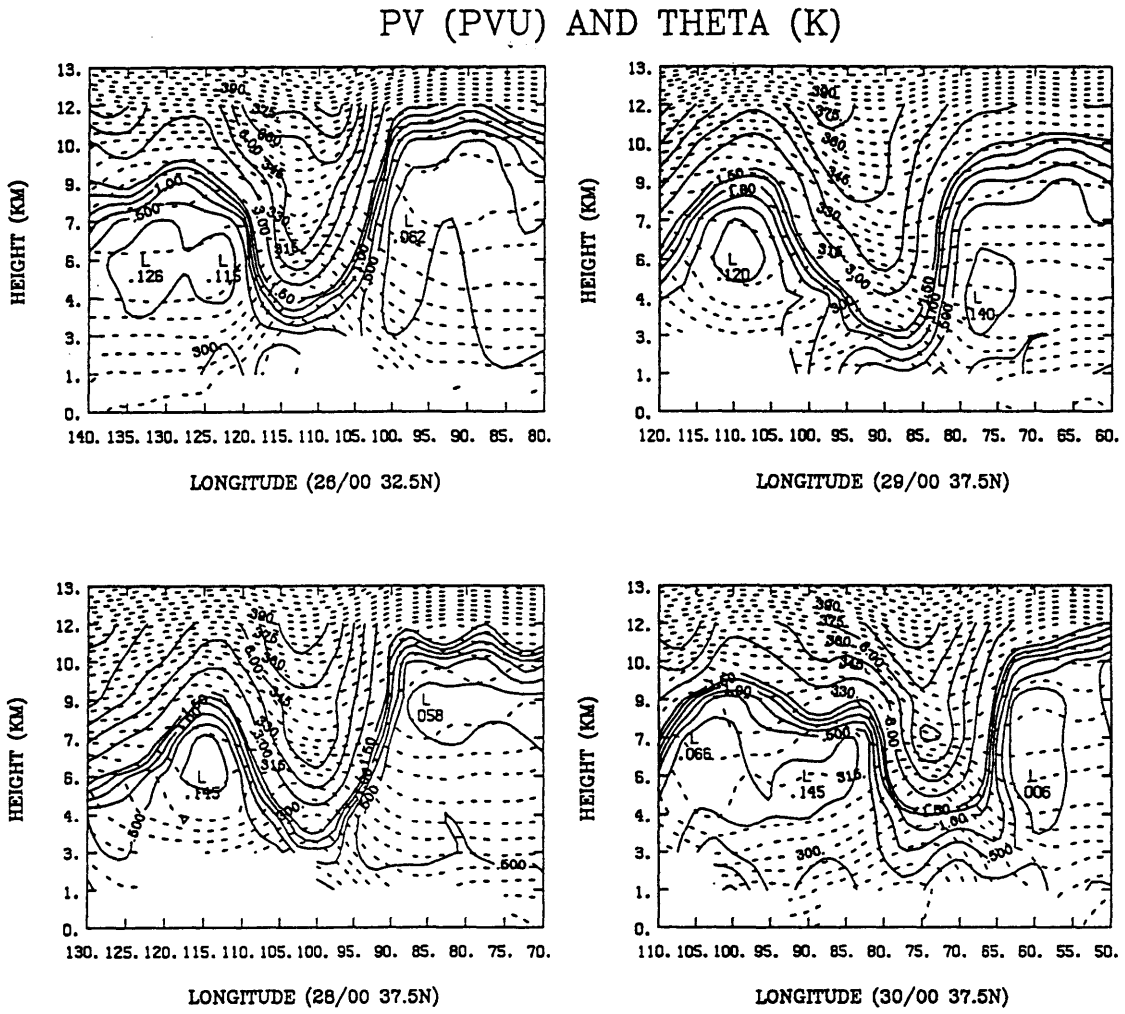


Figure 4.28 Cross sections of PV (PVU, solid) and potential temperature (K, dashed). Plotting conventions as in figure 4.2; (a) 00Z 26, 32.5N; (b) 00Z 28, 37.5N; (c) 00Z 29, 37.5N; (d) 00Z 30, 37.5N.

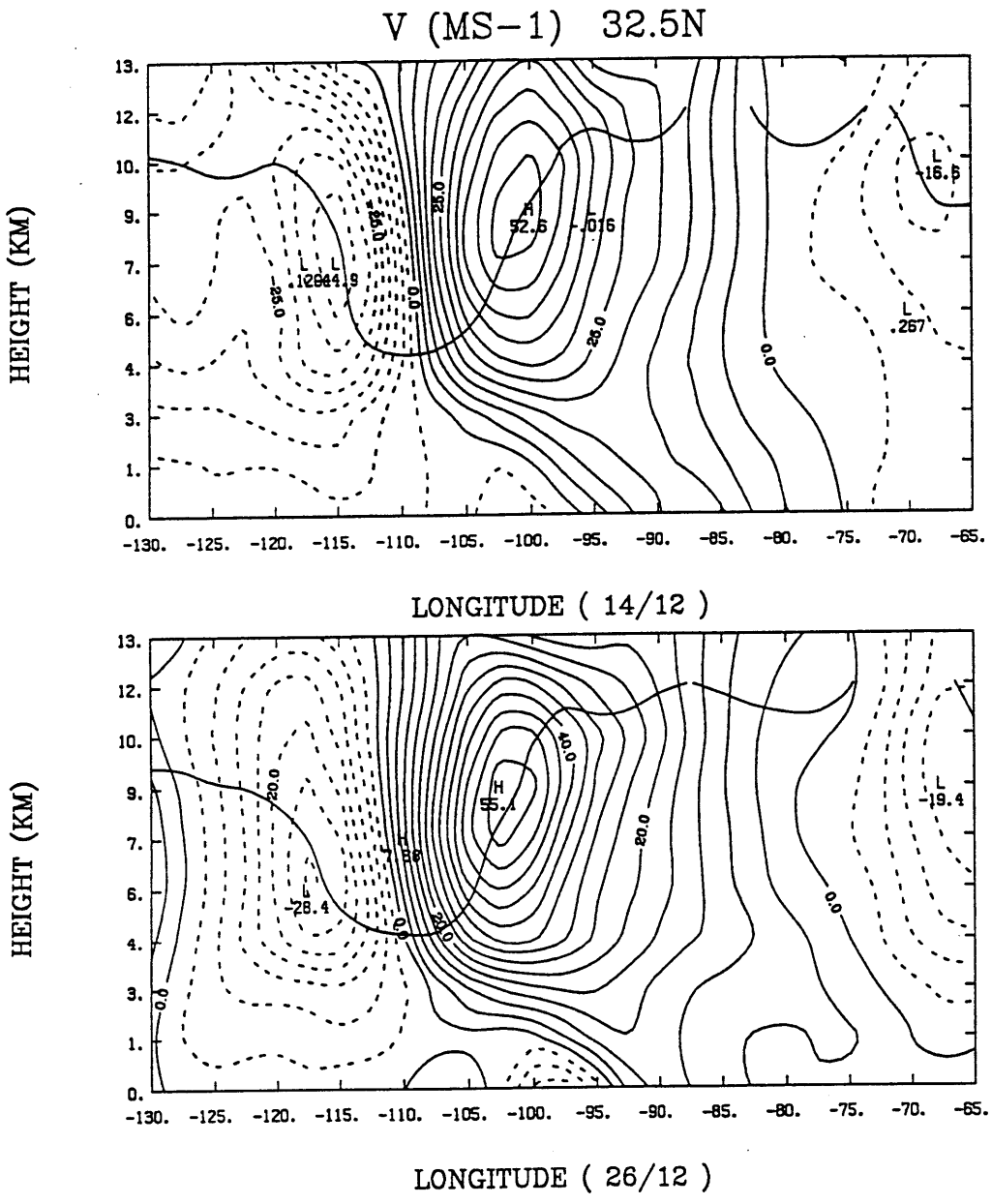


Figure 4.29 Cross sections of balanced meridional wind along 32.5N (contour interval 5 ms^{-1}, negative contours appear dashed). (a) 12Z 14 December (top); (b) 12Z 26 December (bottom). Height refers to "pseudo-height" as in other cross sections. 1.5 PVU contour has also been plotted on each cross section.

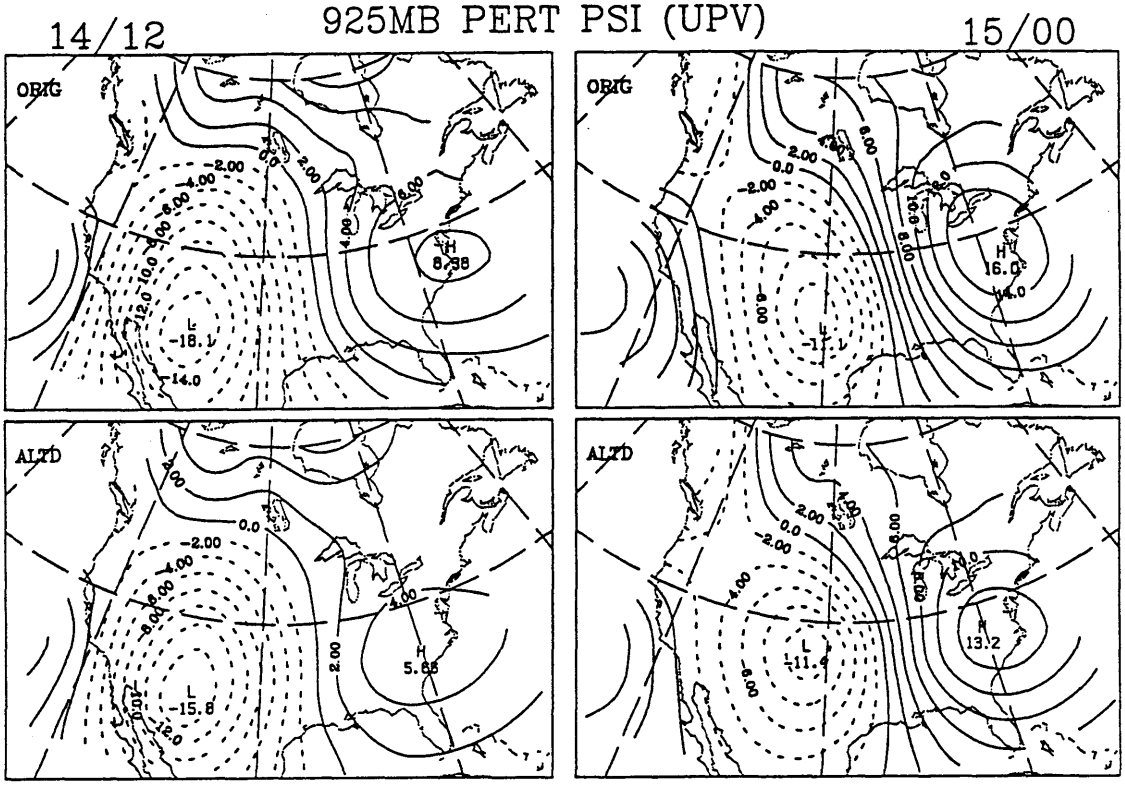


Figure 4.30 Perturbation stream function at 925 mb associated with upper PV anomalies in case I. Left column is for 12Z the 14th. (a) original calculation (b) calculated using coefficients computed from the balanced fields at 12Z 26 December in the differential equation. Right column is for 00Z 15 December. (c) original calculation (d) modified with coefficients from 00Z 28 December.

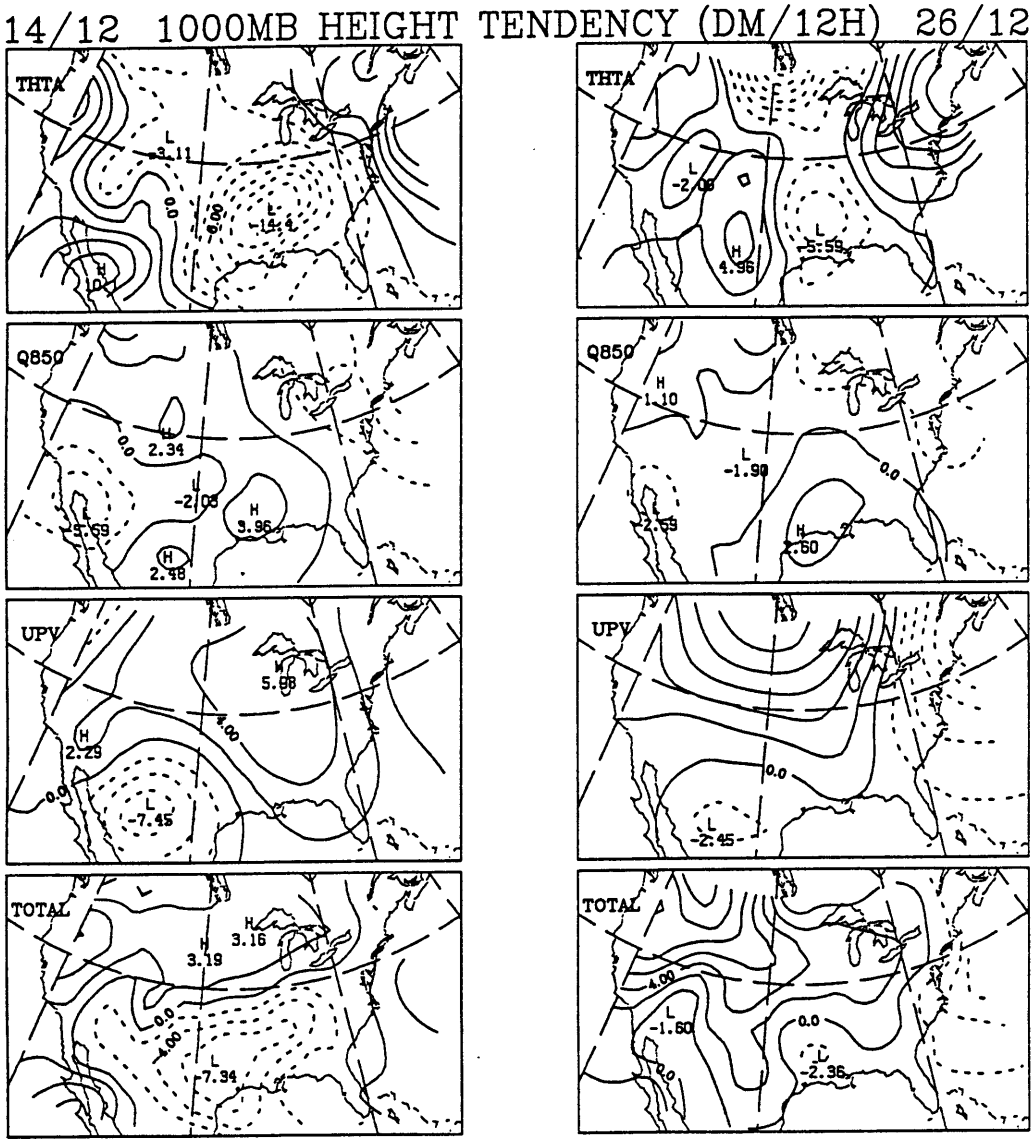


Figure 4.31 Geopotential height tendencies at 1000mb for 12Z 14 December (left column) and 12Z 26 December (right column). Contour interval is 2 dm/12hrs, negative contours dashed. (a) and (e) tendency from lower boundary θ tendency; (b) and (f) from 850mb PV tendency; (c) and (g) from upper PV tendency; (d) and (h) show the total tendency field for each time.

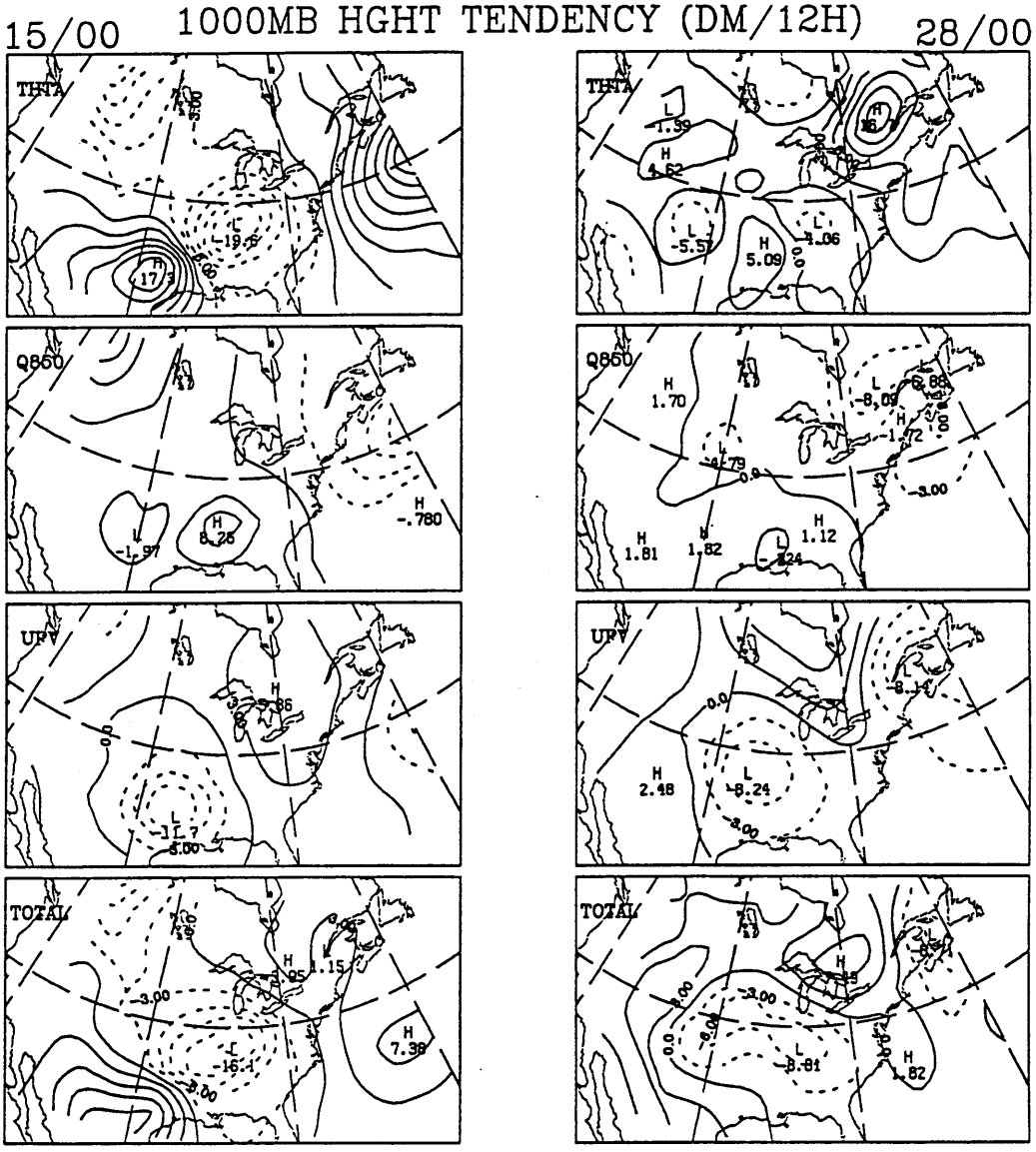


Figure 4.32 As in 4.31 but for 00Z 15 December (left column) and 00Z 28 December (right column).

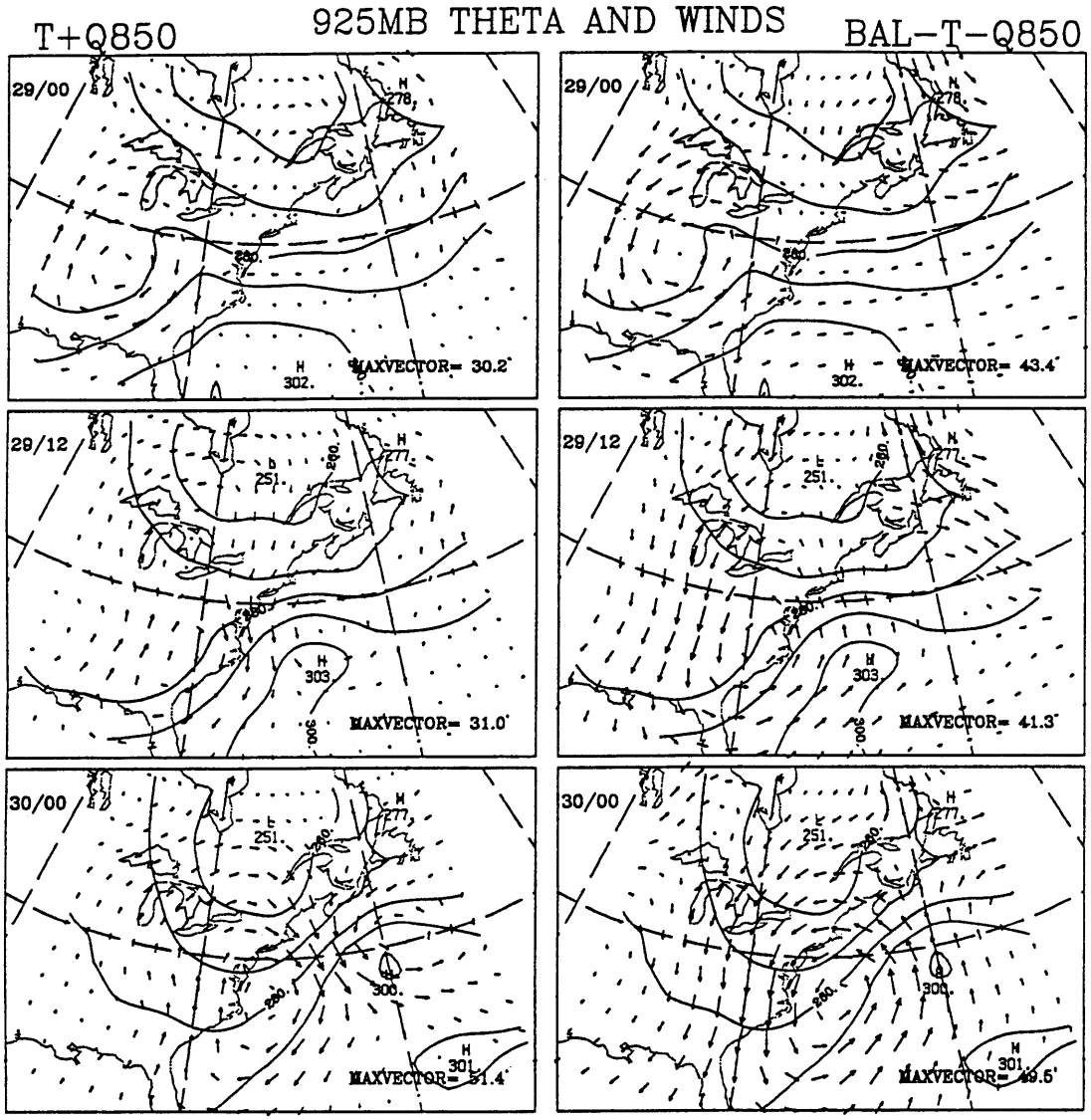


Figure 4.33 Winds at 925 mb and lower boundary θ (contour interval 10K). Left column shows the wind vectors from the perturbations of θ_B and PV at 850mb for (a) 00Z 29; (b) 12Z 29 and (c) 00Z 30 December. Right column shows the remainder of the balanced wind fields at that level for (d) 00Z 29; (e) 12Z 29 and (f) 00Z the 30th.

Chapter 5: Summary and Discussion

Summary of cases

The recurring themes in the four cases we have examined can be summarized as follows. First, in the early stages of development, the total low level total cyclonic circulation was mostly associated with perturbations of potential temperature at the lower boundary. Second, the amplification of the boundary thermal wave was primarily related to the low level circulation associated with anomalies of potential vorticity in the upper troposphere, both in developments of transient and more phased locked vertical structures. Third, the effect of moisture could be seen from the generation of positive low level potential vorticity features nearly in phase with the surface warm anomaly. The winds associated with such features made substantial contributions to the cyclone intensity in two cases (roughly 1/3 total circulation). These anomalies were found just upshear of (and partially overlapping) the region of largest PV generation from condensation in stably stratified ascent. "Stably stratified ascent" does not imply weak vertical motions; indeed, vertical velocities of 15-20 cms^{-1} were calculated in the updraft regions of the more intense cases. This suggests a small effective stability for ascending air in these systems as emphasized by Emanuel (1988).

Two of these cases, both from December, 1987 seemed governed by the initial presence of large amplitude PV features in the upper troposphere. A strong distinction in the evolution of these two cases existed, however. In the first December cyclone (case I), the large amplitude upper tropospheric disturbance was still embedded within the main isentropic gradient of PV (tropopause gradient of potential temperature). The significant PV feature in the second case of December, 1987 was physically cutoff from the basic gradient of PV to the north. In case I, the fact that an ambient tropopause gradient existed allowed two important things to happen. One was the impinging of an upstream shortwave feature on the major trough, which we saw in Chapter 3 was perhaps responsible for its rapid advection downstream. The other important event at upper levels was the amplification of the downstream negative PV anomaly. As we saw in Chapter 3, the combination of this amplification along with the physical lowering of the tropopause in the positive PV anomaly (probably from condensation) was significant for the intensification of the low level circulation. The southerly flow acting to amplify the positive phase of the thermal wave was strengthened at the same time that superposition of the positive vorticity signatures of both the upper and lower anomalies occurred. Much of the ridge amplification was due to simple advection, but our analysis indicated that the "wrap up" phase of this development may have been diabatically enhanced.

In case IV, the initial large amplitude feature became cutoff

from the main gradient of PV at the tropopause. Subsequent events were quite different from case I because (a) no further development of the upper level feature was possible (at least from conservative dynamics) (b) disturbances in the detached northwesterly jet to the north were, on average, cancelling the development of a warm boundary perturbation to the east of the cutoff and (c) even if such a low level disturbance did exist, the slow eastward progression of the upper vortex was unfavorable for rapid growth from superposition effects. At a later time, the "phase" relation between this vortex and a disturbance in the jet to the north became favorable for reinforcement rather than cancellation. Rapid cyclogenesis then occurred in a development scenario similar to case I. The low level spinup was related to the amplification of a boundary themal wave, which was strongly influenced by the low level circulation of the upper PV. The offshore development was more intense than that of case I, though we have not considered the modifications to the basic baroclinic development theme presented here that may have made it so.

The character of the major developments in both cases I and IV is that of the robust cyclogenesis events described by Petterssen (1955). The coupling between the tropopause and low levels is "one way" in each example, meaning that the circulation from the low level PV and boundary potential temperature anomalies was likely unimportant in the upper level amplification. These developments seem most consistent with the works of Farrell (1984) and Rotunno and Fantini (1989). Both works were concerned with the

initial value problem of cyclogenesis; Farrell examined growth of initial disturbances where the continuous spectrum of neutral modes was involved while Rotunno and Fantini considered initial disturbances composed only of a combination of the two neutral Eady edge waves. In our cases, the amplitude of the upper level perturbation is initially much larger than that of the lower.

Especially for case I, it is possible to think of the cyclogenesis as transient growth with an Eady type configuration in the potential vorticity distribution. That is, if we identify the tropopause as the upper "boundary", the behavior can be summarized as the amplification a thermal wave at the lower boundary via the low level flow associated with an upper boundary potential temperature anomaly. This is essentially the picture put forth in HMR (section 6e) except that in these two examples, the circulation related to the lower boundary potential temperature perturbation does not play much of a role in the amplification of the PV aloft. Also, there is not a simple "overtaking" of the low level θ perturbation by the upper level anomaly and subsequent passage downstream as envisaged in the theoretical initial value problem. There is a partial superposition of the two features, but then the upper PV pattern begins to wrap up, slowing its downstream progression. In addition, the eastward phase speed of the lower boundary thermal wave increases, perhaps in response to a large scale enhancement of the low level thermal gradient downstream. The result is that the previously favorable phase relation between the upper and lower anomalies is once again

established, and some baroclinic growth occurs again. However, as seen from the magnitude of the vorticity perturbations associated with the lower thermal anomaly, most of this "secondary" cyclogenesis is only "apparent" development. It results from the physical separation of the upper and lower anomalies (and the fact that the negative vorticity signature of the upper PV is weaker than the positive signature at low levels).

The other two cases (cases II and III in Chapter IV) featured a more evenly partitioned importance of upper and lower level interior PV perturbations in the development as well as a less transient phase structure. At the early stages in each case, there was evidence that potential vorticity perturbations near 850 and 700mb had some role in the amplification of the low level thermal field. The bulk of the development in each case occurred when the circulation associated with the tropopause waves became large enough to aid in the amplification of the low level thermal wave. During this stage of development, most of the initial transience in the phase structure ceased.

In only one of these cases was the majority of the amplification at upper levels consistent with the advection of upper PV by the circulation associated with the low level PV and θ perturbations (case III). In case II, the reason for the upper level amplification is not totally clear. We saw that the circulation from the lower tropospheric anomalies was properly configured to amplify the positive phase of the upper PV wave. In the calculation of the heat flux at the tropopause, however, this flow had a

secondary effect to that of the flow associated with the upper PV distribution.

This may not tell the whole story because at any given time, the flow associated with the upper PV pattern depends somewhat on the previous effect of the low level anomalies. We saw an example of this at low levels in case I. The positive thermal anomaly appeared to be growing in association with the flow from the upper PV. However, the cold phase of the thermal wave seemed to grow in response to the circulation associated with the positive θ perturbation. We should bear this in mind when considering the evolution of the tropopause perturbation in these cases.

In both cases II and III, the important low level PV anomalies likely arose through condensation. In the early stages of case III, there was evidence that such a feature helped amplify the thermal wave. The fact that later growth of this perturbation took place in phase with the warm thermal anomaly meant that it reinforced its circulation. Especially for case III, this increased the strength of the advection of tropopause potential temperature and the amplification of the upper level anomaly. Thus, the primary effect of moisture may be viewed as effectively enhancing the strength of the lower boundary warm anomaly (leaving the cold phase of the wave unchanged).

Discussion

A basic point of the above analyses is the significance of the

tropopause based upper PV disturbances in amplifying perturbations of potential temperature at the lower boundary. We did find that low level PV anomalies (usually with maximum amplitude somewhat below the steering level) were quite important in some developments, however, these were probably created by diabatic processes rather than advection. Thus, at least in the main stages of development, we do not find a significant role for PV perturbations of advective origin near the steering level.

We cannot rule out the existence of very small steering level PV features of conservative origin in the early stages of development. Our data is perhaps inadequate to detect them, however. It may be instructive to examine the "basic state" PV distrubution to see whether there are interior gradients of PV in addition to those at the tropopause. The existence of mean isentropic PV gradients would at least be consistent with the possibility of critical level instability. Figure 5.1 shows cross sections of PV and potential temperature (a-d) and zonal wind (e-h) averaged over a wavelength of the case II disturbance (November, 1988). The averaging domains used were identical to those for figure 4.8 (at 00Z the 11th, we averaged from 90W to 50W). Recall that the perturbation was centered near 40N at the early times and the main circulation of the cyclone was close to 45N by 00Z the 11th. We do see a systematic gradient of PV in the region of large vertical shear, although this variation is not much larger than inherent errors in calculating PV. For reference, the β

term would yield a gradient of about 0.1PVU for every 10° latitude (computed from $q_y=g\beta\theta_p$ with θ_p being a typical tropospheric static stability of $5x10^{-4}K\ PA^{-1}$).

Theoretically, (Green 1960, Bretherton 1966b), this acts to destabilize the short waves in the traditional Eady problem and deemphasizes the disturbance at the upper boundary. In addition to this, at 00Z the 9th, a low level PV anomaly shows up in the average, embedded within a baroclinic zone near 37N (maximum value is a bit larger than 0.5 PVU). Being an extremum on an isentropic surface (dashed lines) this satisfies the necessary condition for instability as well. Hence, the classical necessary conditions for linear instability are certainly met in this case given the interior tropospheric distribution of PV and the gradients of potential temperature at the lower boundary.

Of course, there is also the large (isentropic) gradient of PV at the tropopause or, viewed another way, a gradient of potential temperature on a constant PV surface. It is interesting to note that the tropopause gradient is eliminated between 42 and 52N by 00Z on the 11th. This is related to the amplifying upper level disturbance. The gradient of potential temperature at low levels is somewhat reduced, but not eliminated (this is also true for lower boundary potential temperature). Note that the small gradient of PV in the interior is still identifiable and has not been erased.

Since the results in this thesis indicate the interaction between disturbances at the tropopause and the lower boundary

dominates in these cyclogenesis cases, it suggests that much of the dynamics can succinctly be viewed in terms of maps of tropopause and lower boundary potential temperature. This is an analogue for the Eady model applied to the real atmosphere where the upper boundary is now a deformable material surface. (material as long as PV is conserved). The existence of lower tropospheric PV anomalies, principally generated through condensation, is a complication to this picture. We now present a means of approximately incorporating these features into the distribution of lower boundary potential temperature.

We can write the finite difference form of PV (somewhat schematically) as

$$q = -G\,(\,\eta\,(\theta_{k+1/2} - \theta_{k-1/2}\,)/\Delta_\pi - S\,) \qquad (5.1)$$

where $G = g\kappa\pi/p$, η is the absolute vorticity, $\Delta_\pi = (\pi_{k+1} - \pi_{k-1})/2$, k is the index for the vertical level and S is the finite difference equivalent of the last two terms in eq. 2.1. With S and η given from the balanced flow fields, we now calculate the $\theta_{k-1/2}$ necessary for q to be uniform in the lowest layer

$$\theta_{k-1/2} = \theta_{k+1/2} + (\Delta_\pi/\eta)(\,S + [q]/G\,) \qquad (5.2)$$

where [q] is now the layer average value of PV. We set $\theta_{k+1/2}$ equal to its observed value as well. This is the same as specifying all of the potential vorticity above layer 'k' (the lowest in the domain) to be equal to its observed value. The modified lower boundary potential temperature, θ_{B^*}, approximately incorporates the distribution of PV in the lowest layer. We could do a similar

calculation with quasigeostrophic PV, only there, the resulting modified potential temperature is conserved following the horizontal motion at the lower boundary (assuming the layer mean flow is also the flow at the lower boundary). This is really nothing more than reexpressing Bretherton's ideas of the equivalence between potential temperature at the lower boundary and a δ-function of PV just above the boundary. The quantity θ_B* obtained from Ertel's PV is only approximately conserved following the horizontal motion at the lower boundary. Nevertheless, we shall present some of examples which point out its usefullness.

One point, that was remarked upon briefly in Chapter 4 (related to figures 4.31 and 4.32) was the partial cancellation of the effects of low level PV and θ_B tendencies on the surface pressure field. Figure 5.2 develops that point further by showing PV at 850mb and θ_B for one time selected from the early stages of development in each case. There tends to be high PV on the cold side of the surface front, likely of nonconservative origin, be it condensation, as the results of Thorpe and Emanuel (1985) suggest, radiation, or surface friction (where the relative vorticity is anticyclonic). If one imposes a cross frontal flow, such as from an upper PV disturbance, the gradients of the PV and potential temperature are such that the effects of the tendencies of these two quantities on the pressure field will tend to cancel. There is no reason to believe that cancellation should be complete, but it does complicate the simple picture of the interaction of disturbances at the tropopause and lower boundary.

We now show figure 5.3, in which we have plotted θ_{B^*} and the balanced nondivergent winds at 925mb. From this, a further point can be made concerning the differences between cases I and IV. The effective potential temperature gradient in case IV is nearly zero in the frontal region. Hence, although the front may deform by advection, there would be little tendency for an increase of vorticity. This adds another reason to the list of why little development took place in case IV given a situation resembling the favorable conditions of case I.

A further point involves the generation of low level PV anomalies during development. As we have seen, the primary effect of these features was to enhance the strength of the lower boundary θ anomaly. We can see this from figure 5.4 which shows the mature cyclone of case III at 12Z 05 February, 1988. We have presented the θ_B and θ_{B^*} fields to emphasize the possible magnitude of the effective enhancement associated with low level PV anomalies. Winds associated with the potential temperature perturbations alone as well as the flow from θ_B and 850mb PV anomalies together are plotted. We obtained the latter from inverting the observed 850mb PV, not by inverting the modified potential temperature directly. Owing to the depth of the positive PV anomaly (figure 4.13d), we are not able to recast all of it in terms of $\theta_B{}^*$. However, the maximum in potential vorticity generated by condensation in stable ascent usually occurs very close to the ground, as it does here. Thus, this modification is able

to account for the bulk of the low level PV anomaly.

The view of development presented in the context of disturbances of potential temperature at the tropopause and the lower boundary appears to be a succinct and dynamically meaningful way of describing the cyclones studied in this thesis. We reiterate that our analogy with Eady "type" development is only in the conceptual sense, since we do not wish to imply that the Eady *model* provides a detailed, quantitatively correct description of the cyclones we have studied. The simplicity of viewing developments in this context is appealing; though more examples, perhaps concentrating on the initial stages of growth, or the growth of weaker cyclones as well as cases in different geographical regions are needed to establish the degree to which this view is representative of cyclogenesis in general.

Further Calculations

The work by Thorpe (1986) was significant in that his calculations of the balanced flow associated with isolated PV anomalies required only the specification of potential temperature at the ground and the tropopause (and at the top of the stratosphere, where θ had no horizontal variation). One question that arises is how much of the total (balanced) flow in the real

atmosphere can be obtained from only these two boundary conditions. For the cyclones we have examined, we have suggested that much of the important dynamics may be viewed this way, but what about for other situations and phenomena on other scales? Also, what about the real lower boundary for the atmosphere? In this work we have really avoided the issue, but in fact, potential temperature is conserved following the horizontal motion on the topographic lower boundary. In addition, the balance condition used by Thorpe was quite accurate, but restricted to perturbations with circular symmetry. How could a more general balance condition, such as the one we have used, be adapted to the geometry of this two surface problem (such that it would be appropriate for inverting Ertel's PV)?

Techniques for inverting Ertel's potential vorticity may also have use in the field of numerical weather prediction. First of all, one of the goals of model initialization is to remove the majority of the high frequency oscillations at the start of numerical integration, namely sound waves and gravity modes. This is accomplished by fiat through the inversion of potential vorticity. The accuracy of our technique for inverting an approximate form of Ertel's PV suggests that potential vorticity should be the focus of the data analysis scheme. The first guess field could simply be the PV, with observations used to modify it appropriately. The initialization process would consist of inverting this field, the divergent and vertical velocities being obtained from the balance equations. One would need to perform all these calculations in the

vertical coordinate system of the model to avoid inconsistencies due to the vertical interpolation of balanced fields.

Another question is what determines the location of diabatically generated PV anomalies with respect to the other PV (and θ_B) features in baroclinic developments. The region north of the warm front, just downshear from the cyclone center, is often where the heaviest stratiform precipitation occurs. We observe the diabatically produced potential vorticity to lie on the upshear edge of this region, close to the positive θ_B anomaly. This is consistent with two dimensional simulations of moist baroclinic waves in which the maximum PV generation occurs below the steering level. However, results from case I indicated that the diabatic generation enhanced anomalies upshear of the positive phase of the thermal wave as well as in the frontal region. In this case, the precipitation shield was wrapped around the north and northwest side of the surface cyclone as the storm relative flow was easterly through a very deep layer by 12Z 15 December. The initial intensity of the upper level PV disturbance probably had a great deal to do with this precipitation distribution. This case serves to illustrate the need for modelling moist baroclinic waves in three dimensions.

Other issues still remain concerning the effects of latent heat release on cyclones. One question is why the low level PV anomalies seem to develop very suddenly, even though precipitation rates in cyclones may not vary significantly during their growth phase. This was particularly important in case III, where the

explosive development was substantially enhanced by the rapid generation of a low level PV anomaly. The dependence of the PV generation rate on the absolute vorticity (eq 1.3b) may be crucial here.

Detailed parcel trajectories are likely necessary to adequately address the issue of PV generation and its influence on cyclone development. In addition, such trajectories would be helpful in quantifying the role of diabatic processes in the wrap up of the upper PV in case I. The most plausible source of realistic trajectories is numerical simulations of cyclogenesis. Here, potential vorticity may have a significant use in diagnosing the performance of models, a necessary first step if model output is to be relied upon. This includes utilizing the integral as well as differential theorems regarding the conservation of PV.

There are other issues which deal with processes we have not considered. It has been remarked (Shapiro 1976) that turbulent processes near the jet may contribute to the "generation" of potential vorticity on scales resolved by observations. There are also effects from turbulence in the boundary layer that can destroy potential vorticity. Evaporation of precipitation has also not been considered in this study.

Without question, there is a great deal more to investigate concerning the cyclone problem for which the potential vorticity approach may prove useful. However, one should excercise caution in applying PV diagnositics to all phenomena on the synoptic and planetary scales since alternative approaches may yield insights in

a simpler way. We feel that this thesis has provided a useful framework for the further study of the cyclone problem and more generally, has encouraged practical and rational applications of "PV thinking" to the real atmosphere.

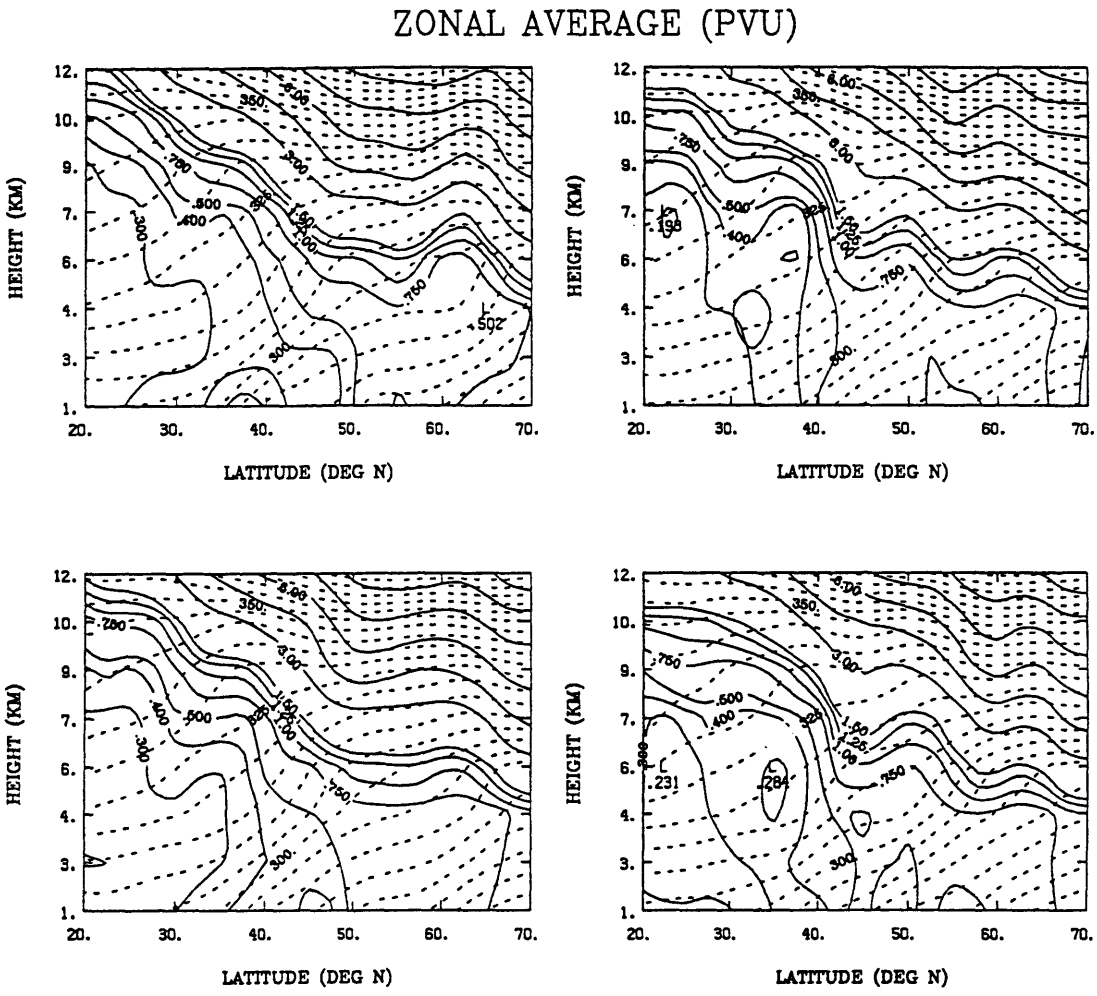


Figure 5.1 Cross sections of potential vorticity and potential temperature averaged over a wavelength of the case II cyclone. Contouring convention for PV is: 0.1PVU interval for q between 0 and 0.5 PVU, 0.25 PVU between 0.5 and 1.5 PVU, and 1.5 PVU for higher values. Potential temperature is contoured in 5K intervals. (a) (upper left) 12Z 09 November, 1988; 120W to 80W; (b) (lower left) 00Z 10; 110W to 70W; (c) (upper right) 12Z 10; 100W to 60W; (d) (lower right) 00Z 11; 90W to 50W.

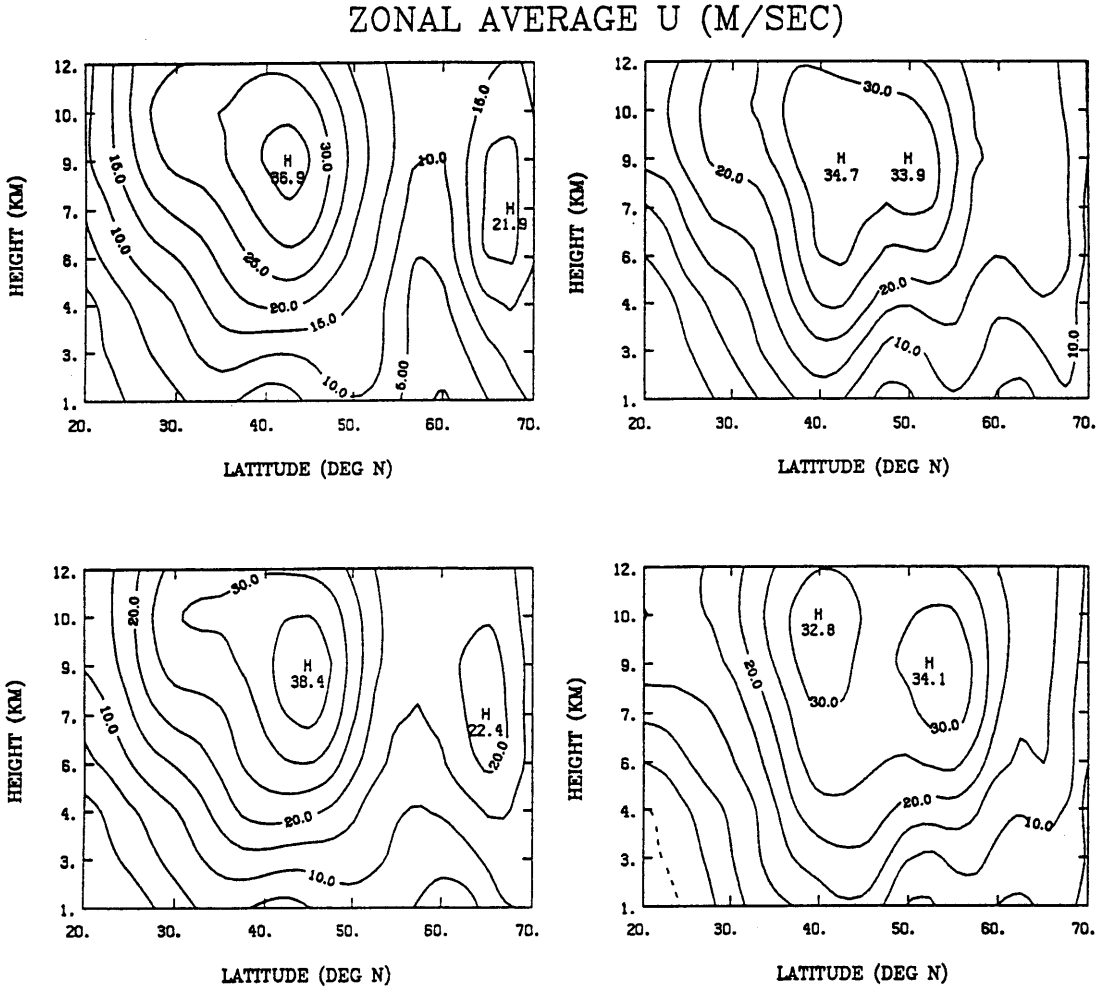


Figure 5.1 (continued) Zonal winds averaged over a wavelength. Contour interval is $5ms^{-1}$. Figures (e)-(h) correspond to (a)-(d) on previous page.

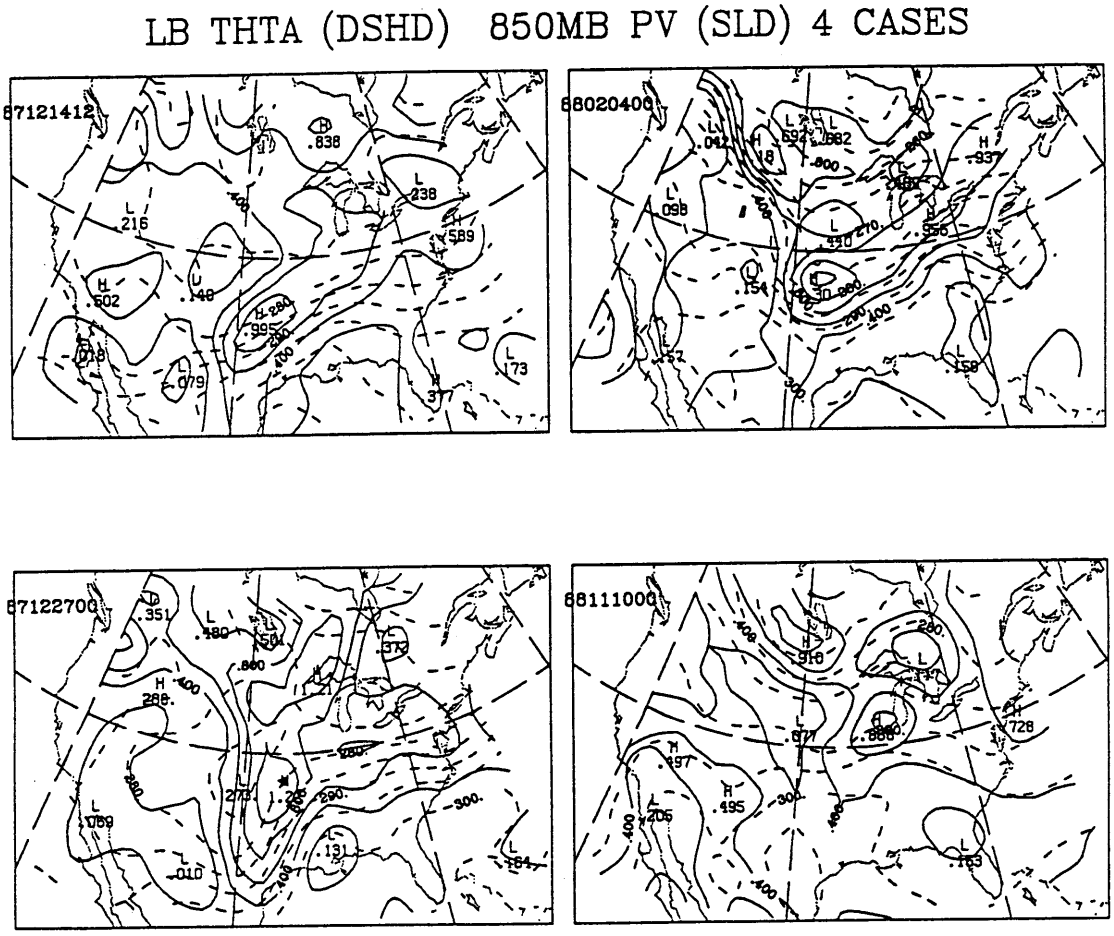


Figure 5.2 Lower boundary potential temperature and 850mb potential vorticity (PVU). Contour interval for PV is 0.2 PVU (solid), for θ it is 5K (dashed) (a) 12Z 14 December, 1987; (b) 00Z 27 December, 1987; (c) 00Z 04 February, 1988; (d) 00Z 10 November, 1988.

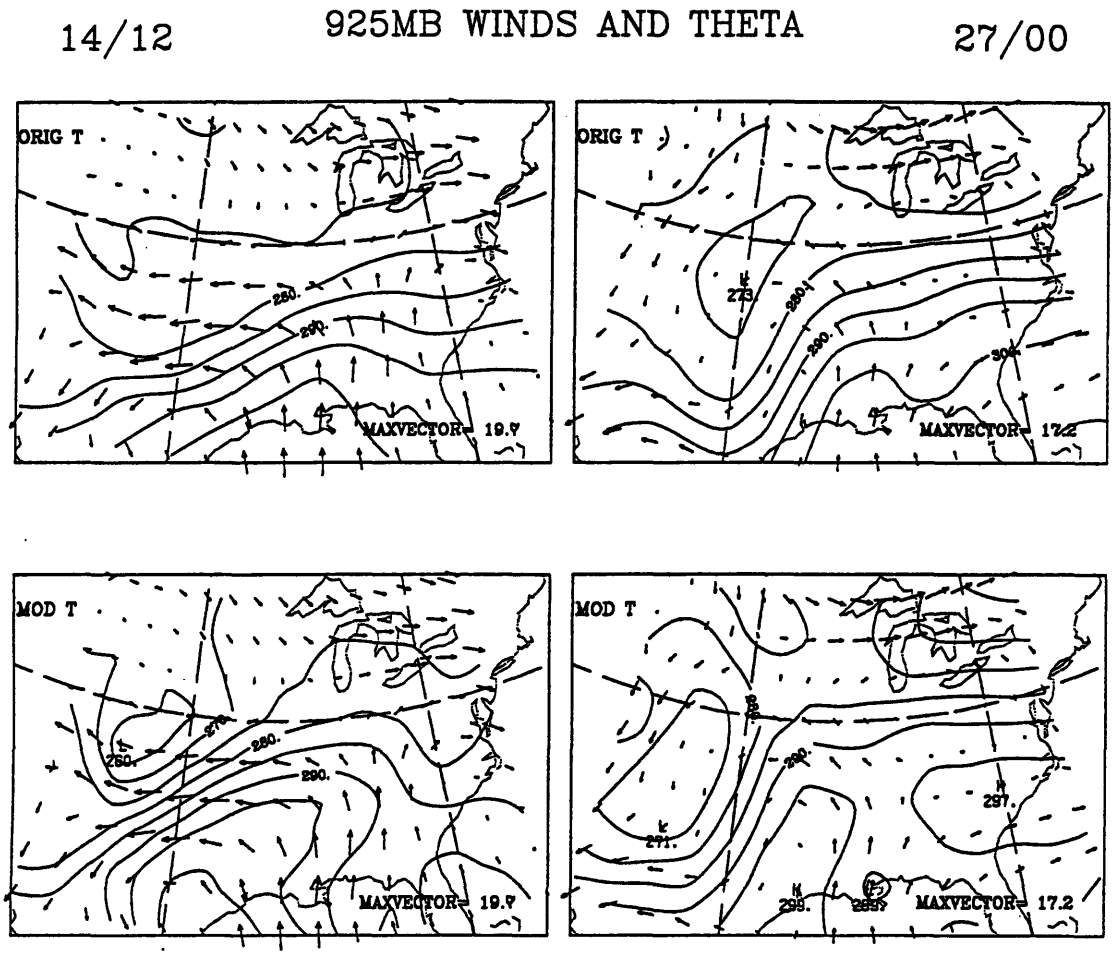


Figure 5.3 Balanced nondivergent winds at 925mb and two versions of lower boundary potential temperature (θ_B="orig" and θ_B*="mod"). Contour interval for potential temperature is 5K. Left column is for 12Z 14 December, 1987 (corresponds to 5.2(a)), (a) θ_B; (b) θ_B*. Right column is as left column except for 00Z 27 December, 1987 (figure 5.2b). Winds in (a) and (b) are the same as are those in (c) and (d).

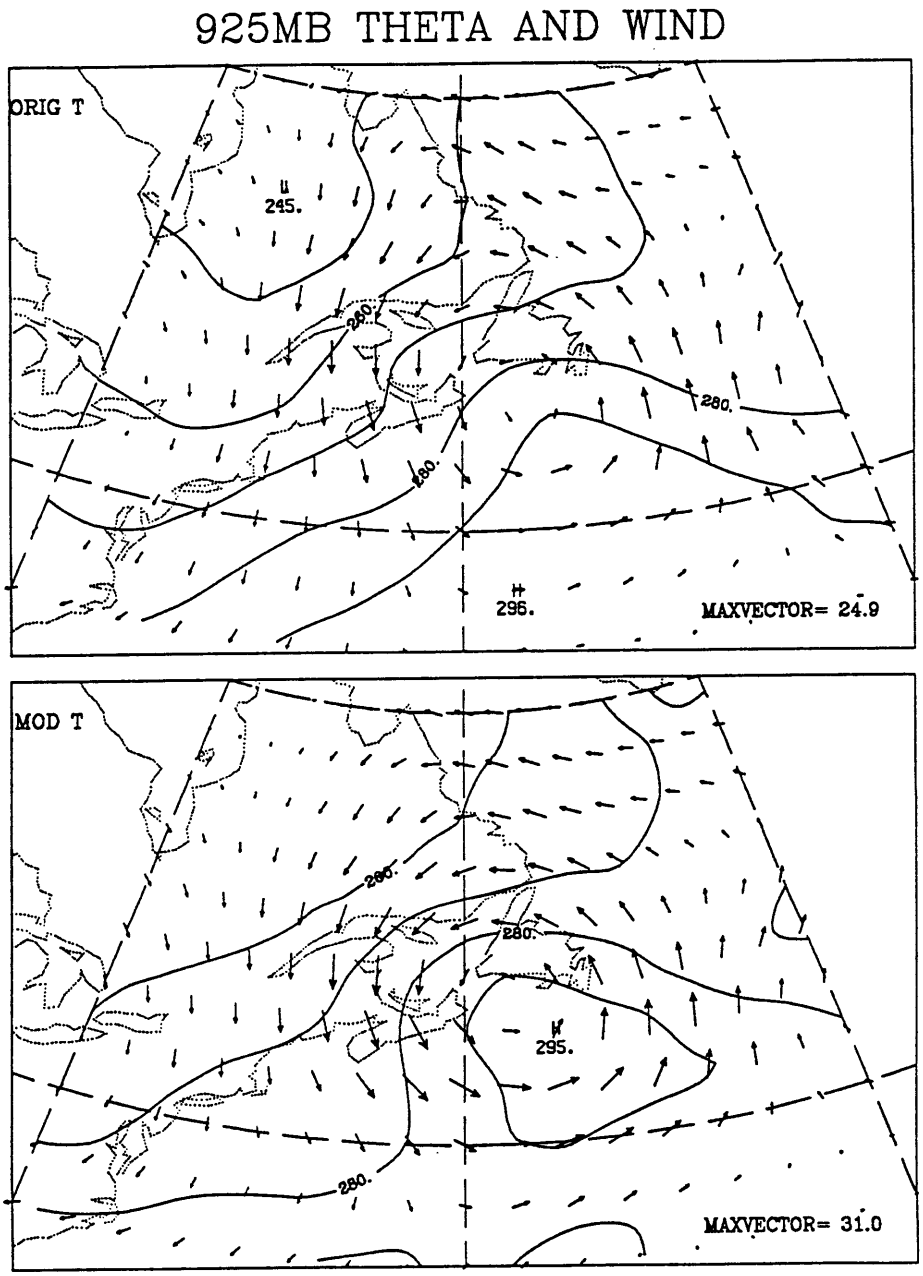


Figure 5.4 As in figure 5.3, but for 12Z 05 February, 1988; (a) θ_B (b) θ_B^*.

Appendix A

For simplicity, consider a two dimensional case of flow perpendicular to a line connecting two stations. Let 'v' denote the wind and 'x' denote the direction orthogonal to it. Then

$$q = -g\{ (f + v_x)\theta_p - v_p\theta_x \}. \quad (A.1)$$

The errors in wind and potential temperature generally increase with height. Estimates of rawinsonde errors in the lower troposphere are about 3 ms^{-1} for wind and 1K for θ (nearly all the error in potential temperature is due to temperature errors). In the lower stratosphere, tracking of rawinsondes becomes more difficult and wind errors may approach 5 ms^{-1} while errors in potential temperature may approach 2K. These estimates are taken from Bengtsson (1976). We let L and P represent the station spacing and the vertical resolution (mandatory levels) respectively. Then

$$q_{err} \approx -g\{ (\theta_p/L + \theta_x/P)\,\Delta v + (v_p/L + (f+v_x)/P)\,\Delta\theta \} \quad (A.2)$$

With typical atmospheric parameters in the lower troposphere, $\theta_p \approx 5\times10^{-4}$K PA^{-1}, $v_p \approx 5\times10^{-4}$K PA^{-1}, $\theta_x \approx 2\times10^{-5}$K m^{-1} (from thermal wind) and assume the relative vorticity is zero ($f=10^{-4}s^{-1}$). If we then assume L=300km as a typical station spacing and P=150mb as the resolution of the lower tropospheric mandatory levels, we have

$$q_{err} \approx 0.03\,\Delta v + 0.085\,\Delta\theta \quad \text{in PVU} \quad (A.3)$$

For $\Delta v = \pm3$ ms^{-1} and $\Delta\theta = \pm1$ K, $q_{err} \approx \pm0.18$ PVU.

At upper levels, we ignore the second term in A.1 compared to the first and estimate $\theta_p \approx 5\times10^{-3}$K PA^{-1}. Then with $\Delta v = \pm5$ ms^{-1}, $\Delta\theta = \pm2$ K and P=50mb, we obtain $q_{err} \approx \pm1.2$ PVU, which should serve as a typical lower stratospheric

error in potential vorticity averaged over the scales given by L and P. We note that to compare its effect on the balanced flow to that of errors in the lower troposphere, this should probably be normalized by the static stability of the basic state. This is because a given PV anomaly has a smaller influence when the surrounding stability (or potential vorticity) is larger.

Bell G. and L. F. Bosart, 1988: Appalachian cold air damming. *Mon. Weath. Rev.* 116, 137-161

Bengtsson, L. O., 1976: Initial data and some practical aspects of weather forecasting. NCAR colloquium, "Weather Forecasting and Weather Forecasts: Models, Systems, and Users" Volume 1. 254-419

Bjerknes, J. and Solberg, 1922: Life cycles of cyclones and the polar front theory of atmospheric circulation. *Geofysiske Publikasjoner.* 3, 3-18

Bjerknes, J. and J. Holmboe, 1944: On the theory of cyclones. *J. Meteor.* 1, 1-22

Bjerknes, J., 1954: The diffluent upper trough. *Meteor., Geophys., Bio.,* Ser A 7, 41-46

Bleck, R. and C. Mattocks, 1984: A preliminary analysis of the role of potential vorticity in Alpine lee cyclogenesis. *Beitr. Phys. Atmos.* 57, 357-368

Boyle, J. S. and L. F. Bosart, 1986: Cyclone-anticyclone couplets over North America. Part II: Analysis of a major cyclone event over the Eastern United States. *Mon. Weath. Rev.* 114, 2432-2465

Bosart, L. F., 1981: The Presidents' Day snowstorm of 18-19 February 1979: a subsynoptic scale event. *Mon. Weath. Rev.* 109, 1542-1566

Bosart, L. F. and C. Lin, 1984. Diagnostic analysis of the Presidents' Day storm of February 1979. *Mon. Weath. Rev.* 112, 2148-2177

Bretherton, F. P., 1966a: Critical layer instability in baroclinic flows. *Quart. J. Roy. Met. Soc.* 92, 325-334

" " , 1966b: Baroclinic instability and the shortwave cutoff in terms of potential vorticity. *Quart. J. Roy. Met. Soc.* 92, 335-345

Charney, J. G., 1947: The dynamics of longwaves in a baroclinic westerly current. *J. Meteor.* 4, 135-163

" " , 1955: The use of primitive equations of motion in numerical prediction. *Tellus* 7, 22-26

" " , 1962: Integration of the primitive and balance equations. *Proc. Symp. Numerical Weather Prediction, Tokyo.* 131-152

" " and M. E. Stern, 1962: On the stability of internal baroclinic jets in a rotating atmosphere. *J. Atmos. Sci.* 19, 159-172

Courant, R. and D. Hilbert, 1962: "Methods of Mathematical Physics". Vol 2. Interscience. pp 324-326

Danard, M. B., 1964: On the influence of released latent heat on cyclone development. *J. Appl. Meteor.* 3, 27-37

Danielsen, E. F., 1968: Stratospheric-tropospheric exchange based on radioactivity, ozone and potential vorticity. *J. Atmos. Sci.* 25, 502-518

Dimego, G. J. and L. F. Bosart, 1982: The transformation of Tropical Storm Agnes into an extratropical cyclone. Part 1: the observed fields and vertical motion computation. *Mon. Weath. Rev.* 110, 385-411

Eady, T. E., 1949: Long waves and cyclone waves. *Tellus* 1, 33-52

Eliassen, A. and E. Kleinschmidt, 1957: "Dynamic Meteorology" in Handbuch der Physik, Vol 48, 1-154, Springer Verlag, N.Y.

Emanuel, K. A., M. Fantini and A. J. Thorpe, 1987: Baroclinic instability in an environment of small stability to slantwise moist convection. Part I: Two dimensional models. *J. Atmos. Sci.* 44, 1559-1573

" " , 1988: Observational evidence of slantwise convective adjustment. *Mon. Weath. Rev.* 116, 1805-1815

Ertel H., 1942: Ein neuer hydrodynamischer wirbelsatz. *Met. Z.* 59, 271-281

Farrell, B. F., 1984: Modal and non-modal baroclinic waves. *J. Atmos. Sci.* 41, 668-673

" " , 1989: On the optimal excitation of baroclinic waves. *J. Atmos. Sci.* 46, 1193-1206

Gent, P. R. and J. G. McWilliams, 1983: Consistent balanced models in bounded and periodic domains. *Dyn. Atmos. Oceans* 7, 67-93

Gyakum, J. R., 1983: On the evolution of the QE II storm, II: Dynamic and thermodynamic structure. *Mon. Weath. Rev.* 111, 1156-1173

" " , and E. S. Barker, 1988: A case study of explosive subsynoptic-scale cyclogenesis. *Mon. Weath. Rev.* 116, 2225-2253

Green, J. S. A., 1960: A problem in baroclinic instability. *Quart. J. Roy. Met. Soc.* 86, 237-251

Haynes, P. H. and M. E. McIntyre, 1987: On the evolution of vorticity and potential vorticity in the presence of diabatic heating and frictional or other forces. *J. Atmos. Sci.* 44, 828-840

Haltiner, G. J. and R. T. Williams, 1980: "Numerical Prediction and Dynamic Meteorology", 2nd Ed. Wiley and Sons, N.Y.

Hoke, J. E., N. A. Phillips, G. J. Dimego, J. J. Tuccillo and J. G. Sela, 1989: The regional analysis and forecast system of the National Meteorological Center. *Weath. and Fore.* 4, 323-334

Holopainen, E. O. and L. Rontu, 1981: On shear lines in the upper troposphere over Europe. *Tellus* 33, 351-359

Hoskins, B. J. and F. P. Bretherton, 1972: Atmospheric frontogenesis models: mathematical formulation and solution. *J. Atmos. Sci.* 29, 11-37

" " , 1975: The geostrophic momentum approximation and the semigeostrophic equations. *J. Atmos. Sci.* , 2225-2253

" " , I. Draghici and H. C. Davies, 1978: A new look at the ω equation. *Quart. J. Roy. Met. Soc.* 104, 31-38

" " and M. Pedder, 1980: Diagnosis of middle latitude development. *Quart. J. Roy. Met. Soc.* 106, 707-719

" " and P. Berrisford, 1988: A potential vorticity perspective of the storm of 15-16 October 1987. *Weather* 43, 122-129

Iversen, T. and T. E. Nordeng, 1982: A convergent method for solving the balance equation. *Mon. Weath. Rev.* 110, 1347-1353

" " and " ", 1984: A hierarchy of nonlinear filtered models-numerical solutions. *Mon. Weath. Rev.* 112, 2048-2059

Juckes, M. N. and M. E. McIntyre, 1987: A high resolution one layer model of breaking planetary waves in the stratosphere. *Nature* 328, 590-596

Keyser, D. and R. Rotunno, 1990: On the fromation of potential vorticity anomalies in upper-level jet-front systems. submitted to *Mon. Weath. Rev.*

Krishnamurti, T. N., 1968: A diagnostic balanced model for studies of weather systems of low and high latitudes, Rossby number less than 1. *Mon. Weath. Rev.* 96, 197-207

Lindzen, R. S., 1988: Instability of plane parallel shear flow (toward a mechanistic picture of how it works). *Pure Appl. Geophys.* 126, 103-121

Lorenc, A. C., 1981: Global three-dimensional multivariate statistical interpolation scheme. *Mon. Weath. Rev.* 109, 701-721

Lynch, P., 1989: Partitioning the wind in a limited domain. *Mon. Weath. Rev.* 117, 1492-1500

Manabe, S., 1956: On the contribution of heat released by condensation to the change in pressure pattern. *J. Met. Soc. Japan* 34, 12-24

Montgomery, M. and B. F. Farrell, 1990: Moist surface frontogenesis associated with interior potential vorticity anomalies in a semi-geostrophic model. Submitted for publication

Nielsen, J. W., 1988: Direct analysis of Ertel's potential vorticity. *NCAR Colloquium on Synoptic Meteorology.* 38-47

Palmen, E. and C. W. Newton, 1969: "Atmospheric Circulation Systems". Acacemic Press, N.Y.

Pagnotti, V. and L. F. Bosart, 1984: Comparative diagnostic case study of East Coast secondary cyclogenesis under weak vs. strong synoptic-scale forcing. *Mon. Weath. Rev.* 112, 5-30

Pedlosky, J., 1979:"Geophysical Fluid Dynamics". Springer Verlag, NY

Petterssen, S., G. E. Dunn and L. L. Means, 1955: Report on an experiment in forecasting of cyclone development. *J. Appl. Meteor.* 12, 58-67

" " , 1956: "Weather Analysis and Forecasting. Vol. 1, Motion and Motion Systems". McGraw Hill, N.Y. 428p.

" " , D. L. Bradbury and K. Pedersen, 1962: The Norwegian Cyclone Models in relation to heat and cold sources. *Geofysiske Publikasjoner* 24, 243-280

" " and S. J. Smebye, 1971: On the development of extratropical cyclones. *Quart. J. Roy. Met. Soc.* 97, 457-482

Robinson, W. A., 1989: On the structure of potential vorticity in baroclinic instability. *Tellus* 41A, 275-284

Rossby, C. G., 1940: Planetary flow patterns in the atmosphere. *Quart. J. Roy. Met. Soc.* 66 Suppl., 68-87

Rotunno, R. and M. Fantini, 1989: Petterssen's Type B cyclogenesis in terms of discrete, neutral Eady modes. *J. Atmos. Sci.* 46, 3599-3604

Sanders, F., 1971: Analytic solutions to the nonlinear omega and vorticity equations for a structurally simple model of disturbances in the baroclinic westerlies. *Mon. Weath. Rev.* 99, 393-407

" " , and J. R. Gyakum, 1980: The synoptic-dynamic climatology of the "bomb". *Mon. Weath. Rev.* 108, 1589-1606

" " , 1986: Explosive cyclogenesis over the West Central North Atlantic Ocean 1981-1984, Part I: Composite structure and mean behavior. *Mon. Weath. Rev.* 114, 1781-1794

" " , 1987: A study of 500mb vorticity maxima crossing the East Coast of North America and associated surface cyclogenesis. *Weath. and Fore.* 2, 70-83

" " , 1988: Life history of mobile troughs in the upper westerlies. *Mon. Weath. Rev.* 118, 2629-2648

Shapiro, M. A., 1976: The role of turbulent heat flux in the generation of potential vorticity in the vicinity of upper level jet front systems. *Mon. Weath. Rev.* 104, 892-906

Simmons, A. J. and B. J. Hoskins, 1978: The life cycles of some nonlinear baroclinic waves. *J. Atmos. Sci.* 35, 414-432

" " and " " , 1979: The downstream and upstream development of baroclinic waves. *J. Atmos. Sci.* 36, 1239-1254

Snyder C., and R. S. Lindzen, 1988: Upper level baroclinic instability. *J. Atmos. Sci.* 45, 2445-2459

Snyder, C. 1989: "On the effects of partial equilibration and cumulus heating on baroclinic instability". Ph. D. Thesis, MIT. 160p.

Sutcliffe, R. C., 1947: A contribution to the problem of development. *Quart. J. Roy. Met. Soc.* 73, 370-383

Thorpe, A. J., 1985: Diagnosis of a balanced vortex structure using potential vorticity. *J. Atmos. Sci.* 42, 397-406

" " and K. A. Emanuel, 1985: Frontogenesis in the presense of small stability to slantwise moist convection. *J. Atmos. Sci.* 42, 1809-1824

" " , 1986: Synoptic scale disturbances with circular symmetry. *Mon. Weath. Rev.* 114, 1384-1389

Tracton, M. S., 1973: The role of cumulus convection in the development of extratropical cyclones. *Mon. Weath. Rev.* 101, 573-592

Trenberth, K. E., 1978: On the interpretation of the diagnostic quasigeostrophic omega equation. *Mon. Weath. Rev.* 106, 131-137

" " and J. G. Olson, 1988: Evaluation of NMC global analysis: 1979-1987. NCAR Technical Note TN-299+STR.

Tsou, C. H., P. J. Smith and P. M. Pauley, 1987: A comparison of adiabatic and diabatic forcing in an intense extratropical cyclone system. *Mon. Weath. Rev.* 115, 763-786

Uccellini, L. W., D. Keyser, K. F. Brill and C. H. Wash, 1985: The Presidents' Day cyclone of 18-19 February 1979: influence of upstream tropopause folding on rapid cyclogenesis. *Mon. Weath. Rev.* 113, 962-980